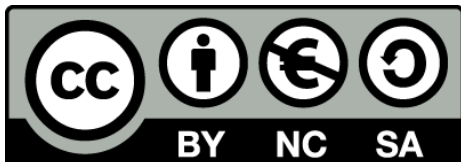




# Seismic structure of the crust beneath the Rif Cordillera

Alba Gil de la Iglesia



Aquesta tesi doctoral està subjecta a la llicència [Reconeixement- NoComercial – Compartirlgual 3.0. Espanya de Creative Commons](#).

Esta tesis doctoral está sujeta a la licencia [Reconocimiento - NoComercial – Compartirlgual 3.0. España de Creative Commons](#).

This doctoral thesis is licensed under the [Creative Commons Attribution- NonCommercial-ShareAlike 3.0. Spain License](#).

# **Seismic structure of the crust beneath the Rif Cordillera**

Dissertation submitted to Doctorate Program in Earth Sciences,  
University of Barcelona, to award the Degree “Doctor in Earth  
Sciences”

by **Alba Gil de la Iglesia**

Supervisors

Prof. Dr. Josep Gallar Musset

Dr. Jordi Díaz Cusí

Tutor

Prf. Dr. Giorgi Khazaradze



This thesis has been prepared at the  
Institut de Ciències de la Terra Jaume Almera  
Consejo Superior de Investigaciones Científicas (CSIC)



*A la meva família*



## Agraïments

Tota feina ben feta no es fa en un sol dia i no és fruit d'una sola persona, i aquesta tesis no l'excepció. Molta gent ha participat directament o indirectament en l'evolució d'aquesta tesis. A tots ells els hi vull agrair la seva ajuda.

Per començar, voldria agrair al meus dos directors de Tesis, Josep Gallart Muset i Jordi Díaz Cusí, l'esforç i paciència dedicat en mi durant aquest 4 anys i escaig de Doctorat. Al dos els vull donar les gràcies per haver-me donat l'oportunitat de col·laborar en el projecte RIFESIS, i per haver compartit amb mi els vostres coneixements en sísmica i sismologia. Gràcies pels vostres consells, ajuda i ànims per tirar endavant aquesta tesis, i fer-me el interessant i “divertida” que pot arribar a ser el camp de la geofísica. Moltes gràcies, de debò.

També voldria agrair als diversos investigadors del centre Jaume Almera, per haver compartit els seus coneixements amb mi durant la meva etapa en el centre. En especial a en Mario, per haver-me guiat en LUNIX, GMT, Seismic Unix, etc. A en Ramon, per haver-me ajudat en molts cassos. Sempre que necessitis una assistent de micròfons, o algú al camp, sempre estaré disposada a donar un cop de mà. A la Montse i la Conxi, per haver compartit els seus coneixements en gravimetria, sense vosaltres encara m'estaria barallant amb GM-SYS. A en Jaume, Emilio i Eduard, pels vostres consells en geologia estructural i ajudar-me amb la geologia del Marroc. Moltes gràcies a tots vosaltres per haver-me compartir els vostres coneixements amb mi, i fer els moments més complicats més fàcils.

I want to thank to Alan, for his advices during my stay in Rice University. To Imma, Rachel, Sally, Chen, Hehe, Emily, Helene, Min, Lester, to making my stay at Rice more comfortable and feel one of them.

Com que tot té un principi, voldria agrair a la Pilar, en Juanjo i en Gia, que van ser els que hem van iniciar en el mon de la Geofísica. Els hi agraeixo les ensenyances en el tema de la sismologia, en especial a en Gia que va ser qui em va guiar amb el treball de final de carrera.

També voldria agrair la convivència que hem compartit durant tots aquest anys a la gent del despatx. A tots, els que han estat i ja han marxa't, els que encara hi estan, i els que acaben d'arribar. Gràcies per suportar els meus canvis d'humor, les meves queixes respecte la temperatura de la sala, etc. En especial a la Mar, Juan, Giovanni, Jan i Siddique, Thanks for the good times, jokes and scientist comments. Thanks for makig the offise my second home. I would like to thank to Grant and Stephanie, who help me with my English and share these coffee moments. No voldria oblidar-me dels amics de l'hora d'esmorzar. Moltes gràcies per avisar-me cada dia per anar a fer un cafè, encara que moltes vegades estiguí desapareguda. Tampoco quisiera olvidarme de Alberto, Chusa, Mireia, Marcel, Giomar, Raquel y Delphine.

I really want to thank to Pat and Patty, for receiving me in their house during Halloween. I really enjoyed that time with both of you, it was short but intense. As well I want to thank to Ed and Pam, for showing me the city and surroundings of Houston. A Adriana por haber venido a visitarme a Houston cuando más necesitaba una muy buena amiga.

También agradecer a Lavinia, a quien quiero como a una hermana. Gracias por los ánimos que me has dado, y sobre todo por esos momentos de desconexión junto con Chiara, Charlotte, JaunDi, Vinyet, Ily, Mauri y Ana. Gracias por atraerme al mundo real en esos momentos que creía que no existía mañana. Muchas gracias por hacer estado allí siempre que os he necesitado. També a Berta i María, que encara que ens hem deixat de veure'ns tan freqüentment encara us en recordeu de mi. Moltes gràcies per seguir contant en mi en les vostres quedades. Us estimo molt a les dues.

Finalment, però per això no menys important. Voldria donar les gràcies als meus pares, que sempre ens han ensenyat al meu germà i a mi fer allò que més ens agradava. Us vull agrair, no només el fet de haver-me donat la vida, si no per donar-me tots els coneixements que meu donat, ja siguin de cultura com de la vida. Per haver-me donat l'oportunitat de fer allò que sempre he volgut fer, i ajudar-me ser qui soc ara, i veure'm com si fos Indiana Jones o un Goonie. Gràcies per permetre'm somiar i que aquests es facin realitat, encara que sigui en els vostres ulls. A en Didac, que tot i que estàs molt lluny de casa sempre t'he sentit al meu costat. Que sempre has sigut el meu model a seguir, i sempre que estic perduda fas el possible per guiar-me, encara que això impliqui moure cel i terra. Moltes gràcies als tres, us estimo molt.

Alba, Desembre 2014

**Funding:**

The author of this thesis benefits from a four-year FPI (training personal researcher) from Ministry of Economy and Competitiveness between 2010 and 2014. The author was also granted within the framework of the EEBB (short-term stays) with the following stay: 4 month at the Department of Earth Sciences at Rice University, in Houston (Texas, USA). The FPI was supported by the RIFESIS project, which was funded by the Spanish Ministry of Economy and Competitiveness, with reference PNIDI-CGL CGL2009-09727. The data used in this work was acquired within the RIFESIS, PICASSO and Topo-Iberia projects. These last projects were funded by the National Science Foundation EAR-0808939; and the Spanish Ministry of Economy and Competitiveness PNIDI-CONSOLIDER CSD2006-00041, respectively



# CONTENTS

SUMMARY	i
---------	---

<b>Part I: Outlook. Objectives and methods</b>	<b>1</b>
<b>Chapter 1: General Introduction</b>	<b>3</b>
<b>Chapter 2: Geological and Geodynamical framework</b>	<b>9</b>
2.1    Introduction	9
2.2    Geology of North Morocco	12
2.2.1    Rif Cordillera	12
2.2.2    Alboran Basin	14
2.2.3    Foreland Basin	15
2.3    Previous Geophysical Studies	15
2.4    Geodynamic models	21
<b>Chapter 3: Methodological approaches</b>	<b>23</b>
3.1    Pn/Sn Travel-time tomography	24
3.1.1    Data selection	26
3.1.2    Method	28
3.2    Active source profiling	32
3.2.1    Wide-Angle reflection/refraction seismic data processing	34
3.2.2    Wide-Angle reflection/refraction seismic data interpretation	37
a)    Travel time Inversion Method (RAYINVR code)	37
b)    First Arrival Seismic Tomography (FAST code)	38
c)    3D low fold wide-angle seismic stack	40
3.2.3    Gravity validation	44
3.3    Receiver Functions	46

<b>Part II: Results</b>	<b>51</b>
<b>Chapter 4: Uppermost mantle velocity and anisotropy in the Euro-Mediterranean region from Pn and Sn tomography</b>	<b>53</b>
4.1    Introduction	53
4.2    Data analysis	53
4.3    Results	59
4.4    Discussion	68
<b>Chapter 5: 2-D velocity-depth transects from wide-angle reflection/refraction seismic profiling</b>	<b>75</b>
5.1    Introduction	75
5.2    Lateral variations of the structure beneath the External Rif domain: East-West profile from Gharb Basin to the Algerian border	79
5.3    North-South Rif transect, from Middle Atlas domains to the Betic range	88
5.4    Gravity control from wide-angle data	95
5.5    Discussion	99
<b>Chapter 6: Mapping the Moho beneath the Rif Cordillera with wide-angle reflections</b>	<b>103</b>
6.1    Introduction	103
6.2    Low-fold wide-angle stacks and offline $PmP$ measurements	105
6.2.1        Data processing	107
6.2.2        Data interpretation	113
6.3    Discussions	118
<b>Chapter 7: Moho-depth constraints from receiver functions (Topo-Iberia and PICASSO networks)</b>	<b>123</b>
7.1    Introduction	123
7.2    Data selection and processing	124
7.3    Crustal thickness map	132
<b>Part III: Conclusions</b>	<b>139</b>
<b>Chapter 8: Conclusions</b>	<b>141</b>
<b>References</b>	<b>147</b>

## SUMMARY

The Rif Cordillera, situated in northern Morocco, together with the Betic Range forms one of the tightest orogenic arcs on Earth, the Gibraltar Arc System. This arched orogenic belt was created by the convergence between the Euarsia and Africa plates. The complexity of this area led to several tectonics models (e.g. Platt and Vissers, 1989; Seber et al., 1996; Lonergan and White, 1997; Zeck, 1997). In this thesis I present a geophysical study that aims to characterize the crustal structure in the northern part of Morocco, especially beneath the Rif Cordillera.

The geophysical data used in this thesis was acquired during RIFSI (2011) survey within the framework of the RIFSI project, which was designated to overcome the lack of results on crustal structure in the northern part of Morocco. The RIFSI project is mainly based on the acquisition of new wide-angle seismic profiles and on the integration of these data with the various seismic data sets currently available, such as the PICASSO (Platt et al., 2008) and Topo-Iberia (Díaz et al., 2009) projects.

The present work is based on the processing, modeling and interpretation of Wide-Angle seismic (WA) and Receiver Functions (RFs) data projects, and has been focused on the crust below Morocco. The WA data was acquired during the RIFSI survey in the Rif Cordillera from two longest profiles; the north-south profile (~430 km) and the east-west profile (~330 km). Both profiles extend across the Rif orogen, from the Middle Atlas to the Betic Range, and from the Gharb basin to the Algerian border, respectively. The RFs data was acquired from the temporary deployment of seismological broadband stations from PICASSO and Topo-Iberia projects. These stations were deployed along all the north Morocco territory. I also have worked with  $Pn$  tomography of the uppermost mantle seismic velocity and anisotropy in the Euro-Mediterranean region.

The study of seismic velocity and anisotropy variations in the uppermost mantle beneath the Euro-Mediterranean region was compiled from inversion of  $Pn$  and  $Sn$  phases. The Method of Hearn has been applied to the travel-time arrivals of the International Seismological Center catalogue. A total of 579753  $Pn$  arrivals coming from 12377 events recorded at 1408 stations with epicentral distances between 200 km and 1400 km have been retained after applying standard quality criteria. The results show significant features well correlated with surface geology and evidence the heterogeneous character of the Euro-Mediterranean lithosphere. The station terms reflect the existence of marked variations in crustal thickness, consistent with available Moho depths inferred from active seismic experiments. The introduction of an anisotropic term enhances significantly the lateral discontinuity of the anomalies, in particular in the most active tectonic areas.  $Pn$  anisotropy shows consistent orientations subparallel to major orogenic structures, such as the Betic Range.

The processing of RIFSIS seismic data provides the tectonic crustal structure model of the Rif Cordillera, whereas the modeling of WA data from travel-time forward modelling provides 2-D seismic velocity distribution of the crust and uppermost mantle. Furthermore, from the results that these projects provide, it becomes possible to infer the geometry of the crust-mantle boundary, also presented in this thesis. These velocity-depth models hold major variations in the crustal thickness, especially the EW profile that shows a rapid change of 15-20 km in Moho depths within 30 km horizontal distances. Maximum depths around 50 km are found below the external Rif domain, while thinnest values of about 29 km are located eastwards, in the foreland and Atlasic terraces up to the Algerian border. The model along NS profile displays also marked differences in crustal thickness, ranging from 40 km beneath the Betics and internal Rif sampled domains, to 47-48 km beneath external Rif, and a progressive thinning southwards till Middle Atlas domain where the Moho is found at 32 km depth. The WA models are then converted to density models using the classical relation  $V_p-\rho$ , in order to verify them with the Bouguer gravity anomaly data.

We processed the WA data as low-fold WA seismic images. The deployment logistics during the RIFSIS project enabled all the stations to record all shots, not limited to the shots aligned with the two profiles. From these profiles we can obtain a deep crustal image in-between the profiles and the shots. We have also estimated the Moho geometry from the  $PmP$  phases identified in the onshore-offshore record sections of the offshore GASSIS-WestMed experiment. The GASSIS-WestMed experiment and the RIFSIS project were conducted in parallel. Those times can be tentatively related to crustal thickness assuming a homogeneous crustal velocity. Although some uncertainties may be inherent to those approaches, a large crustal root, reaching more than 50 km, is well-documented in the central part of the Rif Cordillera. At the same time, I performed a RFs study in the Rif domain area, in order to determine the crustal thickness beneath the northern Morocco. This has resulted in an independent estimation of the crustal depth which can be compared to the models derived from WA data.

In summary, the results obtained from the different methodologies used in this thesis reveal us a crustal root well-documented in the central part of the Rif Cordillera, which is supported by the area large negative Bouguer anomaly values. I interpreted the Rif Cordillera crustal structure as resulting from a complex interaction of the Miocene to present continent-continent collision between Iberian and Africa plates, coupled with rollback of the Neo-Thethys Alboran slab. This hypothesis is highly aligned with the final 3-D numerical modelling of the western Mediterranean region presented by Chertova et al. (2014).

**Part I:**

**OUTLOOK.**

**OBJECTIVE AND METHODS**



# Chapter 1: General Introduction

The Earth has a cool and therefore mechanically strong outermost shell called the lithosphere (from the Greek lithos for “rock” and spharia for “sphere”). It comprises the crust, which includes the rocks exposed at the surface of the Earth, and the uppermost mantle. The limit between crust and mantle, the Mohorovicic discontinuity, is related to strong changes in chemical composition and seismic properties; the crust is mainly formed by maphic rocks and has typical mean P-wave velocity around 6.2 km/s, while the uppermost mantle is dominated by peridotites and the P-wave velocity is close to 8.0 km/s. Continental lithosphere thickness ranges between 40 to 280 km, even if typical values are around 100-150 km, while beneath the oceans the lithosphere is thinner, reaching maximum depths of 140 km. Knowledge of the structure, composition, and secular evolution of the lithosphere is primordial for understanding the geological evolution of the Earth since its formation.

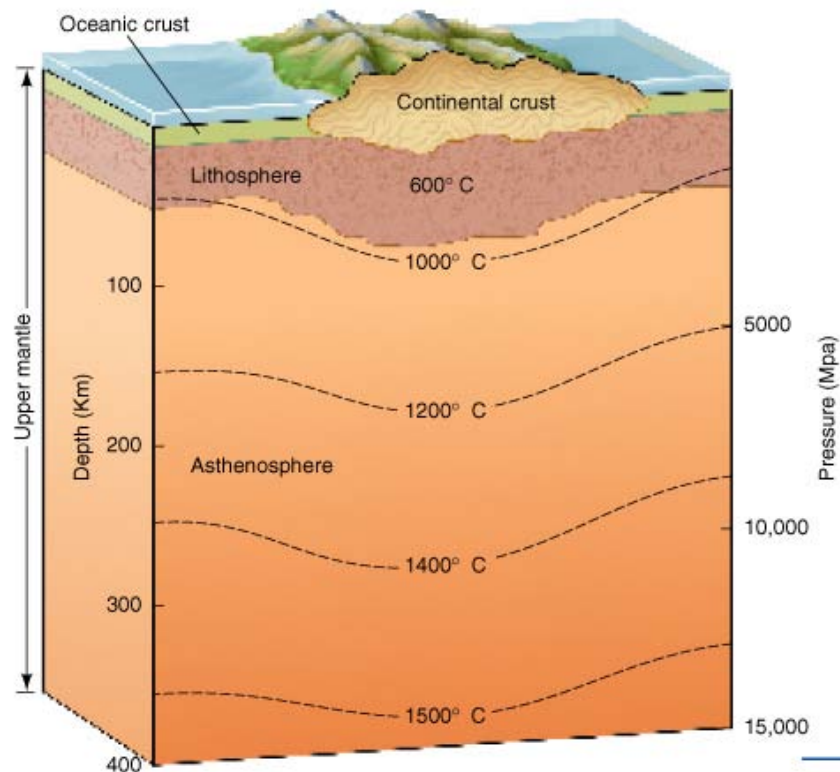


**Figure 1.1:** Sketch depicting the structure of the uppermost layers of the Earth (Tarbuck et al., 2013)

The lithosphere must be studied by indirect methods based on geophysical properties which allow the study of physical properties across large sections of in situ lithosphere. The physical properties determined by geophysical field experiments can be then compared to laboratory measurements to place constraints on the composition of the lithosphere. Among such geophysical methods, seismic exploration is widely recognized as one of the most powerful tools to explore the interior of the Earth.

At the westernmost Mediterranean region the complex interactions between two continental masses, the Eurasian and African plates, has produced a broad arcuate collision zone, the Gibraltar Arc System, which comprises the Betic and Rif mountain ranges separated by the Alboran Sea basin.



**Figure 1.2:** Geographic location map of the study area (image from [visibleearth.nasa.gov/](http://visibleearth.nasa.gov/))

A wide variety of tectonic models have been proposed, based mostly on the surface geology (see Platt et al., 2013 for a review), whereas only recently has detailed

information been available of the deep structure of much of this region, particularly on the Rif Cordillera in North Morocco. In the last decade a major effort has been done to get new data on this area (Figure 1.3), with large scale initiatives as Topo-Iberia (Díaz et al., 2009) and PICASSO (Program to Investigate Convective Alboran Sea System Overturn; Platt et al., 2008). However, one of the missing knowledge which needs to be fulfilled is the seismic crustal structure of Morocco, including the topography of the crust-mantle boundary as very few data are available so far. This is the main objective of projects based in seismic exploration carried out during the last 5 years, as RIFIS (Seismic Investigations across the Rif; Gallart et al, 2012), SIMA (Seismic Imaging of the Moroccan Atlas; Ayarza et al., 2014), or GASSIS-WestMed (Gràcia et al., 2012).

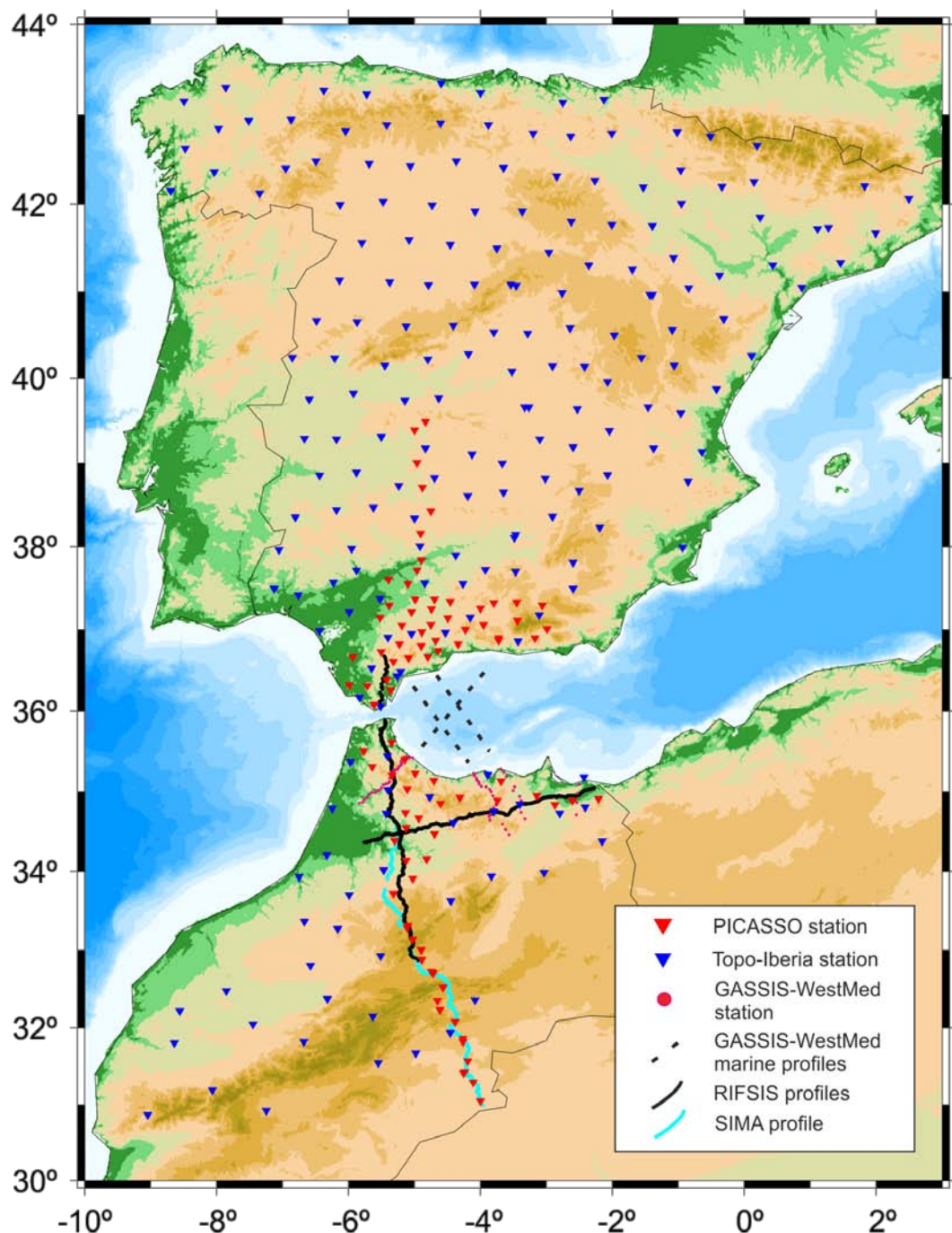


**Figure 1.3:** Map of Iberian Peninsula and North Africa, where are represented the coverage of the PICASSO (in red), Topo-Iberia (in blue), RIFSIS (in black), SIMA (in cyan) and the GASSIS-WestMed (in dashed lines and magenta dots) projects.

The main goal of this thesis is to investigate the lithosphere beneath this region using different seismic techniques based on the analysis of natural seismicity and controlled-source profiles.

The first method used in this work to investigate the uppermost mantle properties is based on the analysis of the time propagation anomalies of Pn and Sn phases at regional scale. These seismic waves travel closely beneath the Moho and thus provide a detailed image of the seismic properties of this depth zone. This tomographic approach, based on time arrivals catalogues, is not restricted to the Gibraltar Arc but comprises the whole Euro-Mediterranean region to provide a large scale view of the region.

This thesis is largely based on the interpretation of the data resulting from the RIFSIS project, which intends to overcome the lack of results on the crustal structure beneath Northern Morocco and in particular beneath the Rif Cordillera from the interpretation of two wide-angle seismic reflection profiles, 330 km-long and 430 km-long, EW and NS oriented, respectively. The modelling of the wide-angle seismic profiles is expected to provide a model of the velocity-depth structure of the crust, including the topography of the main discontinuities, as the basement or the Moho. To obtain those P-wave velocity-depth models we will use the classical forward modeling of Zelt and Smith (1992) based on ray path theory. In this approach, a synthetic model is generated using the available previous information and the corresponding travel-times and amplitudes are compared to the observations. The analysis of the misfits leads to the modification of the theoretical model and to a new iteration in the process, till reaching a satisfactory adjustment of all the data set. I have also tried to use an inversion approach (in which the observations are inverted to obtain a theoretical model), but this has been unsuccessful, probably due to the moderate density of our data coverage and the complexity of the velocity-depth structure.

In order to assess the consistency of the resulting models, they have been converted to gravity using classical relationships (Christensen and Mooney, 1995; Brocher, 2005) between seismic velocity and density and then compared successfully to the available gravity observations.

The deployment logistics during the RIFSIS project allowed that all the stations recorded not only the shots aligned with each profile, but also the rest of them. This allows also a data processing to obtain a wide-angle, low-fold seismic stack following the method described in Carbonell et al. (2002). A hyperbolic time reduction is applied

to the data, resulting in stacks in which the reflections from the Moho are expected to appear as subhorizontal energy. This provides insight on the Moho depth variations offline of the main seismic profiles. A second, complementary approach arises from the identification and reading of the arrival times corresponding to PmP phases in the offline record section of the RIFSIS shots. Those times can be tentatively related to crustal thickness assuming an homogeneous crustal velocity. Even if those assumptions imply that large errors can arise in case of heterogeneities, we will show that the method can provide significant results in this region.

The crustal thickness beneath northern Morocco has also been investigated from teleseismic data using the Receiver Function technique. We have reprocessed data from both the Topo-Iberia and PICASSO experiments and we have also installed some complementary stations to densify the data in the investigated zone. This has resulted in an independent estimation of the crustal depth which can be compared to the models derived from active seismics.

In summary, the objectives of this thesis are:

1. To derive the seismic properties of the uppermost mantle beneath the Euro-Mediterranean region using  $Pn$  and  $Sn$  tomography.
2. To derive the velocity-depth crustal structure beneath the Rif Cordillera based on the modeling of the RIFSIS wide-angle seismic profiles
3. To investigate the crustal thickness offline the RIFSIS profiles from the unconventional process of new and existing data.
4. To constrain the Moho topography beneath the region from the analysis of 2-D passive seismic data along the Rif Cordillera

The basic aim of this study is thus to provide new insight on the crustal structure beneath the Rif, and subsequently to provide stronger constraints on the geodynamical models proposed for the área .

## Chapter 2: Geological and Geodynamical framework

### 2.1 Domains and evolution in the study area and surroundings

The Western Mediterranean Region has a complex geodynamical history. After the Variscan orogeny, a large rifting episode affected the Mediterranean region in Mesozoic times. Later on, during the late Mesozoic, the area was dominated by subduction zones of relatively short wavelength which consumed the previous Tethyan oceanic crust and its continental margins. Since Cenozoic times, the tectonics is dominated by the opening of small-size oceanic domains in backarc situation in the framework of an Africa-Eurasia convergence. The main subduction zones surrounding the Mediterranean Basin are the Alps-Betics, the Apennines-Maghrebides and the Dinarides-Hellenides-Taurides, which have been imaged as high velocity slabs within the upper mantle in global and regional body-wave tomographies (Bijwaard and Spakman, 2000; Piromallo and Morelli, 2003; Koulakov et al., 2009; Zhu et al., 2012; Giacomuzzi et al., 2012). Extensional processes affected the whole region in Neogene times, as evidenced by the observation of a shallow asthenospheric layer in S-velocity tomographies (Marone et al., 2004; Schmid et al., 2008; Boschi et al., 2009; Legendre et al., 2012). Those extensional processes resulted in the opening of the Alboran, Algerian, Valencia and Provençal basins in the west, the Tyrrhenian and Ionian basins in the central Mediterranean, the Aegean basin in the east and the Pannonian basin at the northern limit of the investigated area. The origin of the Tyrrhenian and Alboran Seas seems related to the fast rollback migration of the former west Mediterranean subduction zone that resulted in the Calabrian and Gibraltar arcs migrating east and westwards, respectively. Since Neogene times, Africa is converging relative to Europe at a rate of about 5 mm/year, as evidenced by space geodesy data. The direction of the relative motion between both plates is not completely understood, with a dominant NW-SE direction in the western Mediterranean and a NNE-SSW direction to the east. This framework resulted in a complicated tectonic pattern dominated nowadays by large regions of extension surrounded by arcuate belts of compression (Carminati and Doglioni, 2004).

The limit between Iberian and African plates is not well constrained from the Gulf of Cadiz to the Algerian coast (Vernant et al., 2010). The contact appears as a diffuse transpressive band of active deformation with significant seismicity at intermediate and deep levels. Geological, geophysical and geochemical data have provided evidences of coeval extensional tectonics in the Alboran region during convergence between Africa and Eurasia (Dewey, 1988, Comas et al., 1999). The area was affected by N-S convergence since 35 Ma (Platt and Vissers, 1989), followed by a roughly EW oriented extensional episode from 27 to 7 Ma (Watts et al., 1993) and slow oblique convergence (5-6 mm/y), oriented approximately NNW-SSE, from 7 Ma to present. This continental boundary zone is dominated now by the slow convergence between Nubia and Eurasia, but clear evidences of extensional tectonics can be observed which require a complex geodynamic scenario to be explained.

The Gibraltar Arc system, one of the tightest orogenic arcs on Earth, forms the Westernmost Mediterranean Alpine belt and comprises the Betic and Rif Cordilleras and a deep sedimentary basin over the extended continental crust of the Alboran Sea, which developed roughly synchronously with the orogenic belt during the Miocene (Vergés and Fernández, 2012; Platt et al., 2013). The Rif Cordillera corresponds to the southern branch of the Gibraltar Arc and is located at the westernmost part of the Maghrebide belt (Rif, Tell, Kabylies), which extends along the north Africa coast, and continues eastward to Sicily and Calabria (Figure 2.1).

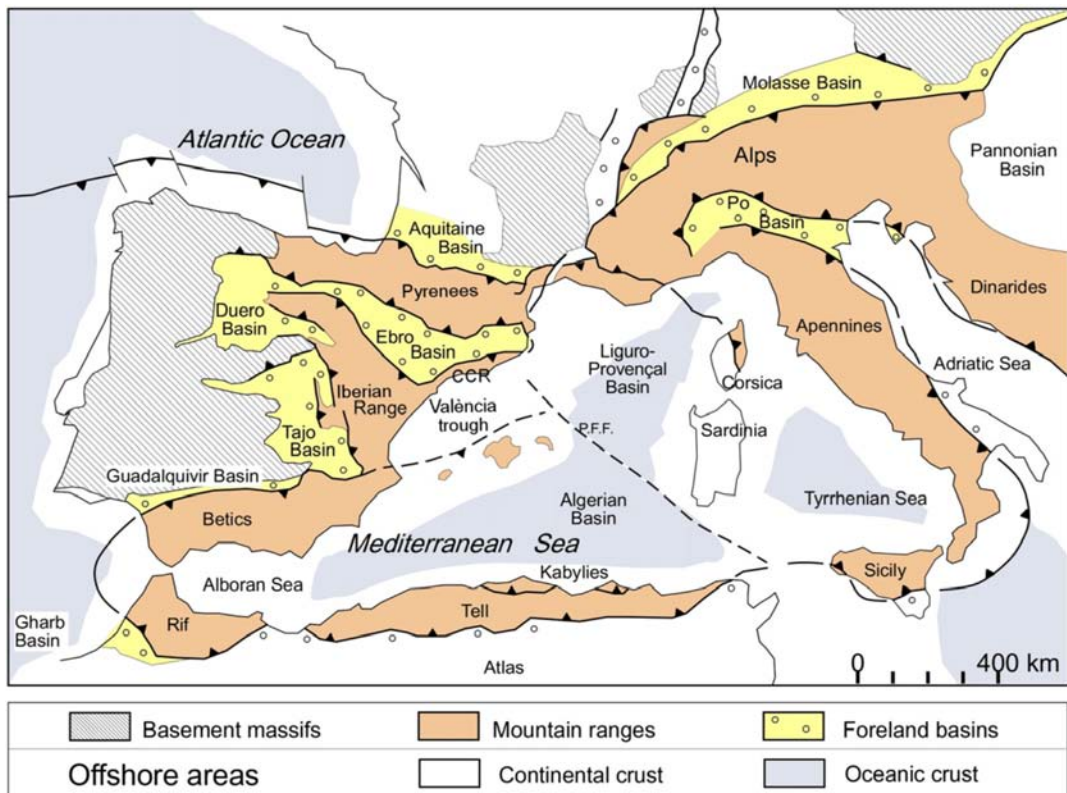


**Figure 2.1:** Tectonic map of the western Mediterranean region showing the main orogenic belts and foreland basins (from Vergés and Sàbat, 1999)

## 2.2 Geology of North Morocco

### 2.2.1 Rif Cordillera

The Rif Cordillera is bounded the west and south by the Gharb and Saïss Basins respectively, and to the east by the Middle Atlas (Figure 2.2). The range extends for around 500 km roughly from Nador to the east to Sebta (Ceuta) to the north. Similar to the Betic Ranges and other Alpine Mediterranean cordilleras, the Rif Cordillera consists of Internal and External Zones, separated by Flysch domain (Durand Delga et al., 1962; Andrieux, 1971; Kornprobst, 1974; Frizon de la Motte, 1985).

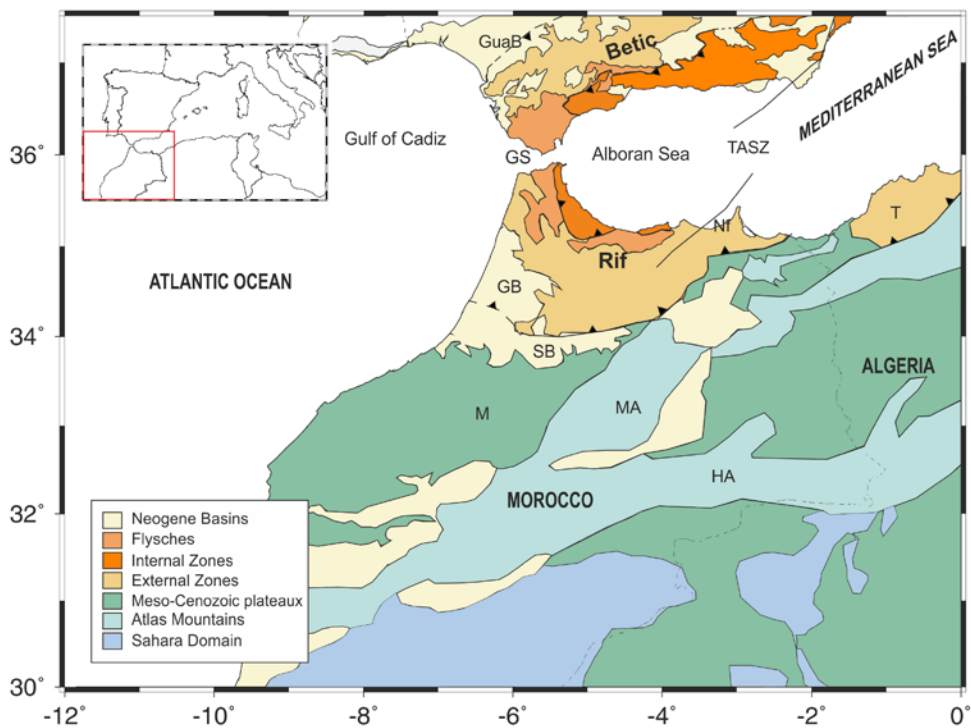


**Figure 2.2:** Map of southern Iberian and northern Morocco with the location and simplified geology of the study area. The major tectonic domains and boundaries are identified. GB: Gharb Basin; Guab: Guadalquivir Basin; GS: Gibraltar Strait; HA: High Atlas; M: Meseta; MA: Middle Atlas; Nf: Nekkor fault; SB: Saïss Basin; TASZ: Trans-Alboran Shear Zone. The inside shows the location of the study area with respect to the Europe continent.

### *Internal Zones*

The Internal zones are formed by Paleozoic, Mesozoic and Cenozoic sequences, including metamorphic complexes that have been affected by Alpine deformation since the Eocene-Late Oligocene (Chalouan et al., 2001, 2008). Since the Late Miocene, continued compression has formed normal faults in the upper crustal levels of the Internal Zones, providing the relief of the modern Rif. The Internal Zones include three main metamorphic complexes: the Sebtides, the Ghomarides and the Dorsale Calcaire.

The Sebtides complex (equivalent to the Betics Alpujarride complex) is a stack of metamorphic units. It consists of relatively deep crustal rocks such as mica-schists, migmatites and granulites associated with mantle peridotites of Beni-Bousera (Balanyá et al., 1997; Bauybaouene et al., 1998).

The Ghomarides complex overlies the Sebtides and is equivalent to the Betic Malaguide. It includes four nappes of low-grade Paleozoic metasediments covered by thick, unconformable Triassic red beds, and much thinner Liassic, Paleocene-Eocene limestone (Chalouan and Michard, 1990).

The Dorsale Calcaire complex consists of stacked carbonate slabs platform to passive margin deposits with thin cover of Jurassic-Late Cretaceous pelagic and Tertiary detrital sediments (El Kadiri et al., 1992; Chalouan et al., 2001).

### *External Zones*

The External Zones of each limb of the Gibraltar Arc originated from two distinct paleomargins of Africa and Iberia, respectively. Therefore, contrary to the Internal Zones and Flyschs nappes, the Rif External Zones do not display any stratigraphic/structural continuity across the Strait of Gibraltar, except in the uppermost and youngest units of the accretionary prisms located offshore in the Gulf of Cadiz (Chalouan et al., 2008).

The Extrenal Zones comprise carbonate and pelitic Mesozoic and Cenozoic units, mainly limestone and marls. In the Rif, they form a fold-and-thrust belt detached along Late Triassic evaporite beds above the thinned continental crust of the North Africa

passive margin (Wildi, 1983; Chalouan et al., 2008). Three structural zones may be distinguished, from north to south and from top to bottom, the Intrarif, Mesorif and Prerif, which derive from more and more proximal parts of the African palomargin, respectively.

### *Flysch domain*

The Flysch domain is composed of Cretaceous-Lower Miocene detritic rocks outcropping at more than 7000 km from the Betic-Maghrebian belt to the Balkian including Apennines, Alps, Dinarides, Hellenides and Carpathians. The Flysch domain forms a tectonic edifice, widespread along the whole Betic-Maghrebian belt and made up by several tectonic units which are piled up and overthrust onto the external deposits (Puglisi, 2009). They overthrust the external Rif units with the exception of some klippe that are located on the Internal Zones as the result of the complex evolution involving back-trusting or back-sliding (Chalouan et al., 1995; El Mirihi, 2005). The Flysch domain is formed by two nappes, the internal higher units, which are named Mauretanian, and the external and lower units, the Masylian nappes. Turbidite sequences, also called flyshs, are dominant in these nappes, but clay-dominated sequences occur at the bottom of each nappe, named pre-flyshs, (Chalouan et al., 2008).

### **2.2.2 Alboran Basin**

In Early-Middle Miocene, after crustal thickening and metamorphism, the region began to undergo EW to NE-SW extension that thinned the continental crust along normal faults forming the Alboran Basin (Chalouan et al., 2008). This is a synorogenic basin with a thinning continental crust, which incorporates stretched elements of the orogen. It has a thick Neogene overlying deep crustal rocks locally recognized as belonging to the Sebtides-Alpujarride nappes.

Up to 8 km of turbidites and muds accumulated in the western sub-basin where numerous mud diapirs occur. In the central and eastern parts of the basin, as well as on its southern and northern borders, an important cal-alkaline magmatism developed during the Middle-Late Miocene. This is the Trans-Alboran magmatic province.

The Eastern part of the Alboran Basin includes the so-called Trans-Alboran Shear Zone (TASZ), a broad fault zone, composed of different left-lateral strike-slip fault

segments running from the eastern Betics to the Alhoceima region in the Rif and resulting in a major bathymetric high in the Alboran Sea, that affects the Neogene basins of the region (Udías and Buforn, 1992; Martínez-Díaz et al., 2001).

### 2.2.3 Foreland Basins

The Gharb (or Rharb) and Saïss basins are foreland basins separating the Rif belt from the Moroccan Meseta and Middle Atlas, and they form a roughly EW trending Late-Miocene, Pleistocene trough that covers the western part of the South Rifian Corridor (Hadif et al., 2008). Those basins have a structural origin and develop adjacent and parallel to a mountain belt. They were formed (DeCelles and Giles, 1996; DeCelles, 2012) due to the immense mass created by crustal thickening associated with the lithospheric flexure. The width and depth of the foreland basins is determined by the flexure rigidity of the underlying lithosphere, and the characteristics of the mountain belt.

The Gharb basin contain part of the Prerif nappe surmounted by a large amount of continental sediments reaching, in the case of the Gharb Basin, a maximum depth of 8 km towards the west (Hadif et al., 2008). The basin was moreover filled with sediments of marine origin during the Tertiary and continental formations during the Quaternary, except for a coastal fringe (Hadif et al., 2008) and evolved as a foreland basin as the basement was loaded by the thrust sheets of the External Units (Fernàndez et al., 1998; García-Castellanos, 2002; Vergés and Fernàndez, 2012).

The Guadalquivir basin is locate at north of the Betic Range, the northern branch of the Gibraltar Arc. This basis was formed during the Neogene, and was emplaced on a Hercynian basement. It is the foreland on the Subbetic nappes and it opens WSW directly to the Atlantic, in the Gulf of Cádiz area (Saenz de Galdeano and Vera, 1992). This basin is filled by Neogene to Quaternary rocks. This basin is formed by clays and marls, with locally developed tick bodies of sandstone turbidites (Azañón et al., 2002; Alonso-Zaraza et al., 2002).

## 2.3 Previous Geophysical Studies

Early geophysical studies of the Rif in the 70's consisting of low-density seismic refraction by Hatzfeld and Bensari, (1977) reported a crustal thickness of 30 km beneath the Gharb Basin. Beneath the Alboran Sea, wide-angle profiles (also in the 70's) constrain Moho-depths of 18-20 km beneath the central part of the basin (Working Group for Deep Seismic Sounding in Alboran 1974, 1978). Wigger et al. (1992) report crustal thicknesses of 35 km beneath the southernmost Rif determined by refraction recordings of quarry blasts.

Torne et al. (2000) used gravity, heat flow and elevation data to estimate crust and mantle lithosphere thickness beneath the Alboran basin, the Betics and the Rif Cordilleras. They found that crustal thickness between the orogenic belts and the Alboran Sea may differ by as much as 25 km. These models were further refined by including constraints from the Geoid anomalies (Frizon de Lamotte et al., 2004; Zeyen et al., 2005) and possible petrological compositions (Fullea et al., 2010, 2014). These resulted in a moderately thick crust underneath the Rif and Betics (~32-34 km), and a thin continental crust (~18-22 km) beneath the Alboran basin. This basin progressively thins towards the east, reaching values less than 16 km depth at the transition to the Algerian basin. In the Moroccan interior, crustal thickness increases to 38 km below the highest elevations of the High Atlas, then it decreases to the southeast to 30-32 km.

Results from a NW-SE oriented magnetotelluric profile across the Rif (Anahnah et al., 2011a) show a heterogeneous upper crust, with resistive (metamorphic rocks) and conductive (peridotites) bodies in the uppermost 10 km of the Internal Zones, and highly conductive bodies in the External Zones and foreland basin. The variable thicknesses of the latter ones suggest the presence of basement highs that may be related to blind frontal thrusts between the Gharb Basin and the External Zones. A crustal detachment level separating shallow geological units from a probable Variscan basement was inferred. At depths below 5 km, relatively large resistive bodies appear below the frontal part of the Rif. The southern Rif has also been modeled using magnetotelluric data, featuring wide and thin conductive bodies interpreted to correspond to detrital rocks that alternate with marl and carbonates (Anahnah et al., 2011b).

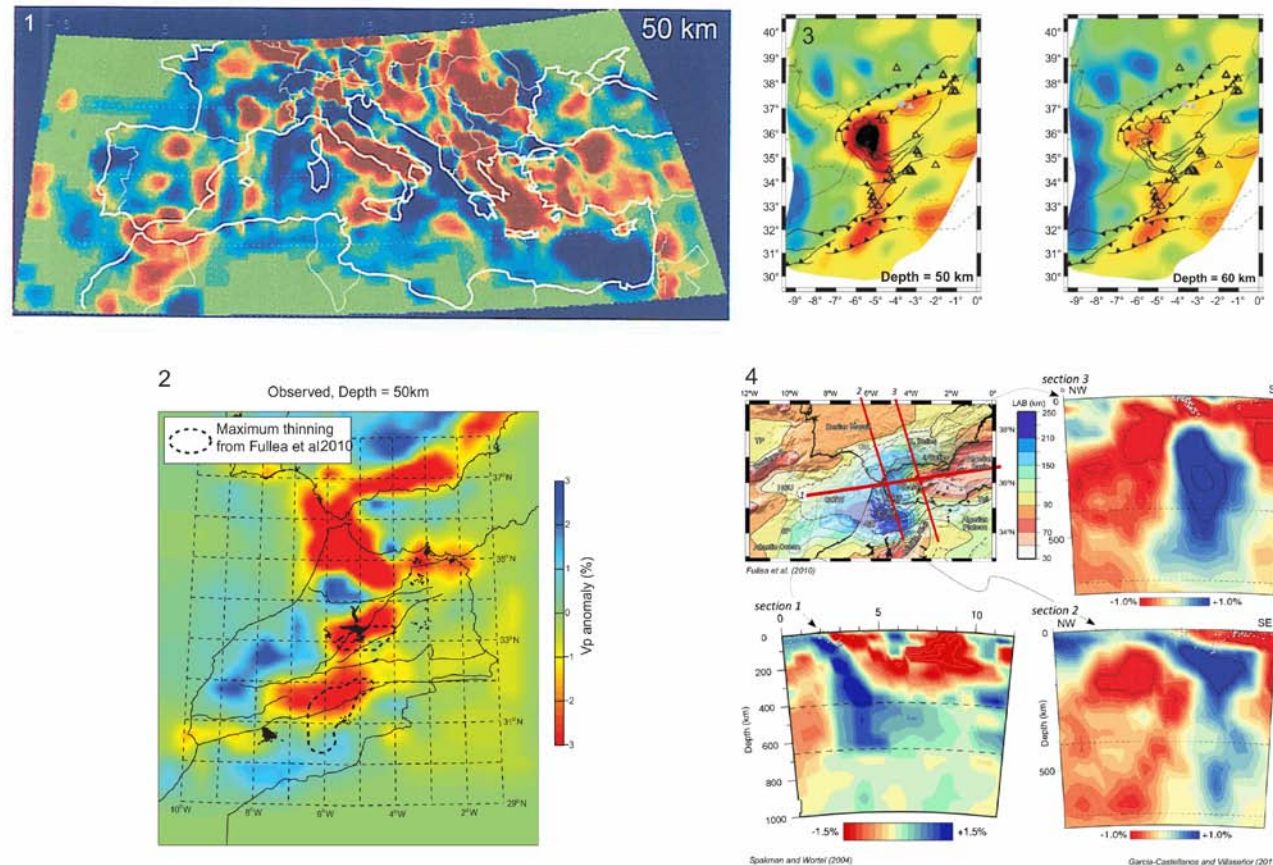
Eurasian convergence relative to Africa trended south during the Late Cretaceous-Paleogene, and has trended southeast oblique to the African margin from the Miocene. The present-day tectonic motions in the study area are constrained from GPS observations on permanent sites and temporary deployments (Fadil et al., 2006; Vernant et al., 2010; Koulali et al., 2011) combined with other stress indicators (Palano et al., 2013). They show south to southeast motion at ~5 mm/year of the Rif region relative to stable Nubia. The Rif, Betics and Alboran Sea are an active seismic zone, with the Rif interpreted as a wide transpressive zone between the seismically active Tell to the east, and the oceanic transform fault plate boundary to the west. This is interpreted as additional evidence of subduction roll-back, corresponding to the contact area between two converging plates, Eurasia and Africa.

Local earthquake travel-time tomography using data from the Topo-Iberia and PICASSO arrays of the Gibraltar Arc (El Moudnib et al., submitted) have significantly enhanced the previous models presented by Gurría and Mezcua (2000) and Calvert et al. (2000a). At the uppermost crustal levels low velocities (5.5-5.75 km/s) are observed beneath the Betics and the Alhoceima region, while the velocities beneath the Rif remain close to the 1-D IGN reference model (Gurría and Mezcua, 2000). At ~30 km depth, a low velocity zone (6.3-6.7 km/s) clearly underlies the Gibraltar Arc from the easternmost Betics to the southeastern Rif, where an abrupt change in velocity is observed. Low shear velocities have been determined in the same region from Rayleigh wave tomography (Palomeras et al., 2014). Calvert et al. (2000b) and Serrano et al. (2005) used seismic regional waveforms to map Pn velocities along the Africa-Iberia boundary. A robust low-Pn (<7.8 kms<sup>-1</sup>) velocity anomaly is imaged beneath the Betics, in contrast with the relatively normal values beneath the Alboran Sea. The Rif and Middle Atlas show also low Pn velocities. Díaz et al. (2013) resolved similar patterns and a local area of high Pn and Sn velocities (>7.8 kms<sup>-1</sup> and >4.8 kms<sup>-1</sup>, respectively) beneath the Alhoceima region (approx. 35°N, 3°W).

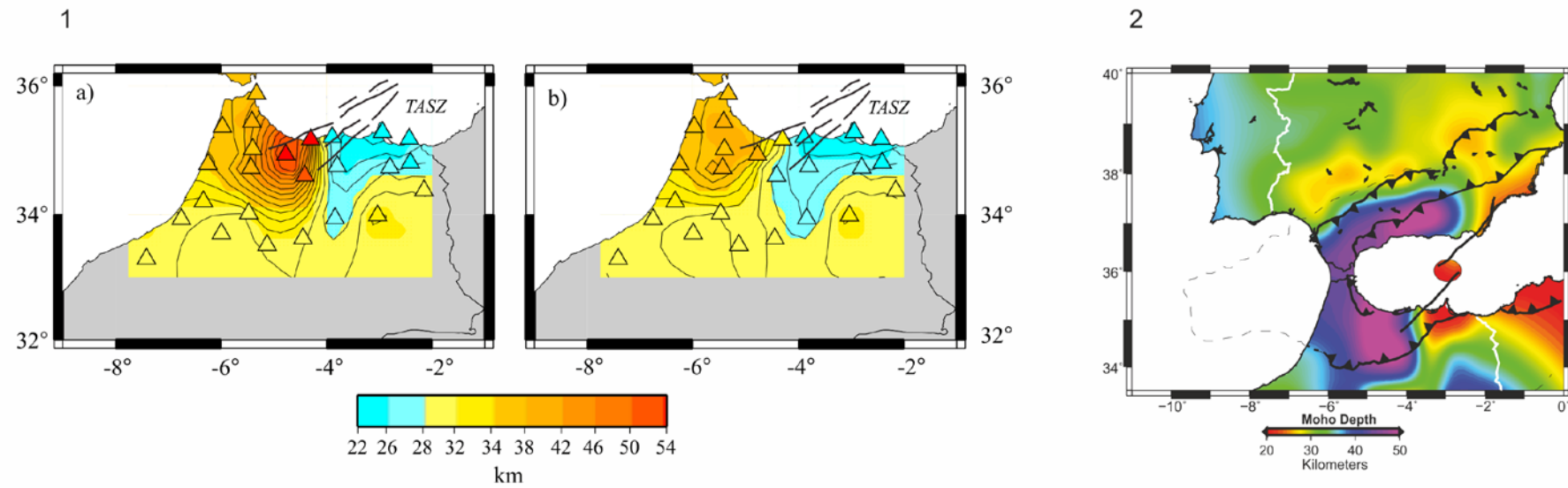
Regional 3-D teleseismic tomography (Bezada et al., 2013) images a high velocity slab-like feature beneath the Alboran Sea and much of the eastern Betics from lithospheric depths to >600 km (Figure 2.3). The geometry supports slab tearing beneath the eastern Betics, suggested previously by Spakman and Wortel (2004) and

Garcia-Castellanos and Villaseñor (2011). Rayleigh wave tomography and receiver function images of the western Mediterranean (Palomeras et al., 2014; Thurner et al., 2014) suggest that the slab is attached to the crust beneath the Rif Cordillera, suggested also by Pérouse et al. (2010) from GPS observations.

SKS split directions rotate around the Gibraltar Arc with the fast directions following the curvature of the Rif-Betic chain (Buontempo et al., 2008; Díaz et al., 2010; Miller et al., 2013; Díaz and Gallart, 2014). This is interpreted as evidence of asthenospheric mantle flow around the Alboran slab (Díaz et al., 2010; Alpert et al., 2013; Díaz and Gallart, 2014). Recent Topo-Iberia and PICASSO receiver function studies (Mancilla et al., 2012; Thurner et al., 2014) show large variations in crustal thickness beneath northern Morocco (Figure 2.4), with a clearly defined localized crustal root beneath the central Rif extending to 40-50 km, and significantly thinner crustal thicknesses of 22-30 km beneath northeastern Morocco, although the studies differ in detail. The eastern limit of the Rif Cordillera, in the transition between both areas, shows complex converted Ps signals admitting different interpretations. Thurner et al. (2014) identified a subcrustal horizon beneath the Betic and Rif Cordilleras, located between 45 and 80 km depth, which are interpreted as the top of the Alboran Sea slab merging with the Moho at 50-55 km depth.



**Figure 2.3:** Previous tomographic models in the area. 1) P-wave tomographic map for a depth of 50 km of the western Mediterranean (from Piromallo et al., 1997), 2) P-wave tomography map for a depth of 50 km of the Gibraltar Arc System and Atlas Mountains (from Bezada et al., 2014), 3) Shear waves tomography at depth of 50 and 60 km of the Gibraltar Arc System (from Palomeras et al., 2014), and 4) P-wave tomographic sections along the Gibraltar Arc System (from Spakman and Wortel, 2004; García-Castellano and Villaseñor, 2011).



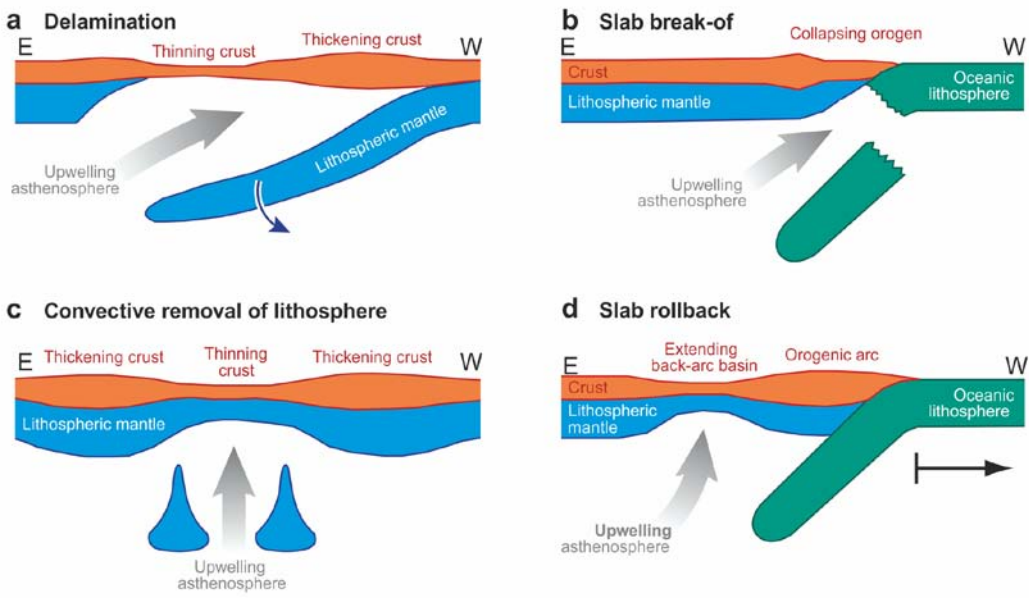
**Figure 2.4:** Moho depth maps obtained from previous receiver functions studies. 1) Two options of Moho depth maps from Mancilla et al. (2014). Moho depth map from Thurner et al. (2014)

Figure 3

## 2.4 Geodynamic models

The Betic-Rif arc may be considered as one of the tightest and smallest orogenic arcs on Earth. Numerous, often incompatible geodynamic models have been proposed to explain the singular configuration of the Gibraltar Arc System (Figure 2.5), from processes including a continental scale thermal mantle source driving rifting from the Rhine Graben into the westernmost Mediterranean (Hoernle et al., 1995) to models suggesting regional scale recycling of the lithosphere by delamination (Seber et al., 1996), slab break-off (Blanco and Spakman, 1993; Zeck et al., 1996), convective removal (Platt and Vissers, 1989) or active eastward subduction of oceanic crust (Gutscher et al., 2002). The formation of an arcuate orogen must be reflected in the geometry of the subducting slab, and the dynamics of the subduction process likely exert substantial control on the geometry of the arc. However, development of the arc requires significant strain in the back-arc region, and the dynamics of this process may also exert control (Facceba et al., 2204; Platt et al., 2013).

Many authors now relate the origin of the Gibraltar Arc to the segmentation of the Western Mediterranean Subduction Zone (WMSZ) and the fast westward oriented retreat of the subsequent narrow slab of oceanic lithosphere (Royden, 1993; Lonergan and White, 1997; Rosenbaum and Lister, 2004; Faccenna et al., 2004; Jolivet et al., 2009; Vergés and Fernández, 2012). Recent mantle studies of this region suggest subduction related convective recycling and delamination of mantle lithosphere from the crust (Bezada et al, 2013; Palomeras et al, 2014; Thurner et al, 2014). However, large uncertainties remain on major points of such hypothesis.



**Figure 2.5:** Models previously proposed to explain the geodynamic evolution of the Alboran region: (a) delamination (e.g. Platt et al., 1996), b) slab break-off (e.g. Blanco and Spakman, 1993), c) convective removal or lithosphere (e.g. Seber et al., 1996), and d) slab rollback (e.g. Rouden, 1993; Lonegan and White, 1997). These entire hypotheses involve the sinking of negative buoyant lithosphere and rising positively buoyant asthenosphere mantle (from Platt et al., 2013)

## Chapter 3: Methodological approaches

Even if there is a large amount of bibliography dealing with the seismic methodologies used in this work (e.g. Stein and Wysession, 2003; Shear, 2009), we think that it is convenient to include a summary of the techniques considered during this thesis. Therefore, this chapter is devoted to present the basic concepts related to Pn/Sn tomography, wide-angle reflection/refraction deep seismic sounding profiles and teleseismic receiver functions.

The seismic methods are widely recognized as one of the more powerful tools for the investigation of the physical properties of the Earth's interior. The existence of the crust was first put on evidence by A. Mohorovičić one century ago from the inspection of the scarce seismic records available of an earthquake in the Kupavally (Croatia). By 1910, the presence of a core in the center of the planet was proposed by R. Oldham and B. Gutenberg to explain the anomalies in the propagation of the seismic waves at large distances. Later on, in 1936, I. Lehman showed the existence of a differentiated inner core again from the analysis of seismic wave propagation times. The 3-D density structure inside the Earth's mantle and core has been deduced in large part from the analysis of the normal modes of resonance recorded after large earthquakes. Therefore, the analysis of seismic data was basic to understand the structure of the Earth (Figure 3.1).

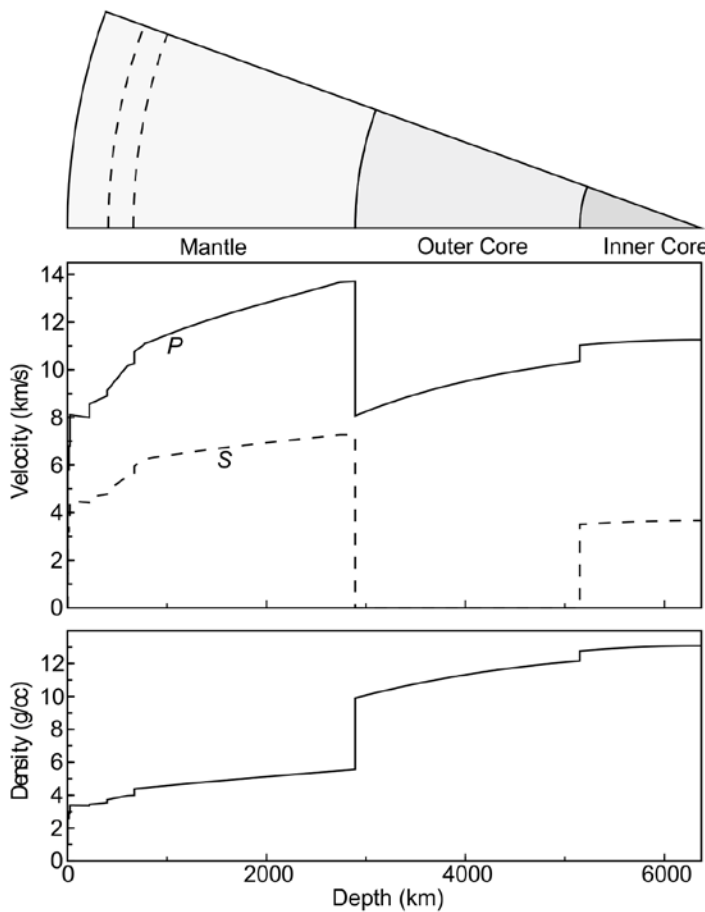


**Figure 3.1:** Earth's P-wave velocity, S-wave velocity, and density profiles as a function of depth. Values are from the Dziewonski and Anderson (1981) Preliminary Reference Earth Model (Shear, 2009).

### 3.1 *Pn/Sn* Travel-time tomography

Seismic tomography was first developed in the mid-70s to obtain 3-D images of the distribution of velocities in the interior of the Earth (Aki et al., 1974, 1977; Paige and Saundes, 1982). Its objective is to obtain 2-D or 3-D images of the Earth's interior using the seismic rays propagating through it along different directions. In a homogeneous Earth, the time taken for a seismic wave to reach a point in the Earth surface will only depend on the distance between this point and the earthquake source. If a zone with anomalous high/slow seismic velocities exists, the rays traversing it will arrive before/after than the rays traveling outside. With a large coverage of earthquakes and receivers and a powerful computer treatment it is possible to map in detail the heterogeneity of the Earth interior following this approach. A similar method is used in

medical scanners, in which X-ray are shot and recorded in all directions through a patient body to study propagation anomalies. In the seismic case, the irregular distribution of sources and receivers, the uncertainty in the time and locations of the source and the errors in the picking of time arrivals will result in blurred images. Nevertheless, seismic tomography has proved to be one of the most powerful techniques to investigate the Earth's interior.

There are different type of seismic tomographies, depending on the set of source used (ambient noise, local or teleseismic events), the type of waves studied (compression P- or shear S-waves, surface waves), the analyzed property (travel-time, full waveform) or the mathematical approach followed to derive the final images. In this thesis we will focus in a special case of travel-time seismic tomography usually known as Pn/Sn tomography. We apply the technique developed by Hearn (1996), widely used in the seismological community, to invert the Pn or Sn travel-time arrivals reported in the International Seismological Center catalog. This method provides information on lateral seismic velocity variations, anisotropic properties and crustal thicknesses. Due to the shallow velocity gradient in the uppermost mantle and to the large contrast with lower crust velocities, Pn and Sn phases are confined in depth and thus the analysis of their travel-time variations provides insights on the velocity variations in the uppermost mantle. This methodology complements global and regional body-wave tomographies, that average velocity changes over large depth intervals and are very dependent on the crustal correction term, as well as surface-wave studies, which provide good vertical resolution but tend to smooth variations horizontally. The observed variations in the Pn and Sn velocities can be associated to changes in the temperature, pressure, composition or water content conditions. The anisotropic parameters to be derived from such kind of analysis constrain the mantle dynamics, as they can be related to the alignment of aggregate olivine crystals. Therefore, this method provides significant clues on the structure and dynamics of the uppermost mantle region.

### 3.1.1 Data selection

The first step in this kind of studies is the selection of the input data. In this case we have used the time arrivals reported at the International Seismological Center (ISC) catalogue (International Seismological Center, 2010) during the time interval 1990–2010, with epicenters and/or recording stations within the  $20^{\circ}\text{N}/55^{\circ}\text{N}$  –  $30^{\circ}\text{W}/30^{\circ}\text{E}$  region. We have tried to extend the southward limit of the investigated area, but the lack of seismic stations southward of the Tell-Atlas chain does not allow recovery of appropriate Pn phases. Data prior to 1990 has not been included because the number of available seismic stations has grown significantly in the last 2 decades, providing great increase in the amount of observations and thus in the accuracy of the catalogs. We estimate that using the whole time range of the catalog may have a negative effect because although the number of travel-time readings increases, its accuracy clearly decreases. The phases with travel-times exceeding by more than 30 s the theoretical time have been directly excluded to avoid readings affected typically by 1 minute errors.

Figure 3.2 shows the travel-time arrivals recovered from the catalog.

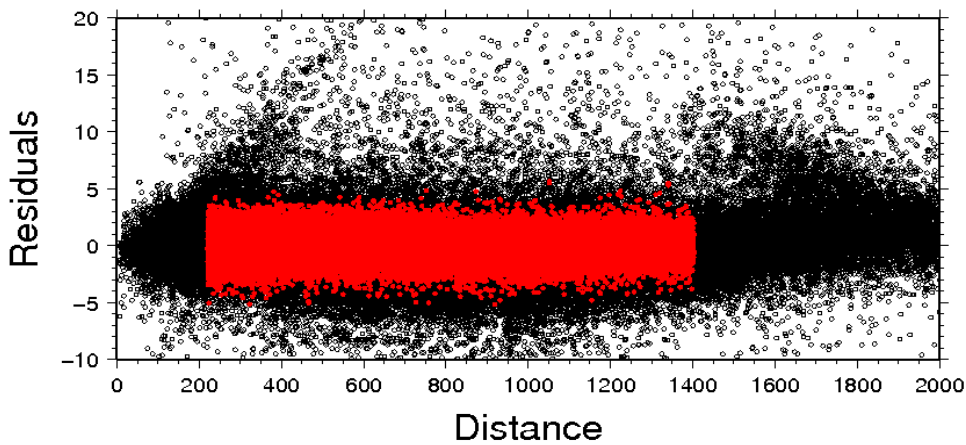


**Figure 3.2:**  $P$  phases obtained as a function of distance and the residual time (difference between the measured time and the theoretical one assuming  $V_p = 8 \text{ km/s}$ ). In black are represented all the  $P$  phases obtained from the catalogs, and in red the selected data as input data.

Pn phases are defined as head waves travelling within the uppermost mantle just beneath the Moho discontinuity, with velocities close to 8.0 km/s. However, in an area geodynamically very complex such as the Mediterranean region, it is very difficult to

clearly identify such waves. Following classical approaches, we assumed that any phase which travel-time verifies appropriate selection criteria may be treated as a real Pn phase (Figure 3.2). These selection criteria are: (1) hypocentral depths less than 35 km; this avoids considering subcrustal earthquakes which will not generate Pn phases. We have chosen a realistic reference value, even if changes in crustal depths beneath the Mediterranean region are very important; (2) epicentral distances ranging from 220 to 1440 km ( $2.0^\circ$  to  $12.60^\circ$ ); those values were determined from the inspection of the time-distance plot of all available wave picks; (3) initial residuals smaller than 6 s; (4) residuals smaller than 3 s after the adjustment of the mean Pn velocity; (5) each retained event must be recorded at a minimum of five stations and each retained station must have arrivals from five or more events. These selection criteria have also been considered for the Sn phases, assuming a typical Vp/Vs ratio of 1.73.

We have to create a simple C program called “treuEvent\_P\_Pn” which allows selecting from the catalogue the travel-times which are described as P or Pn (S or Sn) (see Figure 3.3). Next step has been to design a script to gather the required information (phase identification, event origin time and location, station location and name, precision of the picking) and build the input file for the tomographic (Figure 3.4).

Event	1750349	France	Date	Time	Err	RMS	Latitude	Longitude	Smaj	Smin	Az	Depth	Err	Ndef	Nsta	Gap	Mdist	Mdist	Qual	Author	OrigID
2000/01/01	03:20:57.30f						48.1190	-2.9590f			3.0f		9	107	0.25	5.59	se	NEIC	3050145		
(After LDG.)																					
2000/01/01	03:20:57.30		0.18				48.1194	-2.9586	4.100	2.800	6	3.0f		25	12	0.25	5.59	ke	LDG	3028341	
2000/01/01	03:20:56.09		1.13	0.990			48.1080	-3.0320	14.38	11.99	90	24.5	14.8	9	12	119	0.21	5.60	m i	ISC	3629958
(#PRIME)																					
Magnitude	Err	Nsta	Author	OrigID																	
ML	2.7		LDG	3050145																	
Md	2.9		1	LDG																	
Ml	2.7	0.2	8	LDG																	
Sta	Dist	EvAz	Phase	Time	TRes	Azim	AzRes	Slow	SRes	Def	SNR	Amp	Per	Qual	Magnitude	ArrID					
QUIF	0.21	205.2	P*	03:21:02.3		0.5				T—										42562113	
QUIF	0.21	205.2	Sg	03:21:05.6						T—		33.6	0.17	_e						42562114	
ROSF	0.28	324.8	P*	03:21:02.5		-0.26				T—										42562115	
ROSF	0.28	324.8	Sg	03:21:05.6						T—		17.1	0.14	_e						42562116	
SGMF	0.35	65.1	P*	03:21:03.5		-0.31				T—										42562117	
SGMF	0.35	65.1	Sg	03:21:06.9						T—		20.2	0.16	_e						42562118	
GRR	1.48	78.3	PN	03:21:24.4		3.0				T—										42562119	
GRR	1.48	78.3	Sg	03:21:43.1						T—		10.1	0.16	_e						42562120	
HYF	3.92	100.3	PN	03:21:56.3		0.1				T—										42562121	
HYF	3.92	100.3	Sg	03:23:00.1						T—										42562122	
TCF	4.01	115.1	Sg	03:23:00.6						T—		2.1	0.47	_e						42562134	
BGF	4.29	109.0	Sg	03:23:11.3						T—		3.9	0.38	_e						42562137	
AVF	4.53	104.6	PN	03:22:04.4		-0.39				T—										42562123	
AVF	4.53	104.6	Sn	03:22:52.1						T—										42562124	
AVF	4.53	104.6	Sg	03:23:15.2						T—		0.8	0.44	_e						42562125	

**Figure 3.3:** Extract from the ISC seismic catalog where all the information from event 1750549 in France is shown.

35.6320	5.9980	36.8979	-2.8896	1690	7.27	282	74947.10	75057.30	3.7	-0.1	129	0	2000	11	20 EBER	-1 -2 -2
35.4610	-3.7350	36.8979	-2.8896	1690	1.59	25	12661.50	12689.50	3.8	-0.3	143	10	2000	11	28 EBER	-1 -2 -2
36.5330	4.8020	36.8979	-2.8896	1690	6.17	275	06286.40	06377.70	3.7	-1.4	87	17	2000	11	30 EBER	-1 -2 -2
36.4470	4.9410	36.8979	-2.8896	1690	6.29	276	07916.40	08011.00	3.3	-0.7	60	10	2000	11	30 EBER	-1 -2 -2
36.5350	4.7770	36.8979	-2.8896	1690	6.15	275	32925.80	33018.10	3.7	-1.3	84	7	2000	12	8 EBER	-1 -2 -2
36.4520	4.7910	36.8979	-2.8896	1690	6.17	276	64330.40	64423.50	3.6	-0.6	168	9	2000	12	11 EBER	-1 -2 -2
36.5910	4.8100	36.8979	-2.8896	1690	6.18	275	42212.90	42304.80	3.3	-0.7	62	20	2000	12	28 EBER	-1 -2 -2
36.6870	5.2560	36.8979	-2.8896	1690	6.52	274	86320.00	00015.90	3.9	-2.7	83	8	2001	1	23 EBER	-1 -2 -2
36.0010	5.2880	36.8979	-2.8896	1690	6.64	280	56372.40	56472.20	4.0	-0.3	106	10	2001	2	2 EBER	-1 -2 -2
44.0710	8.6460	36.8979	-2.8896	1690	11.31	234	80924.30	81092.20	4.1	3.5	366	13	2001	2	6 EBER	-1 -2 -2
38.3760	-0.7980	36.8979	-2.8896	1690	2.22	228	26015.90	26053.00	3.5	-0.1	53	10	2001	2	10 EBER	-1 -2 -2
43.4670	7.4720	36.8979	-2.8896	1690	10.27	233	66880.60	67032.70	3.9	1.5	497	10	2001	2	25 EBER	-1 -2 -2
37.0450	-9.9850	36.8979	-2.8896	1690	5.67	89	28701.10	28788.10	3.9	0.5	197	10	2001	4	9 EBER	-1 -2 -2
39.8620	-8.6610	36.8979	-2.8896	1690	5.37	121	53333.50	53416.10	4.1	1.1	248	14	2001	4	10 EBER	-1 -2 -2
38.4543	-0.6760	36.8979	-2.8896	1690	2.34	229	02615.70	02653.50	2.9	0.0	56	2	2001	4	16 EBER	-1 -2 -2
36.3688	0.4311	36.8979	-2.8896	1690	2.72	282	06771.80	06815.10	2.1	0.0	25	0	2001	5	13 EBER	-1 -2 -2
42.8860	-7.6120	36.8979	-2.8896	1690	6.93	146	05946.90	06053.10	4.7	2.2	197	10	2001	5	20 EBER	-1 -2 -2
35.7388	-0.1823	36.8979	-2.8896	1690	2.47	298	47010.20	47048.30	3.4	0.0	40	18	2001	5	29 EBER	-1 -2 -2
35.8193	-0.6831	36.8979	-2.8896	1690	2.08	301	86076.50	86108.60	3.3	0.0	28	24	2001	6	1 EBER	-1 -2 -2
35.7349	-3.8126	36.8979	-2.8896	1690	1.38	32	22957.70	22982.60	2.6	0.0	15	0	2001	6	12 EBER	-1 -2 -2
34.3320	-6.4970	36.8979	-2.8896	1690	3.90	47	55304.30	55363.60	3.7	0.3	312	33	2001	6	28 EBER	-1 -2 -2
38.3512	-1.2655	36.8979	-2.8896	1690	1.94	222	71529.70	71562.00	2.2	0.0	31	10	2001	7	6 EBER	-1 -2 -2
35.1547	-4.7044	36.8979	-2.8896	1690	2.28	39	21888.40	21923.20	2.5	0.0	56	28	2001	7	8 EBER	-1 -2 -2

**Figure 3.4:** Extract from the input data to arrange the  $P_n$  tomography. The first two columns correspond to the event location, followed by the station location and elevation in meters. The next columns refers to distance station-event in degrees; azimuth; event time in seconds; the arrival to the station in seconds; magnitude of the event; residual time in second; number of stations which recorded this event; event depth; date (year, month and day); precision in the pick; precision in the event latitude; and finally the precision in the event longitude. The same procedure was performed for the  $S_n$  data

### 3.1.2 Method

We followed the classical method of Hearn (1996) for inverting  $P_n$  and  $S_n$  traveltimes both for isotropic velocity variations and transverse anisotropy perturbations.

If no anisotropy is considered, the travel-time between the  $i$  event and the  $j$  station can be expressed as:

$$t_{ij} = a_i + b_j + \sum d_{ijk} s_k$$

where  $a_i$  and  $b_j$  are, respectively, the static delays for event  $i$  and station  $j$ ,  $d_{ijk}$  is the distance travelled by the ray within cell  $k$  and  $s_k$  is the slowness ( $1/v$ ) in this cell. The station delay depends on the crustal thickness and the velocity beneath the station, but may also include errors derived from timing problems or from erroneous picking of the phase arrivals. The event term can, in addition, contain the effect of mislocations of the event.

The sum is calculated over all the cells traversed by the ray, and the three unknowns  $a_i$ ,  $b_j$ , and  $s_k$  are retrieved from the whole set of equations using regularized least squares with a preconditioned version of the LSQR algorithm (Paige and Saunders, 1982), which requires the use of a regularization or damping parameter. Further details

of the technique can be found in Hearn and Ni, (1994) and Hearn (1996). Thus, features and smoothness of the final model depend on the chosen size of the cells and the value of the smoothing parameter used.

Previous works have already shown than better results are obtained if we consider the presence of anisotropy. In this case, assuming that the anisotropy in the uppermost mantle can be properly described by a  $2\theta$  azimuthal term, the equation to solve will be:

$$t_{ij} = a_i + b_j + \sum d_{ijk} (s_k + A_k \sin 2\theta + B_k \cos 2\theta)$$

$A_k$  and  $B_k$  are the anisotropic parameters for cell  $k$  and  $\theta$  is the backazimuth. The size of the anisotropy at cell  $k$  is related to  $(A_k^2 + B_k^2)^{1/2}$  and the azimuth of the fast direction of propagation will be given by  $\frac{1}{2} \arctan(B_k/A_k) + 90^\circ$ . In this case, two damping factors must be used, one controlling the smoothness of the slowness variations and the other taking care of the anisotropy variations. The ratio between both factors controls the relative weight of the data variance accounted on each kind of variations, and both factors are used to get the right balance between low errors and small resolution width.

The anisotropic term in  $2\theta$  in the Hearn's equations is adapted from the theoretical work of Backus (1965) discussed in the classical review work by Crampin (1981). For P-waves, the dependence on  $\theta$  is:

$$\rho V_p^2 = A + B_c \cos 2\theta + B_s \sin 2\theta + C_c \cos 4\theta + C_s \sin 4\theta$$

where  $\rho$  is the density, and  $A$ ,  $B_c$ ,  $B_s$ ,  $C_c$  and  $C_s$  are combinations of the elastic tensor (see equations 6.2 on Crampin, 1981). In the Hearn's approximation, the terms in  $4\theta$  are not retained due to its small contribution. For S-waves, the equivalent equations are:

$$\begin{aligned} \rho V_{SP}^2 &= D + E_c \cos 4\theta + E_s \sin 4\theta \\ \rho V_{SR}^2 &= F + G_c \cos 2\theta + G_s \sin 2\theta \end{aligned}$$

where  $V_{SP}$  and  $V_{SR}$  refer to the S-waves polarized parallel and perpendicular to the symmetry plane. Assuming a horizontal symmetry plane,  $SR$  can be identified with the

SV polarized phase, contained in the same plane than the P-wave while  $SP$  will correspond to the  $SH$  component. Therefore, the SV polarized wave has a velocity variation with a  $2\theta$  dependence, in a very similar way to P-waves, while the  $SH$  component will vary with  $4\theta$ . Introducing a  $2\theta$  anisotropic term in the  $Sn$  tomographic inversion implies the assumption that the S-wave arrivals identified in the catalogs correspond to SV polarized phases. This hypothesis is not unrealistic, as quite often the S-wave time-arrivals are read in vertical components. Therefore we decided to explore this case, even if we are aware that results should be taken with caution.

The  $Pn$  tomography method assumes that the waves are travelling sub horizontally below the Moho. In case of a significant velocity gradient in the uppermost mantle the ray paths would deviate from this assumption, diving in the mantle lid and thus sampling higher velocities. However, the retained travel-times fit properly along an 8.0 km/s line (Figure 3.5a), without evidences of relevant velocity changes. Furthermore, Figure 3.5(b) shows that a large majority of the used ray paths are less than 600 km in length. It has been tested that the retained travel times for the  $Sn$  phases adjust properly a 4.6 km/s line.

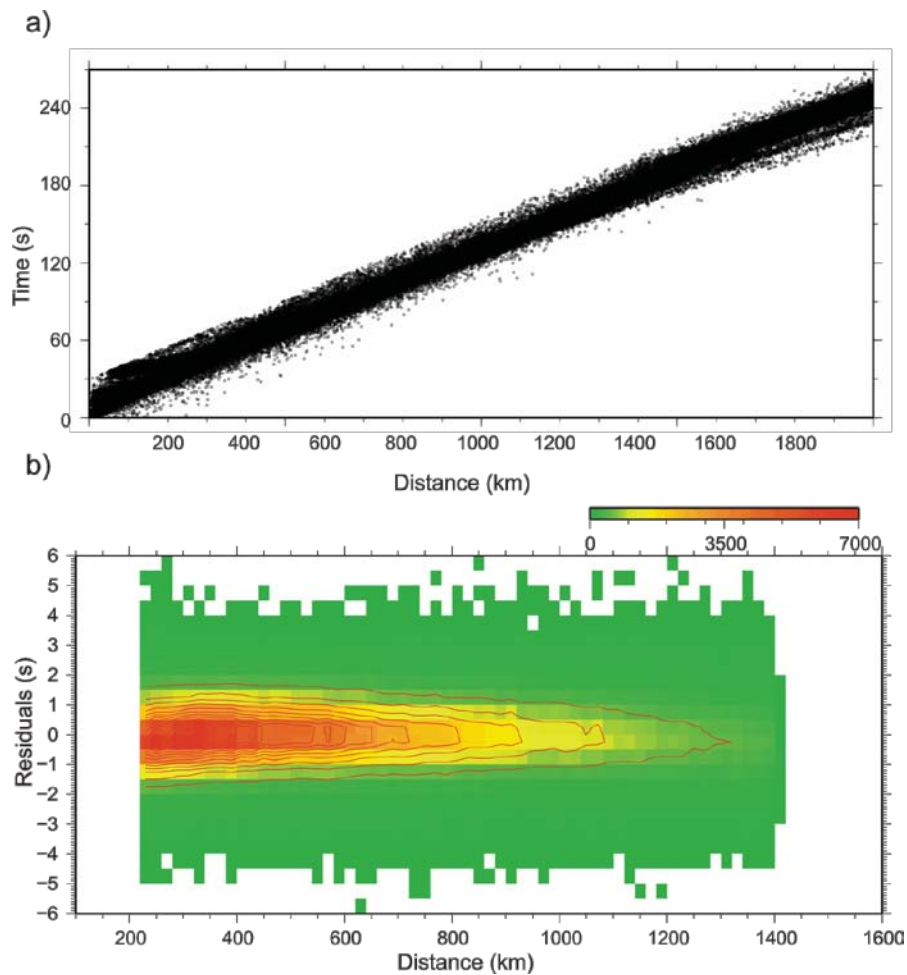


**Figure 3.5:** (a) Total travel-times used in the  $P_n$  tomography study as a function of distance. (b) Retained travel-time observations as a function of the distance and the residual time. Color scale and contours account for the number of retained observations

## 3.2 Active source profiling

Controlled-source seismology (also called “active source seismics”) is one of the primary methods to explore the velocity-depth structure of the Earth’s crust and uppermost mantle. The particular advantage of controlled-source seismology is that it uses man-made seismic sources for which the origin time and location are precisely known. Active source seismology can be used in a large depth range, from the precise mapping of the uppermost sediments using high frequency sources to the identification of the base of the crust and even the properties of the uppermost mantle using large explosions. One of its more successful uses is in oil exploration, becoming the basic tool for the identification of geological structures which may contain oil or gas traps (see Figure 3.6). Active source seismic is classically divided in vertical reflection profiles and refraction/wide-angle reflection profiles.

In vertical seismic reflection profiles, the seismic waves generated by the source are recorded on a large number of receivers located at a short distance. This results in the record of vertically reflected phases which provides a good image of the geometry of the interfaces phases but does not allow getting a good control on the seismic velocities. When used offshore, the typical source is formed by an array of air-guns, generating an air bubble that couples to ground motion when it reaches the sea bottom. Inland, most of the studies rely on the record of arrays of vibrating panels coupled to large trucks which can move quite easily. In both cases, a large number of sources at close distances are shot, providing redundant records (multicoverage) which once processed result in images with large power resolution.

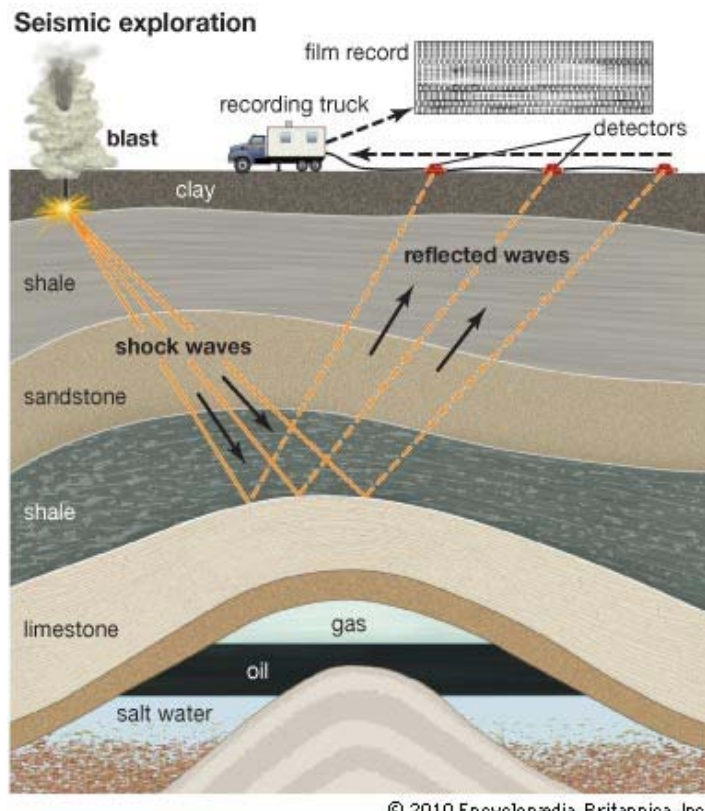


**Figure 3.6:** Schematic representation of a vertical seismic reflection experiment

Refraction/wide-angle reflection method uses a different geometry, in which large explosions (typically generated using chemical explosives) are recorded at distances of hundreds of kilometers by an array of seismic stations. Those receivers are not connected to each other, making fundamental to assure a common time base. This is nowadays assured by precise clocks synchronized to GPS receivers. In this case, the record contains seismic phases which are reflected with wide incidence angle in the seismic discontinuities, as well as phases which are refracted in the same interfaces following the Snell's law. The identification of those phases allows deriving a crustal model providing information not only on the geometry of the reflectors, but also in the seismic velocity of each interface. However, the resolution of the obtained model is typically lower than the provided by vertical refraction profiles.

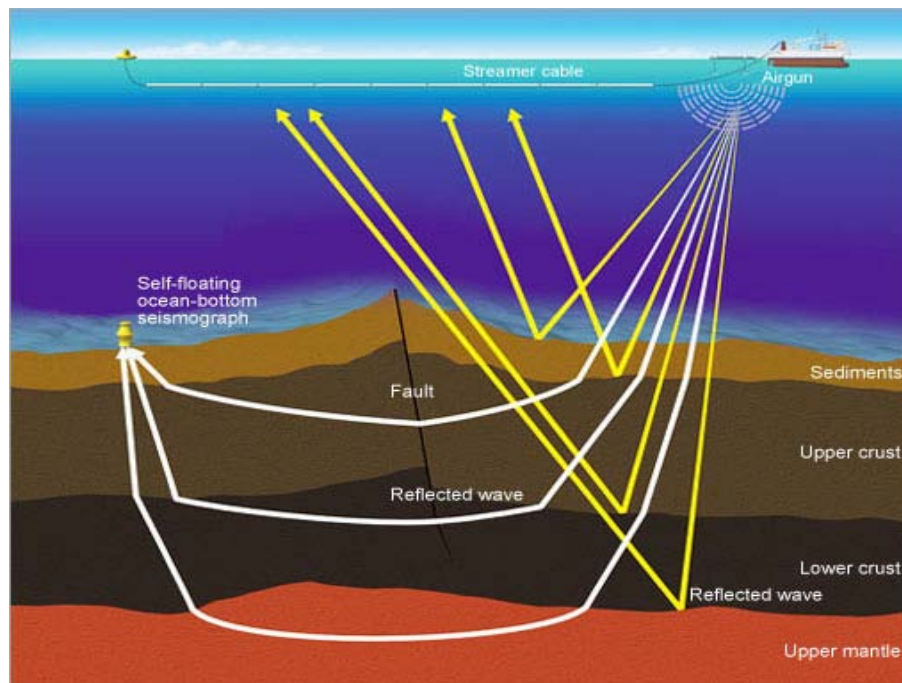


**Figure 3.6:** Schematic representation of the wide-angle seismic experiment and the propagation of the refracted P-waves (in white) and reflected P-waves (in yellow) along the different layers of the crust.

### 3.2.1 Wide-angle reflection /refraction seismic data processing

The data processing starts by sorting by offset (distance to source) the traces of a single shot recorded at all the available stations. The traces are displayed in a Distance-Time reference system usually known as “record section”. To better identify the arrival of the different phases, the vertical axis is expressed in the so-called reduced time (RT):

$$RT = T - D/VR$$

where T is for time, D is for distance and VR is a reduction velocity. The seismic waves travelling with velocities close to VR will appear as horizontal line in the record section, thus being easily identified.

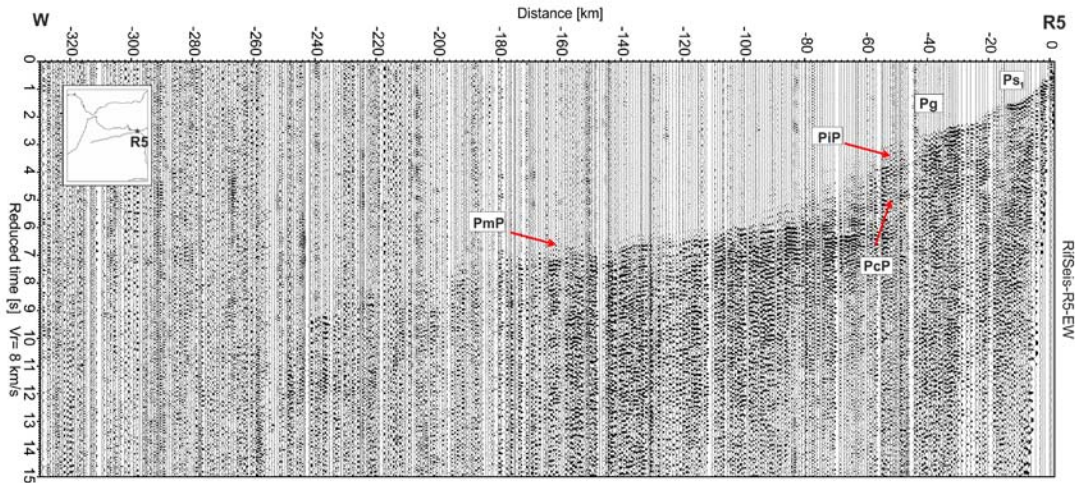


**Figure 3.7:** Example of a wide-angle shot-gather (vertical component). The interpreted phases are labeled following the conventional notation (see text for explanation). Shot displayed with a reduction velocity of 8 km/s with the identified P-wave phases.

We follow the conventional nomenclature to identify the different seismic phases (shown and labeled in the figures):  $Ps$  and  $Pg$  denote refractions through the sedimentary cover and the basement, respectively;  $PiP$ ,  $PcP$  and  $PmP$  stand for  $P$  to  $P$  reflections produced at the top of the middle crust, top of the lower crust and Moho discontinuity, respectively; and  $P1$ ,  $PIP$  identify refraction and reflection events on a locally limited sedimentary layer.

Data processing included amplitude recovery, frequency filtering using a classical band-pass Butterworth filter (3-10 Hz) and phase enhancement by a lateral phase coherency filter [Schimmel and Gallart, 2007]. The filter is data-adaptive and identifies signals by their coherence which is derived from the local phases of neighboring stations. The local phases are obtained from a time-frequency analysis of the seismic records. Coherence means a measure of trace-to-trace similarity of seismic waveforms within a small analysis window. A signal is assumed to be coherent while random noise is not. This latter procedure allows a better identification of weak seismic arrivals at large offsets, as can be observed in Figure 3.8. The coherency filter was especially valuable in the case of shot R1 allowing us to identify arrivals from 80 km to 140 km offsets. A total of 2297 picks were obtained, 1154 from the NS profile and 1143 from the EW.

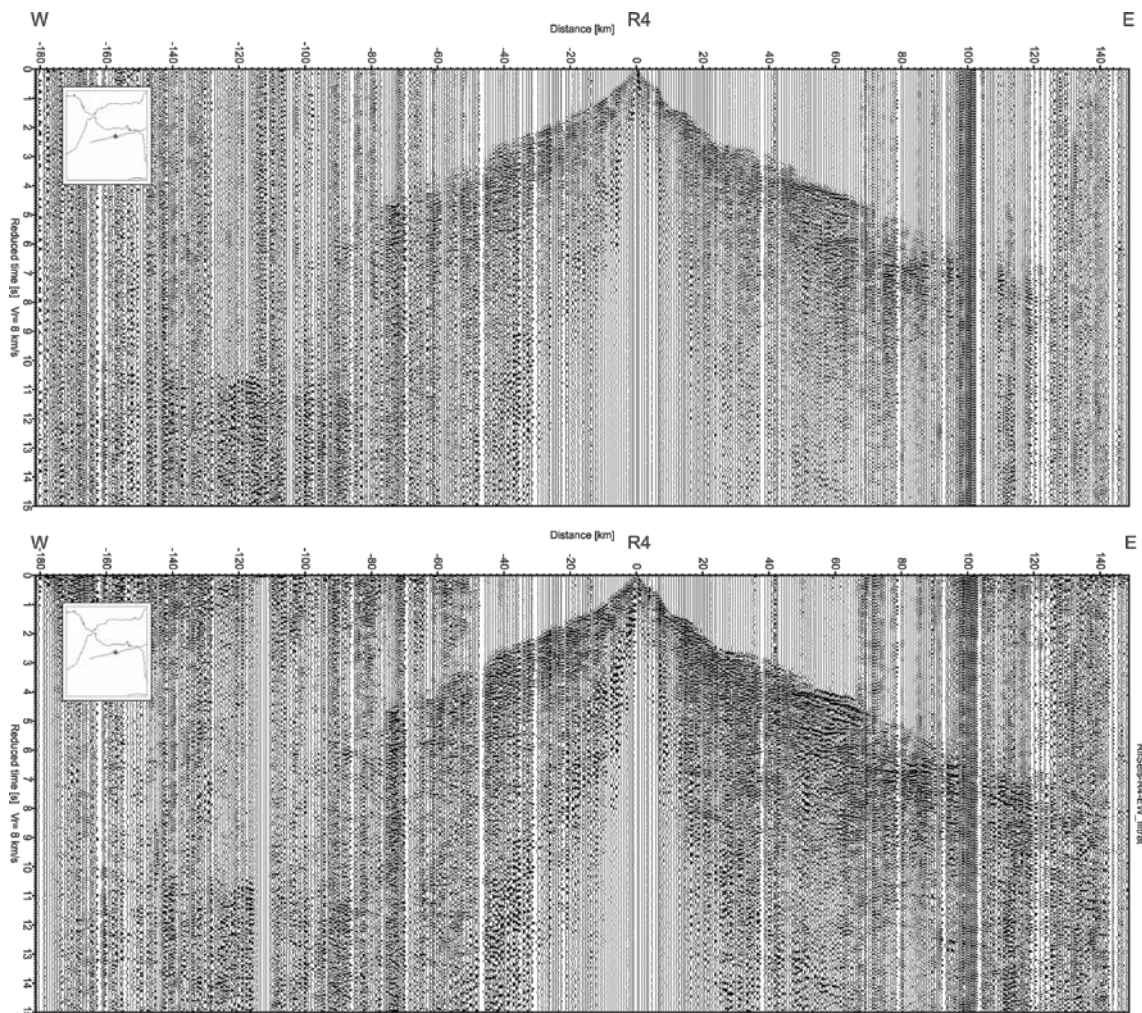


**Figure 3.8:** Record section for shot R4, where shows the (a) raw data, just using a frequency filtering (3-10 Hz); (b) the energy and phase enhancement by using a lateral phase coherency filter from Schimmel and Gallart (2007).

### 3.2.2 Wide-angle reflection /refraction seismic data interpretation

Several approaches have been tested to interpret the data, all of them based in ray theory; 1) travel-time and amplitude inversion method, 2) a first arrival seismic tomography, and 3) a low-fold seismic stack

#### a) Travel-time and amplitude inversion using RAYINVR

P-wave velocity-depth models were derived by forward modeling of diving and reflected waves using RAYINVR software (Zelt and Smith, 1992). The algorithm is based on asymptotic ray theory (Cerveny et al., 1977) and is widely used to interpret wide-angle profiles. In this approach, the theoretical travel-time response of an inhomogeneous medium is calculated and compared with the observed record sections. The model is modified and a new iteration is run to decrease the divergence between calculation and observation. Even if the software allows using a direct inversion scheme, the relative low density of the data and the complexity of the investigated area have made inefficient its practical use.

The input to the modeling program is a layered velocity-depth model. Each layer is delimited by nodes and a velocity for its top and its bottom is defined, allowing velocity gradients within the layer as well as lateral velocity variations. The medium is assumed to be isotropic with lateral homogeneity in a direction normal to the plane of the model. To calculate the theoretical ray tracing, the program divides each layer in trapezoidal blocks and calculates the velocity at any point within the trapezoid by linear interpolation between the upper and lower velocity in the trapezoid. To trace rays through the velocity model, the 2-D ray-tracing equations are solved numerically, satisfying the Snell's law at the boundaries between layers. Once the ray is traced through the model, the total travel-times are obtained by simple numerical integration along the ray path. Three ray families, refracted waves, reflected waves and head waves are taken into consideration (Figure 3.9).

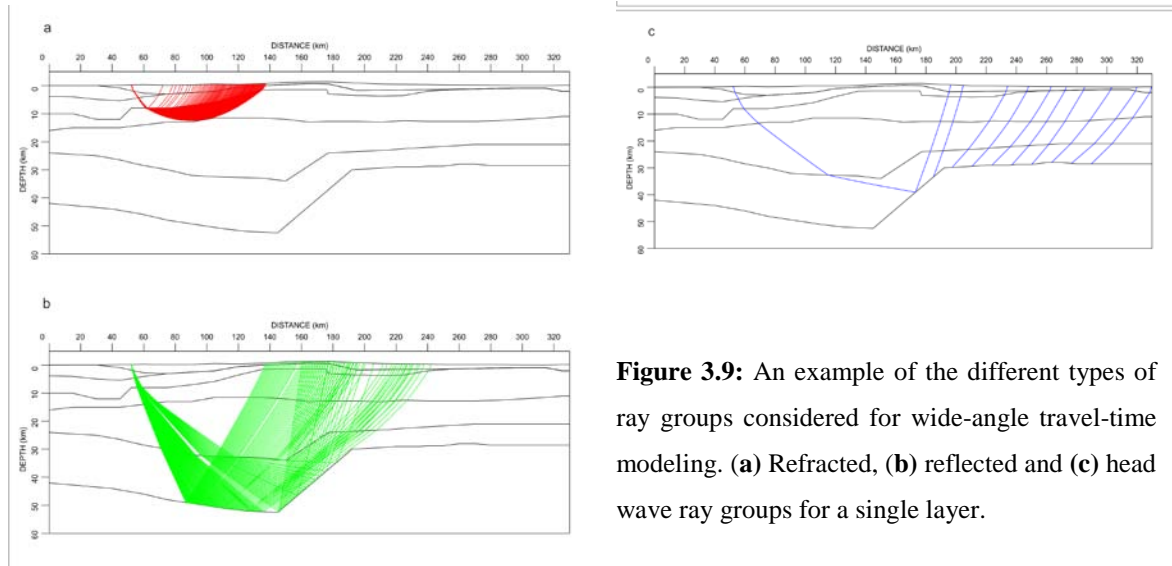


**Figure 3.9:** An example of the different types of ray groups considered for wide-angle travel-time modeling. (a) Refracted, (b) reflected and (c) head wave ray groups for a single layer.

The models are obtained starting from the uppermost layer, adjusting the travel-times for all the shots and then moving down to deeper levels. RAYINVR is the main program of the software package which provides ray tracing in 2-D isotropic media for forward and inverse modeling, and calculates travel-times residuals and partial derivatives for inversion. It also allows obtaining synthetic traces which provide information on amplitudes, even it is well-known that its accuracy is limited.

Additional geological and geophysical constraints were considered in the modeling procedure where available. For the NS profile we start from the velocity-depth model presented by Ayarza et al. (2014) from the interpretation of the SIMA profile, crossing the Atlas and partially overlapping our profile. At the northern edge, the seismic models by Medialdea et al. (1986) were also taken into consideration. Different geological results compiled in Chalouan et al. (2008) have been used to get an initial estimation of the geometry and velocities in the uppermost sedimentary layers.

### b) First Arrival Seismic Tomography

The first-arrival seismic tomography method (FAST, Zelt and Barton, 1998) is a tomographic method especially adapted to deal with data from controlled-source experiments. FAST uses the first seismic arrivals identified at each trace to infer a minimum-structure model by minimizing the roughness and size of the total slowness perturbation with respect to the starting model. A simplified starting model and a uniform parameterization of the investigated area are needed to start the process. As in

most tomographic methods, regularizations parameters are also needed in order to stabilize the inversion. The final result is a model which does not include seismic discontinuities, but smooth vertical and horizontal seismic velocity gradients. This model represents the minimum structure needed to justify the observed data. In order to produce satisfactory results, a dense distribution of rays sampling the investigated area is needed. This is typically achieved in offshore surveys, where air-guns are shot every 150 or 300 m and recorded by OBS separated few kilometers each order.

The FAST method has been implemented and tested using data from the RIFSIIS experiment to verify if additional information could be inferred from the uppermost sedimentary layers. In our experiment, stations were distributed approximately every 750 m and only 2-3 sources were shot for each profile. This resulted in a low density of first arrivals (Figure 3.10) which probably does not allow getting significant results using the FAST code.

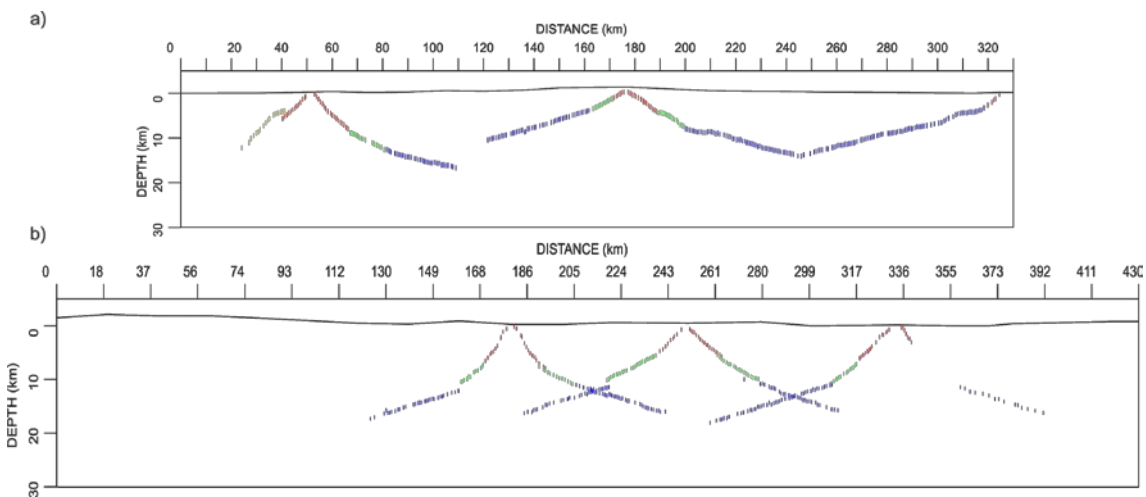


**Figure 3.10:** Schematic models of the wide-angle data showing the density of first arrivals. In red and green are represented the  $P_s$  phases, and in blue the first arrivals along the basement ( $P_g$ ). More information is described in chapter 5 **(a)** EW profile and **(b)** NS profile.

However, we tested if the method may provide some improvement to the available model. To do so, we used the final model resulting from the RAYINVR approach as starting model of the FAST code (Figure 3.11). Even if some changes appear in the sedimentary layers, its consistency could not be demonstrated.

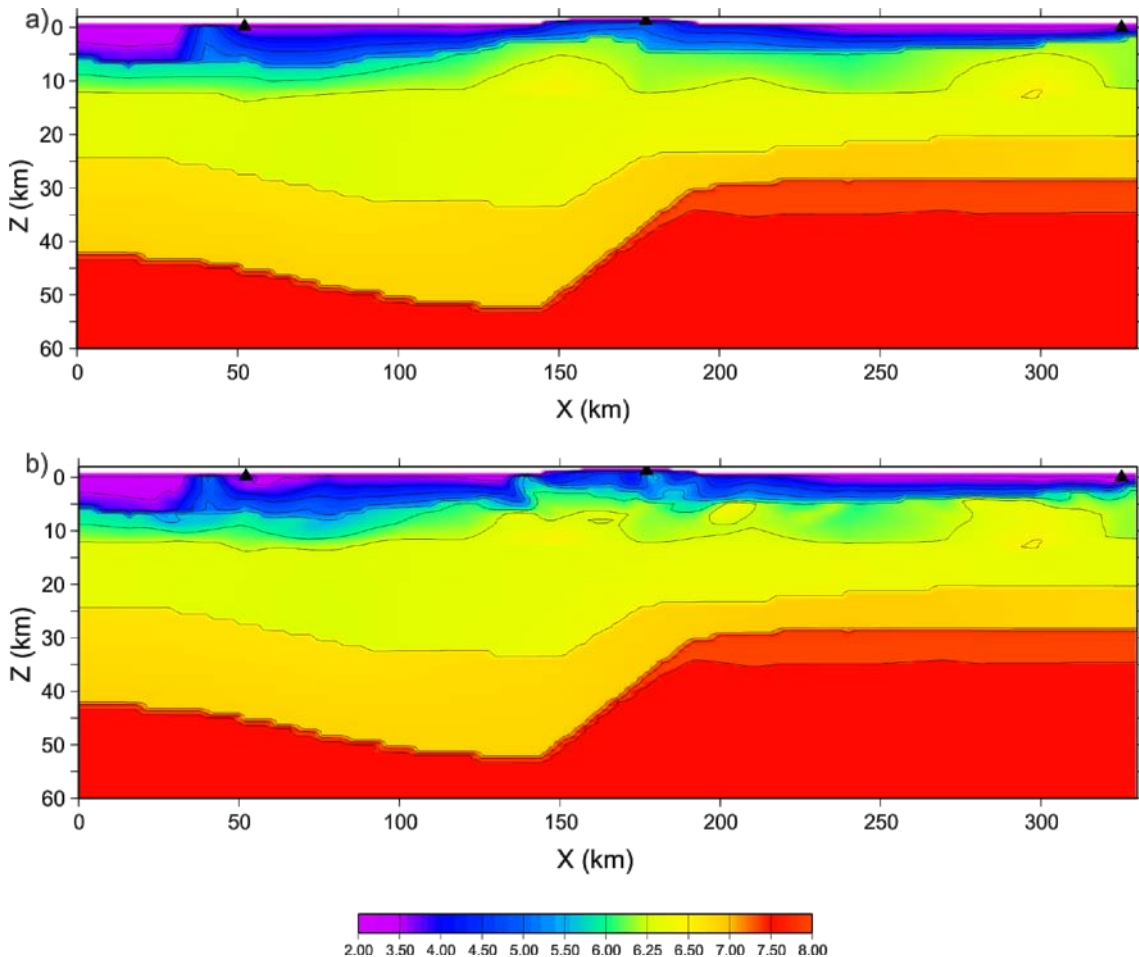


**Figure 3.11:** (a) Input model used in FAST program, which corresponds to the final model obtained by RAYINVR program; (b) Best solution obtained by using FAST program. There are not many differences between both final models due to the distance between shots, which does not provide a good coverage, and therefore the output model is similar to the input model.

### c) 3D low fold wide-angle seismic stack

The deployment logistics during the RIFSIS project allowed that all the stations recorded not only the shots aligned with each profile, but also the rest of them, hence providing a large set of offline propagation times. This data set can be used to investigate the geometry of the Moho in the zones not sampled by the main RIFSIS profiles.

Seismic vertical reflection profiles take advantage of experimental devices with geometries of multiple coverages, which allow to group traces from different shots with a common reflection point (CDP). This allows eliminating incoherent signals and enhances the amplitude of the coherent phases. In our case the shot records have large offsets (long distance between the shot and the receiver) and hence we do not have

significant multiple coverage. However, the data can be processed in an analogue way to obtain a wide-angle, low-fold seismic stack. The offline shot-gathers of the RIFSIS project are processed following a conventional scheme. Several steps have been applied to increase the signal-to-noise ratio, including band pass frequency filtering, spherical divergence amplitude corrections, spectral whitening (spectral balancing), and amplitude gain (trace balancing). Following Carbonell et al. (2002), a hyperbolic time reduction, comparable to the classical Normal Move Out (NMO) correction, is applied to the data, resulting in stacks in which the reflections from the Moho are expected to appear as subhorizontal lines. By stacking signals of offline shots (e.g. shot R1 along EW profile) we can get information on the midpoint area, thus providing additional constraints on an area otherwise unsampled (Figure 3.12). Hence, low-fold wide-angle seismic stack provides a tool to image the possible lateral variations of the Moho topography.

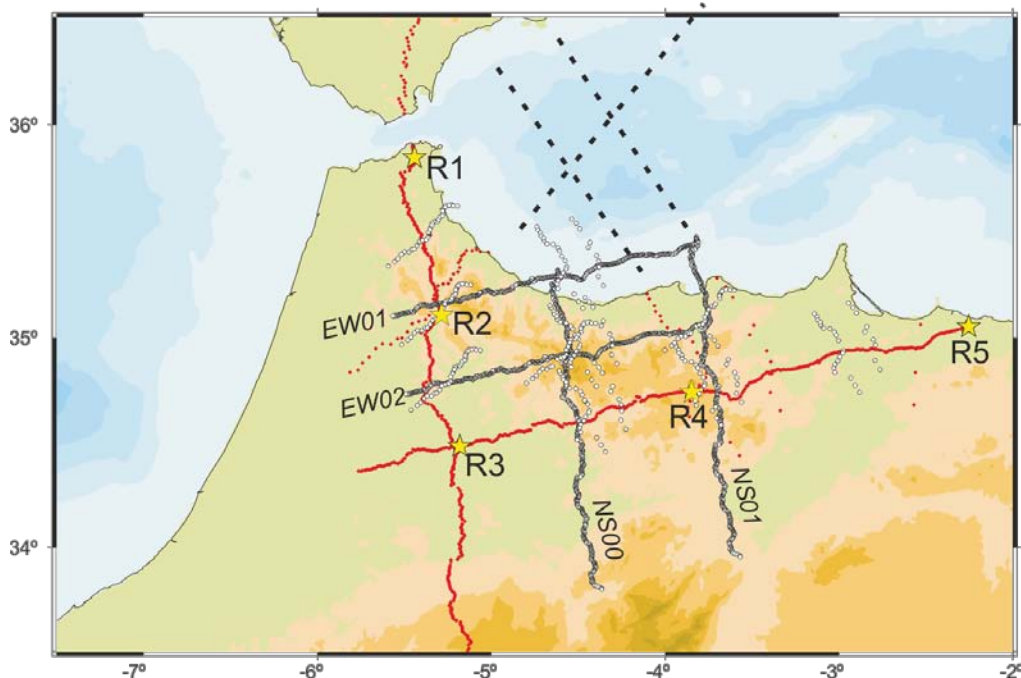


**Figure 3.12:** Geometry of the wide-angle seismic reflection experiments. Shot point locations are indicated by yellow stars: The red dots indicate the location of the seismic recorders while the white dots indicate the CMP (Common mid points) used for the low-fold wide-angle stacks. Black lines show the contributing GASSIS-WestMed offshore profiles.

A second, complementary approach arises from the identification and reading of the *PmP* phases arrivals in the offline record sections of the RIFSI shots. Figure 3.13 illustrates the approach followed here. The time arrivals interpreted to correspond to *PmP* phases are read from the fan record sections from the WestMed profiles. Assuming a uniform crust with a mean velocity value of 6.3 km/s, the depth of the reflection point is calculated. This value is then assigned to the midpoint between the shot and the receiver positions. Of course, those assumptions imply that large errors can arise in case of heterogeneities, but we will show that such approach can also provide significant results in this region.

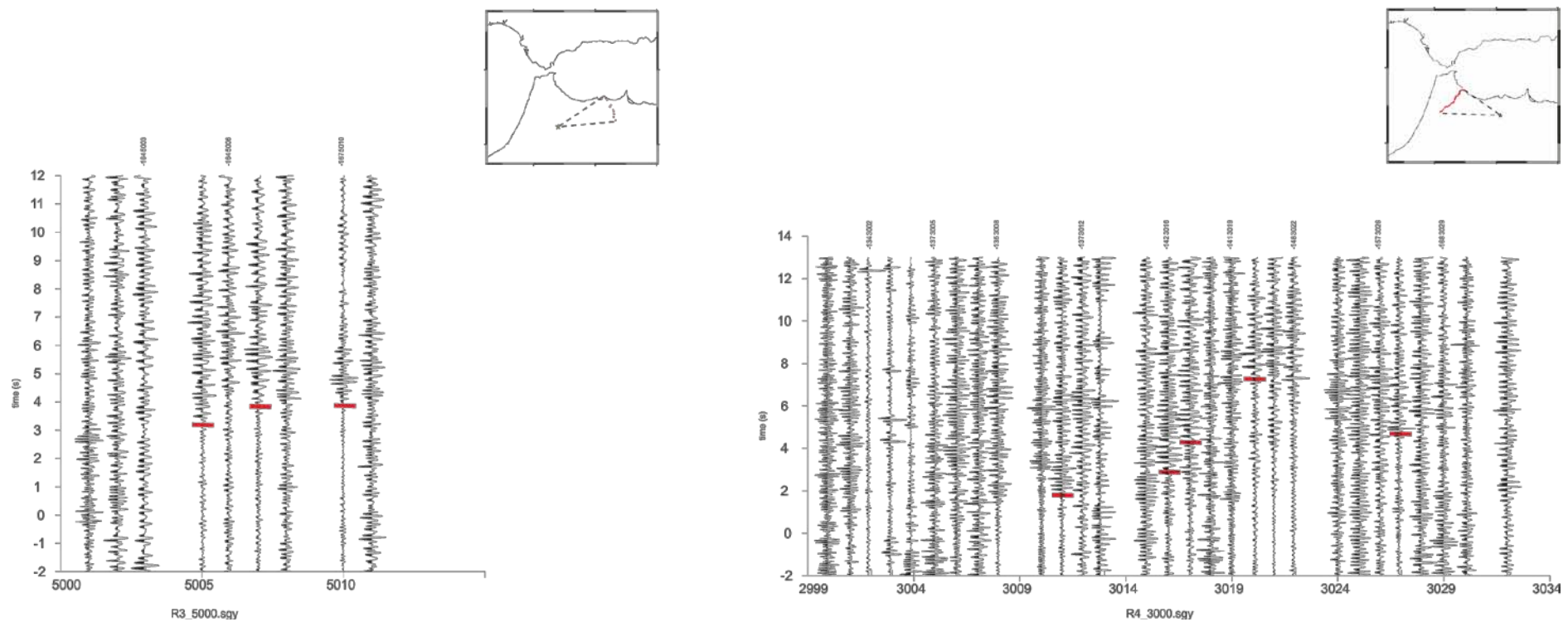


**Figure 3.13:** Examples of  $PmP$  picking on the complementary profile. **Left panel:** Shot R3 recorded at line 5000, where the offsets are between 164 and 167 km. **Right panel:** Shot R4 recorded at line 3000, where the offsets are between 120 and 170 km. Times are reduced using  $v=6.0$  km/s.

### 3.2.2. Gravity validation

To further assess its robustness, the new seismic models derived from our wide-angle data are converted to density and the predicted Bouguer anomaly is compared with the measured one from BGI database. Using this tool helps us to validate the velocity-depths models obtained, and it can bring information of the areas that the seismic experiment could not cover, such as physical properties of shallow layers at far offsets.

To account for lateral variations perpendicular to the strike of the profiles, gravity data have been averaged over a  $\pm 25$  km strip of the RIFISIS seismic profiles. The gravity models have been built using the geometry derived from seismic modeling. An averaged P-wave velocity value has been assumed for each layer in the seismic model and the corresponding densities were calculated using the empirical relations by Brocher (2005), (Figure 3.14) which applies to most lithologies, except mafic- and calcium-rich rocks. The crust is modeled as: sedimentary layers with densities that range from 1800 to 2400 kg/m<sup>3</sup>, an underlying crystalline basement with density of 2650 kg/m<sup>3</sup>, 2700 kg/m<sup>3</sup> for the upper crust, 2800 to 2850 kg/m<sup>3</sup> for the middle crust, 2850 to 2950 kg/m<sup>3</sup> for the lower crust and 3300 kg/m<sup>3</sup> for the uppermost lithospheric mantle. Calculations of the gravity model response are based on the methods of Talwani et al. (1959), and Talwani and Heirtzler (1964), and the algorithms described in Won and Bevis (1987) and implemented in the Geosoft Oasis Montaj 2-D forward modeling software package (IUGG, 2012).

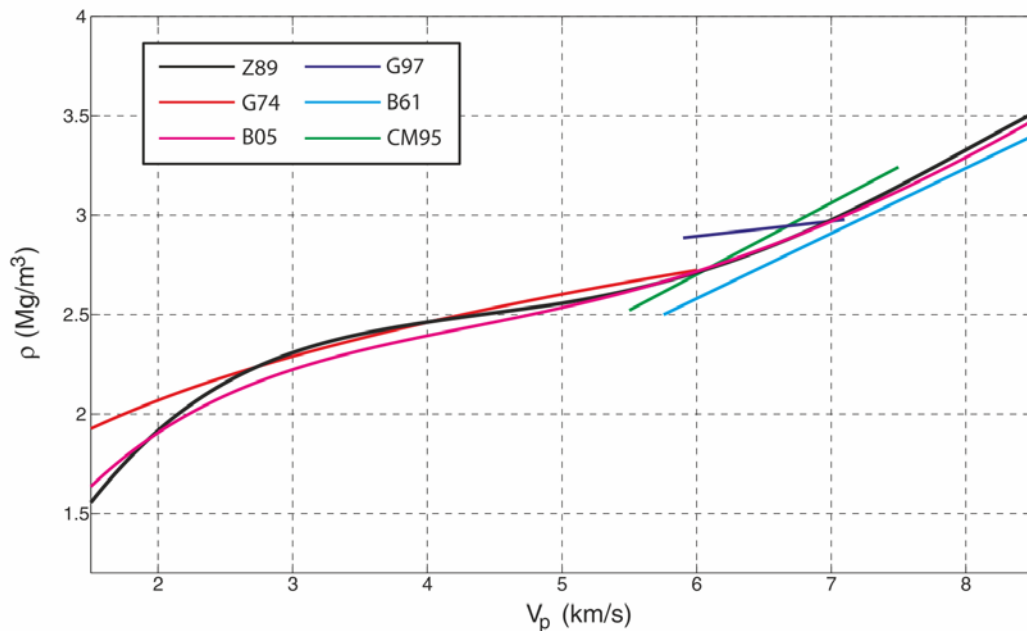


**Figure: 3.14:** Representation of the commonly used  $V_p$ - $\rho$  relations. References: ZS89, Zelt (1989); G74, Gardner et al. (1974); B05, Brocher (2005); G97, Godfrey et al. (1997); B61, Birch (1961); CM, Christensen and Mooney (1995) - (Modified from Bezada and Zelt (2011))

### 3.3 Receiver Functions

The geometry of the Moho interface can also been investigated by using passive seismic data, that is, recording distant earthquakes in permanent and portable broadband seismic stations deployed over north Morocco. We have considered the classical receiver function (RF) technique. Receiver functions are time series computed from the three components records of teleseismic events by deconvolution of the vertical component from the radial and transversal ones. As teleseismic signals reach the station with small incidence angles, the vertical component is assumed to be a proxy of the source time function and the source-side and deep-earth propagation effects. Once deconvolved from the horizontal components, the remaining signal shows the response of Earth structure beneath the station. The most prominent signal in the RF is the P-to-S conversion (Ps) in the main seismic discontinuity beneath the station, which usually corresponds to the Moho. Inspection of the time-arrival of this phase and its reverberations allow inferring the depth of this converter (Figure 3.15).

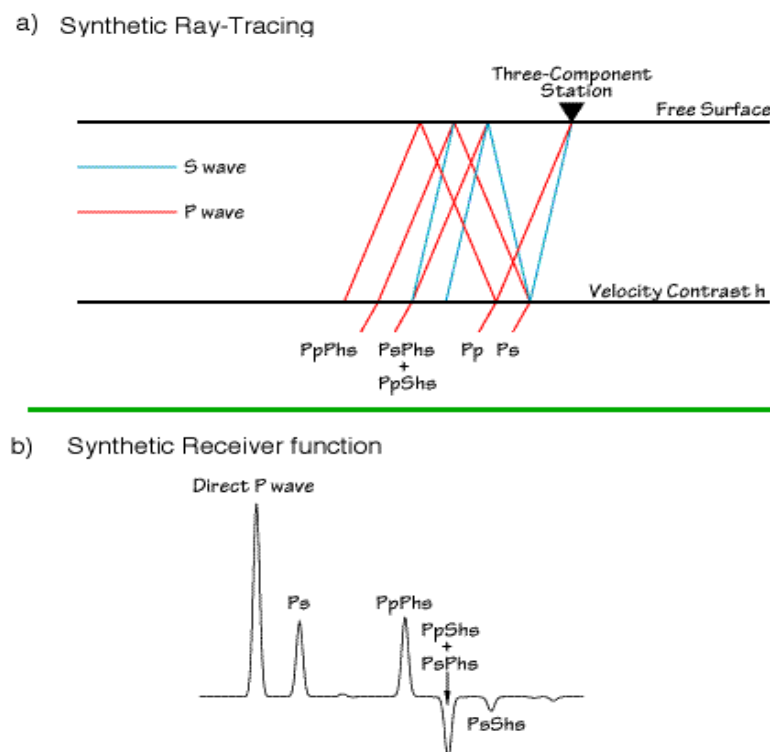


**Figure 3.15:** A schematic representation of receiver function: (a) Diagram showing the major Ps converted phases for a layer  $h$  over a half space model. (b) Synthetic RF corresponding to the model in (a) showing the direct P and the Ps converted phase and its multiples

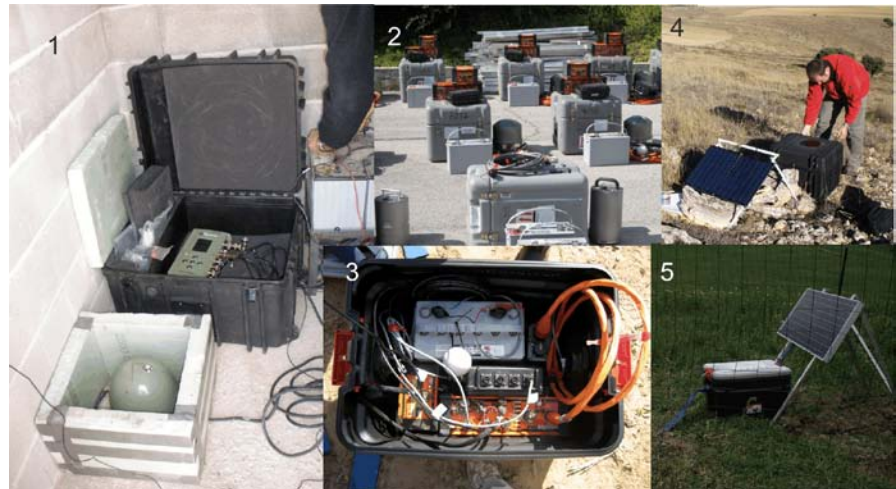
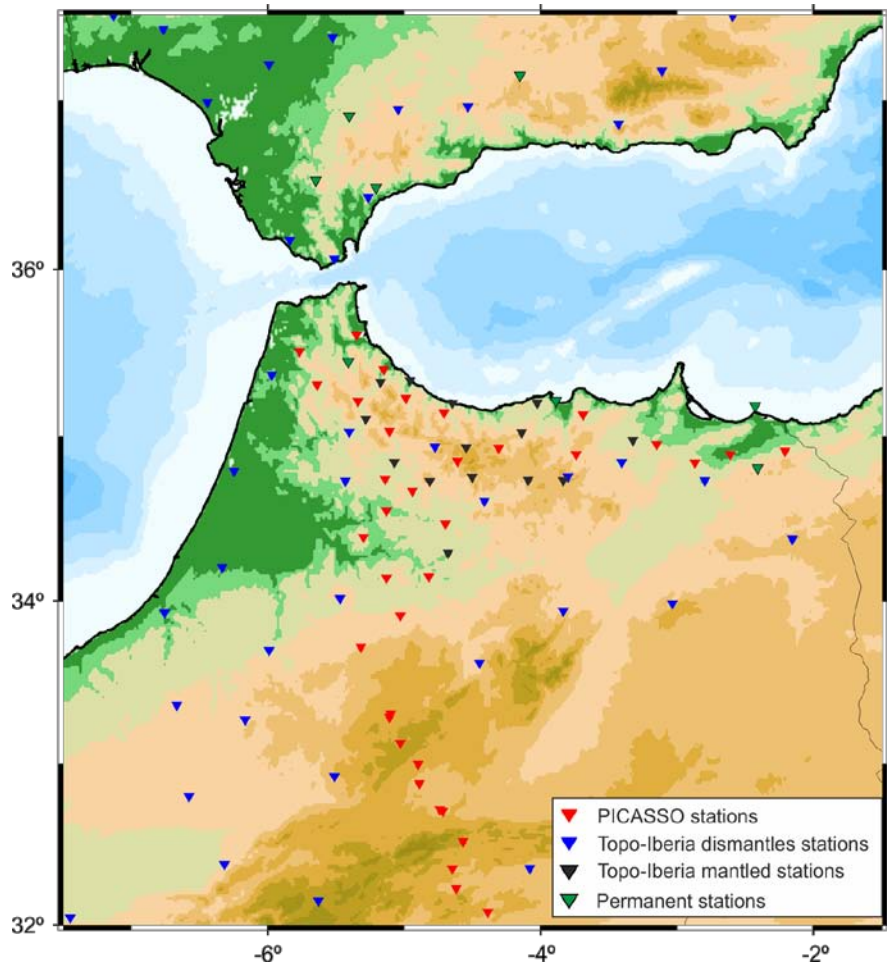


**Figure 3.16:** (Right) Map showing the locations of the Topo-Iberia (blue and black; [iberarray.ictja.csic.es](http://iberarray.ictja.csic.es)) and PICASSO (red; [iris.edu](http://iris.edu)) seismic network stations used to perform the Receiver Function study. (Left) Instrumentation used and installed in the field. (1) Trillium 120 sensor connected to Nanometrics datalogger; (2) STS-2 and GURALP sensors with their Q330 dataloggers for the Picasso project; (3) Initial setting of electronics – Action Packer, containing the battery, Q330+Baler, power box, GPS, cables and break out box for a STS-2 sensor; (4) Topo-Iberia station with the solar panel; (5) PICASSO station with solar panel and a fencing to protect the station.

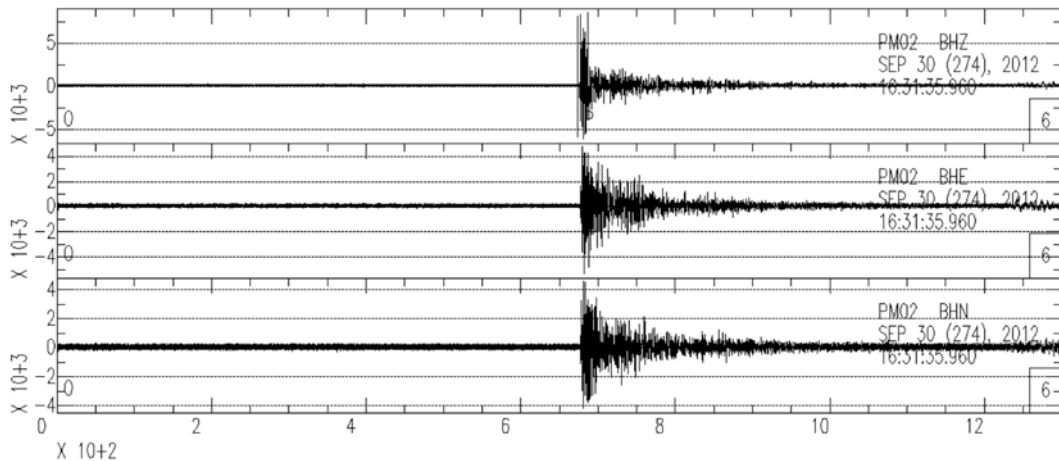


**Figure 3.17:** Three-component seismogram, 0.5-12 Hz bandpass filtered, recorded at the M002 station. In the vertical (HHZ) component is showed the first arrival, with the P label, of the teleseismic event.

The first step in the RF processing is the selection of the teleseismic events with magnitude higher than 5.5, epicentral distances between 30° and 90° and clear P arrivals recorded from the Topo-Iberia and/or PICASSO networks (Figures 5.16 and 5.17). The RFs are calculated by frequency domain deconvolution (Langton, 1979) of the vertical component from the horizontal components in the time window corresponding to the P arrival and its coda. The deconvolution is done using the classical “pwaveqn” software (Ammon, 1997), using gauss filter-width parameter values of 2-4 and typical water level values ranging between .01 and .001. After visual inspection, only those RF with good signal-to-noise ratio were retained.

Once the RF calculated, we have used the H- $\kappa$  analysis (Zhu and Kanamori, 2000) to infer an estimation of the crustal depth (H) and the  $\kappa$  ratio ( $\kappa = Vp/Vs$ ) beneath each investigated station. This method considers a mean crustal velocity and estimates the arrival time of the Ps, PpPs and PsPs phases for each given combination of H and  $\kappa$ . The real amplitude values of the RFs at those times are then evaluated in the (H,  $\kappa$ ) parameter space using the estimation parameter s:

$$s\left(H, \frac{Vp}{Vs}\right) = \sum_n [a(tp - Ps) + a(tp - PpPs) + a(tp - PsPs)]$$

The presence of a well-defined maximum in the stacking surface defines the preferred solution for each station. In many cases, and especially if the energy of the multiple phases is scarce, the trade-off between both parameters produces stacking surfaces showing a well-defined “crest” but with poorly constrained maximum value (Figure 3.18a). We have used a mean crustal  $V_p$  of 6.2 km/s, estimated from the wide-angle seismic profiles available in the region (Gil et al., 2014; and Chapter 5). It has been shown that variations of  $\pm 0.1$  km/s in  $V_p$  result in changes of  $\pm 0.6$  km in the Moho depth, making the choice of the reference  $V_p$  value not a critical issue (Mohsen et al., 2005; Nair et al., 2006).

The H- $\kappa$  method is known to have limitations in the presence of a dipping converser, a gradient-type boundary or in presence of sedimentary environments. (e.g. Julia et al., 2003; Lombardi et al., 2008). In those cases the Ps reverberations are masked and hence the amplitude summation does not provide reliable results. In this case, following Mancilla et al. (2012), we have estimated the crustal thickness by picking the arrival time of the converted phase, Ps, in the summation trace after applying a Ps-moveout correction and then converting delay time to depth using a  $V_p/V_s$  ratio consistent with that derived for other stations in the same domain (Figure 3.18b).

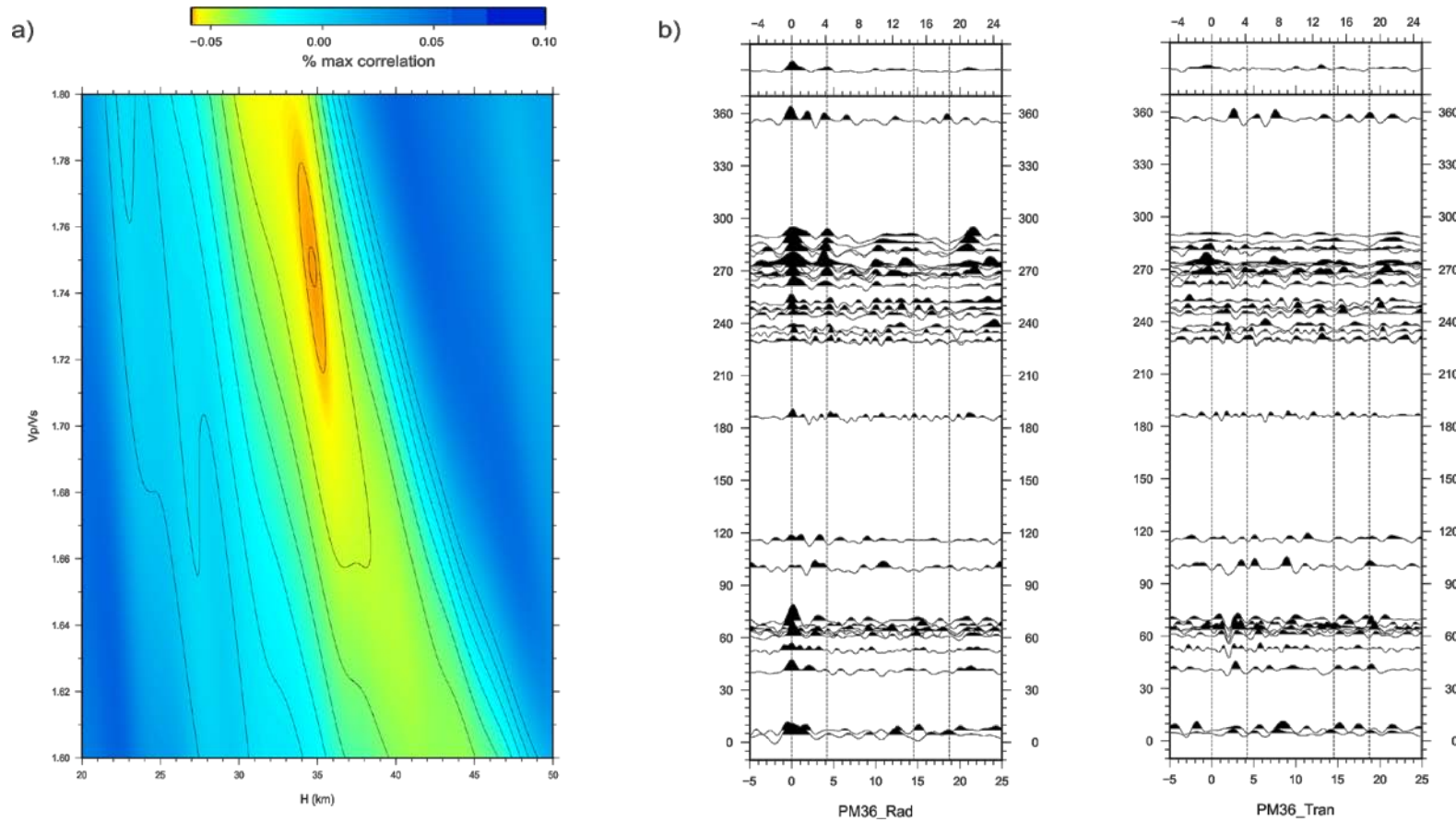


**Figure 3.18:** Results for station PM36. (a) H- $\kappa$  analysis. The thick black ellipse denotes the estimated uncertainty in the definition of the Moroccan Moho. (b) Receiver functions retrieved from the radial and transverse components, respectively, corrected for Ps-moveout and stacked into bins of  $10^\circ$  of back azimuth. The dashed lines correspond to the direct P arrival, the converted phase (Ps) and the multiples (PsPs+PpSs). On top of each panel it is shown the radial and transverse stacked Receiver Functions.

## **Part II:**

# **RESULTS AND DISCUSSIONS**



# Chapter 4: Uppermost mantle velocity and anisotropy in the Euro-Mediterranean region from Pn and Sn tomography

## 4.1 Introduction

The original purpose of this study was to produce a tomographic image of the uppermost mantle beneath the Iberian Peninsula and Northern Morocco, using the classical Hearn's method (Hearn, 1996), based on the analysis of *Pn* phases. However, we decided to extend the study area to cover the whole Euro-Mediterranean region with the aim of providing a view of the properties of the uppermost mantle beneath the whole region, affected by recent tectonic events including subduction and extensional processes. This large scale approach allows integrating previous works focusing at smaller scales (Mele et al., 1998; Hearn et al., 1999; Serrano et al., 2005) and to connect them with recently published *Pn* tomographies beneath East Asia (Al-Lazki et al., 2004; Mutlu et al., 2011) and the continental collision zone from Alps to Himalaya (Pei et al., 2011a). The lack of available seismic stations make impossible to extend the tomographic images southwards of the Mediterranean coast of Africa. However, the Mediterranean basin is generally well sampled, as it will be discussed hereafter.

The geodynamics of the Euro-Mediterranean region has been a subject of debate during the last decade. Key questions, as the Cenozoic evolution of the western Mediterranean, the geometry of the subduction beneath the Peloponnesus or the relationship between the European and the Adrian plates beneath the western Alps are still not solved. One of the main tools to investigate those points is provided by body and surface wave tomographies. However, those methods do not allow constraining in the geodynamic interpretation. In this chapter we present a new regional scale *Pn* and *Sn* tomographic inversion aims to provide new clues to the discussion of those open subjects.

## 4.2 Data analysis

As previously mentioned in Chapter 3, to select the useful dataset we followed a classical approach of: (1) hypocentral depths less than 35 km; this avoids considering

subcrustal earthquakes which will not generate *Pn* phases. We have chosen a realistic reference value, even if changes in crustal depths beneath the Mediterranean region are very important; (2) epicentral distances ranging from 220 to 1440 km ( $2.0^\circ$  to  $12.60^\circ$ ); those values were determined from the inspection of the time-distance plot of all available wave picks; (3) initial residuals smaller than 6 s; (4) residuals smaller than 3 s after the adjustment of the mean *Pn* velocity; (5) each retained event must be recorded at a minimum of five stations and each retained station must have arrivals from five or more events. These selection criteria have also been considered for the *Sn* phases, assuming a typical *Vp/Vs* ratio of 1.73.

Applying those constraints, from an initial set of 172293 travel-times, a total of 579753 *Pn* arrivals corresponding to 12377 events recorded at 1408 stations were retained for *Pn* waves (Figure 4.1a), and 162645 arrivals from 7528 earthquakes at 869 stations for *Sn* waves. The resulting ray paths provide an appropriate coverage for the *Pn* phases, although less satisfactory for the *Sn* ones (Figure 4.1b).

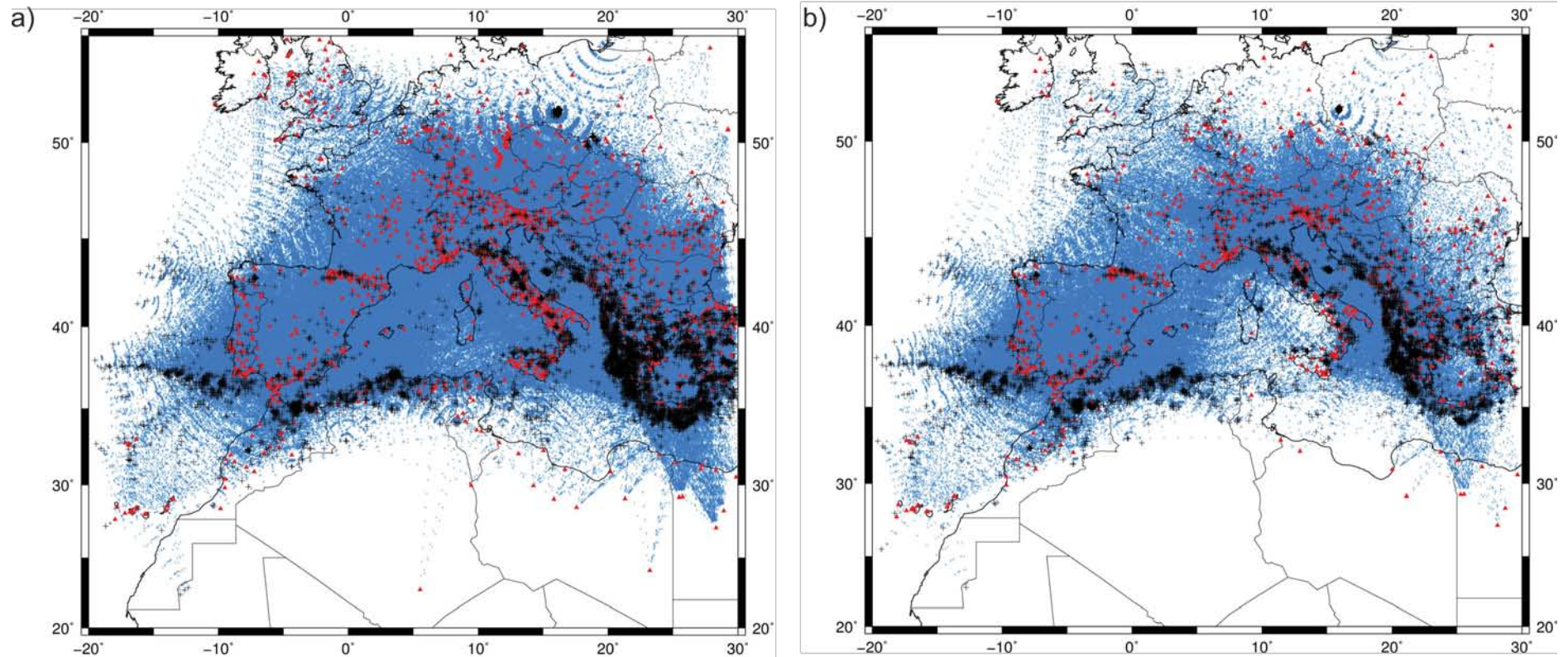


**Figure 4.1:** *Pn* (a) and *Sn* (b) ray paths used in the tomographic inversion. Red triangles and crosses display respectively the stations and events used in each tomographic inversion.

We followed the classical method of Hearn (1996) for inverting *Pn* and *Sn* traveltimes both for isotropic velocity variations and transverse anisotropic perturbations. Previously we have performed a series of tests to investigate the resolution that can be obtained with our event-station data set, and to fix the values of the number of iterations and the damping factors more convenient for our data set. First trials were performed in the isotropic case with a number of iterations limited to 25. Different damping values from 200 to 1000 were tested and finally a value of 500 was retained for slowness, even if no significant changes appear for damping larger than 400. When dealing with *Sn* arrivals a smaller damping factor of 200 must be used to get a smooth image. In the anisotropic case, the trade-off between velocity and anisotropy variations has been checked using different combinations of slowness and anisotropy damping factors. However, neither the standard errors nor the tomographic images obtained show significant differences, if extreme combinations were avoided. We finally used the same values for both damping factors, as it has been recommended by Hearn (1996). This choice implies that the amount of velocity and anisotropy perturbation is similar. We decided to extend our calculations to 100 iterations, even if little additional effect on the standard error or the velocity image is observed after 60 iterations. The final root mean square of the residuals is 0.83946 s. Allowing more iterations resulted in more constrained and patched velocity anomalies, that in turn make more convenient to use a higher damping factor, finally fixed to 1000 for the *Pn* inversion and to 600 for the *Sn* case.

Checkerboard test models with different pattern sizes and alternating values of  $\pm 0.25$  km/s for low and high velocities were used to explore the resolution, with station and event delays set to zero. We calculated synthetic traveltimes using the same configuration of events and stations as in the real case and the same damping factors to test whether the input model can be recovered properly. The checkerboard with a  $2^\circ \times 2^\circ$  pattern can be satisfactorily recovered for velocity variations in most of the investigated area (Figure 4.2). However, the scarce amount of seismic stations in Northern Africa results in a lack of resolution in the southern Mediterranean coasts. Most of southwestern Europe and the northernmost Morocco are well resolved even, if beneath Northern Iberia and the Gulf of Cadiz the resolution diminishes as most of the rays are orientated along single directions, resulting in elongated leaking. A checkerboard with  $1^\circ \times 1^\circ$  cells can only be recovered properly in the zone more illuminated by seismic

rays, comprising Central Iberia, Western Mediterranean Basin, SW of France, Italy, the Balkan and Greece.

Regarding the anisotropic pattern, the resolution is clearly lower (Figure 4.3). In this case the synthetic model has anisotropic fast polarization directions (FPDs) orientated orthogonally in neighbor cells, with a 3 per cent degree of anisotropy. Checkerboard test show how the inversion produces spurious oblique orientations at the corners of the cells, resulting in an image dominated by those artifacts when checkerboard cells of  $2^\circ \times 2^\circ$  are used. Only when large cells of  $4^\circ \times 4^\circ$  are used, the anisotropic pattern can be properly retrieved in most of the study area. This clearly shows that the anisotropic parameters are not properly constrained at small scales and thus their interpretation must be taken with special care, focusing only in large-scale terms.

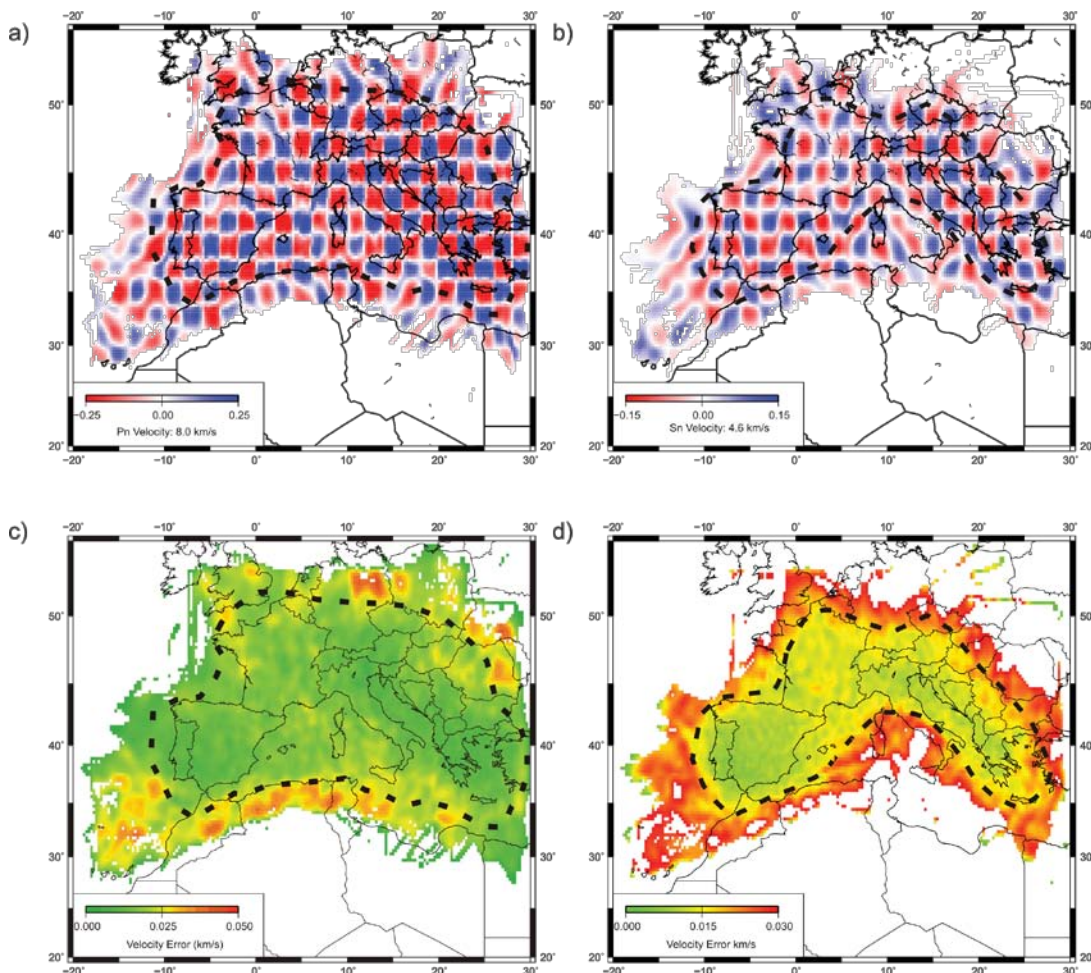


**Figure 4.2:** Checkerboard test for  $Pn$  and  $Sn$  velocity variations ( $2^\circ \times 2^\circ$ ), (a) and (b) respectively. Standard deviations of the  $Pn$  and  $Sn$  velocities from bootstrap analysis, (c) and (d) respectively. The dashed line delimits the confidence zone (small standard deviations of  $Pn$  and  $Sn$  velocity and successful checkerboard tests)

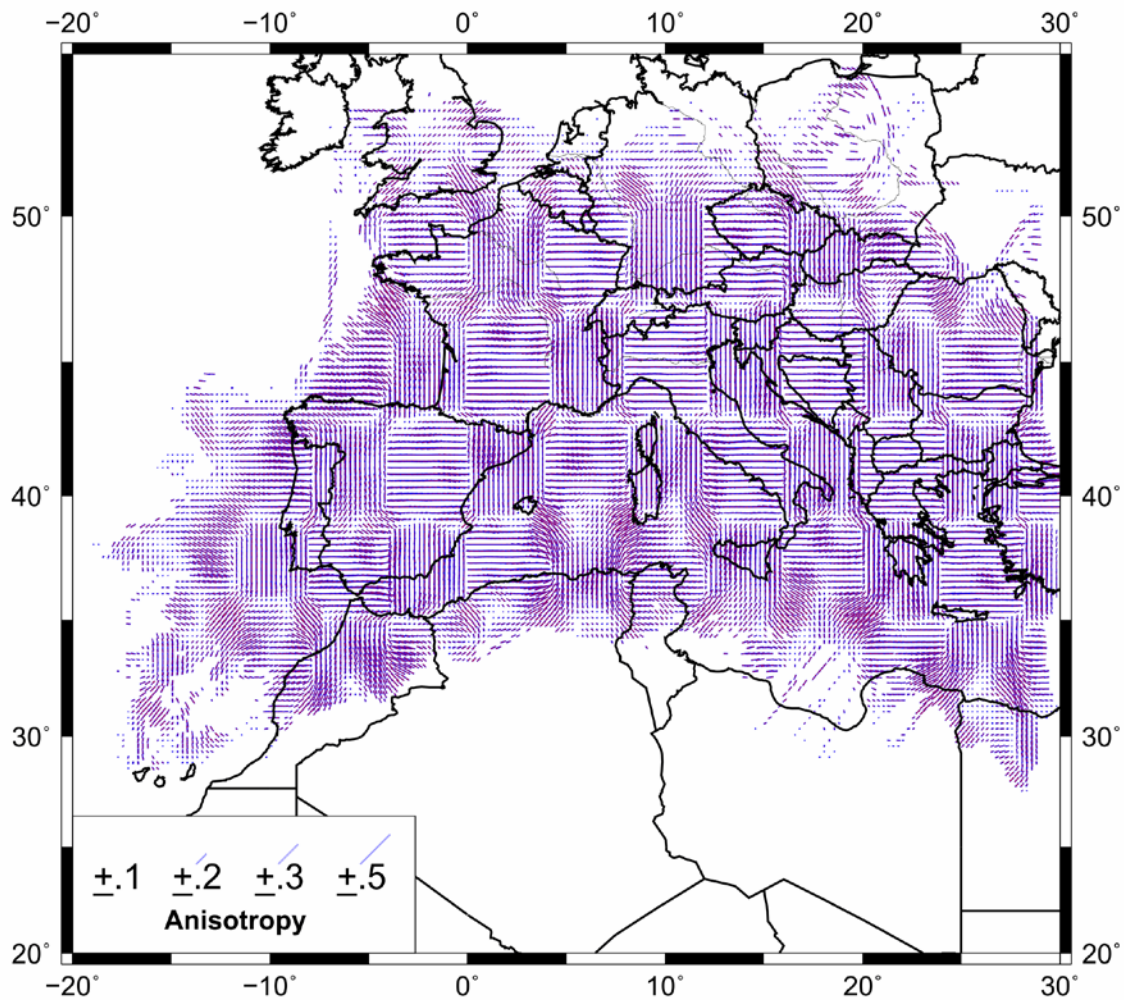


**Figure 4.3:** Checkerboard test for anisotropic parameters in the *Pn* tomographic inversion ( $4^{\circ} \times 4^{\circ}$ ).

The bootstrap analysis technique (Hearn and Ni, 1994) is used to estimate the errors in the *Pn* velocity distribution. The method works by constructing a number of data sets randomly picked from the original data, inverting each one with the same parameters and finally estimating the standard error of the *Pn* velocity distribution. Figures (4.2a and 4.2c) show the result of the procedure. The velocity errors are small, only exceeding 0.02 km/s in the most external zones, thus confirming the good coverage in the central region.

Checkerboard tests and bootstrap analysis have also been applied to the *Sn* set (Figures 4.2b, d). In this case, the area recovered properly is smaller, due to the more limited number of travel-time readings. The main difference with *Pn* data is located beneath the Tyrrhenian Sea, an area not sampled properly by *Sn* phases. However, a

large zone including the whole Iberian Peninsula, France, northern Italy, the Adrian Plate, Central Europe, the Balkans and Greece is well resolved by both data sets.

### 4.3 Results

The fitting of all the retained travel-times led to a *Pn* velocity estimation of 8.03 km/s. Assuming a 6.2 km/s mean value for the crustal velocity (value which is in agreement with Christensen and Mooney, 1995, and with the average crustal velocity in the Rif, see more information in the following chapter), the obtained intercept time results in a mean crustal thickness over the whole area of 39.1 km.

The station static delay terms reflect variations in the crustal thickness and/or velocity relative to the assumed model. The presence of marked variations in crustal depth beneath the investigated area has been revealed from a large number of active seismic surveys (see Grad et al., 2009; Tesauro et al., 2008; Díaz and Gallart, 2009, and references therein). The station delays obtained in our study (Figure 4.4) are in general in good agreement with those results. Positive delays that can be related to zones with increased crustal thickness are observed along the Hellenides, Alps, Apennines, Pyrenees, Betics and Rif ranges. The largest consistent negative delays are observed from the Canary Islands to Sicily along the southern Mediterranean coasts.

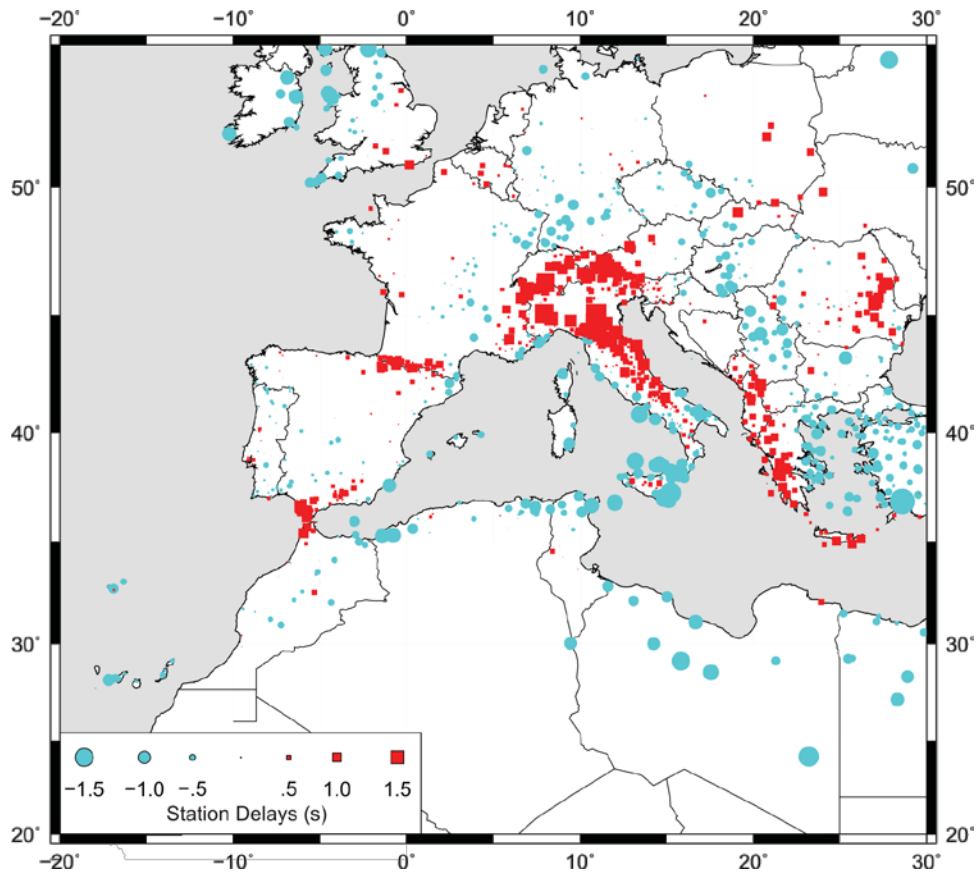


**Figure 4.4:** Static time delays associated to each station

The *Pn* velocity perturbations are calculated first for the isotropic case (Figure 4.5a), and then an anisotropic term is introduced (Figure 4.5b). At a first glance, the presence of heterogeneous lithospheric structures in the Mediterranean area is clearly inferred from the observation of very large fast and slow anomalies beneath the region, generally in close correlation with surface geology. The inclusion of an anisotropic term does not improve significantly the final rms, evidencing the intrinsic trade-off between velocity and anisotropic variations. However, the anisotropic term enhances significantly the lateral continuity of the anomalies, resulting in more constrained images. This effect, already reported by Hearn (1996), suggests that the presence of anisotropy must be included in any seismic study to be carried over those regions.

The most significant low-velocity values (<7.8 km/s) are found beneath the main orogenic chains (Alps, Pyrenees, Betics, Apennines and the Calabrian Arc) and under the Sardinia and the East and South of the Balearic Islands, close to the northern limit of the Algerian Basin. The Dinarides-Hellenic arc is also imaged from its northern limit to the south of Peloponnesus Peninsula. Beneath Crete, the velocity anomaly is hardly

recognized, probably due to reduced ray coverage. The signature of the Alps is not continuous, with low-velocity zones beneath its W and SW terminations, separated by an 8.0 km/s zone along the Swiss-Italian border. The anomaly beneath the Pyrenees is limited to its eastern section, while no perturbation is apparent neither in the western Pyrenean Chain nor beneath the westward prolongation of the orogen, the Cantabrian Mountains. However, the latter is not well sampled from our data. A large velocity anomaly is observed beneath the Eastern termination of the Betic chain, while the southern part of the Gibraltar Arc (Rif chain), still inside the well-resolved zone, shows a velocity close to 8.0 km/s.

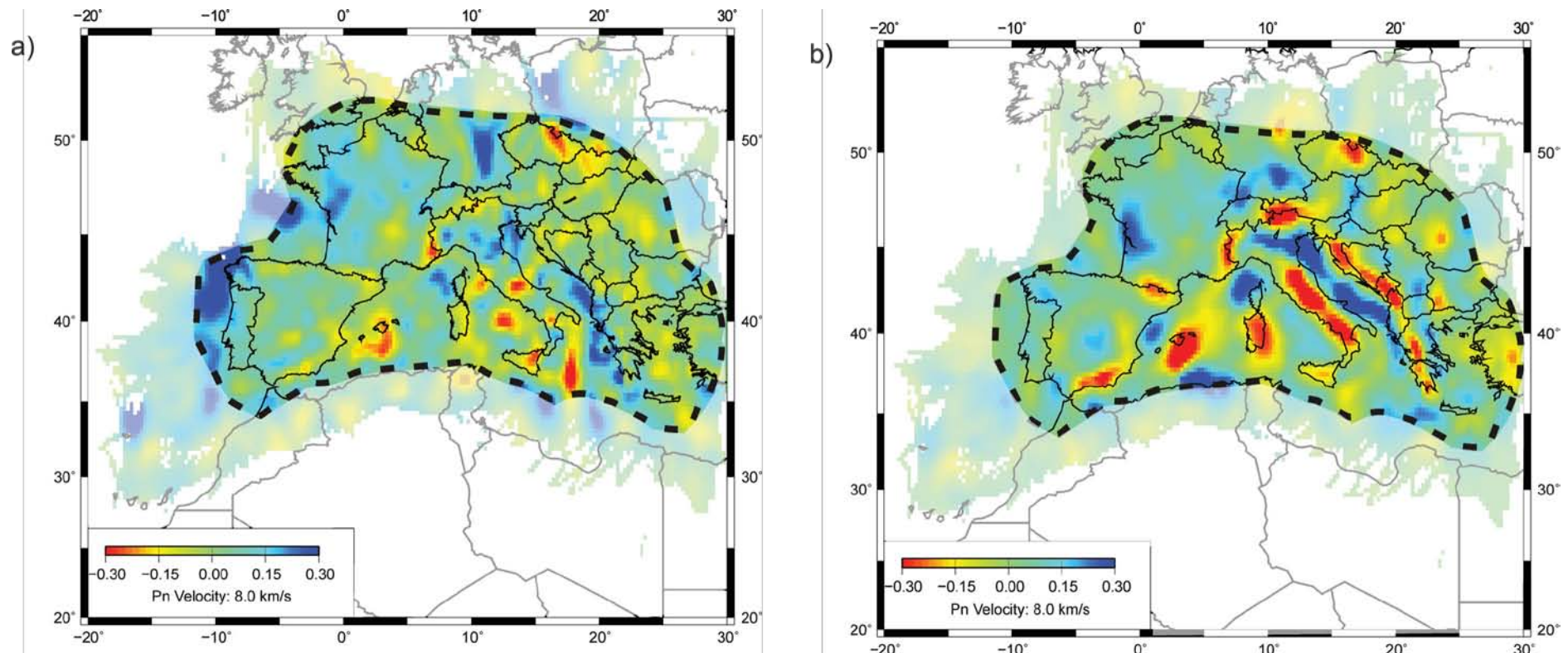


**Figure 4.5.** (a)  $Pn$  velocity anomalies with respect to 8 km/s assuming isotropic propagation (weight-damping factor: 1000). (b)  $Pn$  velocity anomalies including an anisotropic term (weight and anisotropic damping factor: 1000). The dashed line delimits the confidence zone; outside this area, the results are masked.

The most prominent high velocity zone extends along the Adriatic Sea, from the Po Basin to the Ionian Sea. Less prominent high velocity zones appear under large sedimentary basins, as the Ligurian, Aquitanian or Guadalquivir-Gharb basins. The Kabylies, in the central and eastern coast of Algeria, show another high velocity anomaly, while the Valencia Trough and the southern Alboran Sea exhibit also a less pronounced but well-constrained high velocity anomaly.

The *Pn* tomographic image here obtained has a relatively good consistency with the uppermost layer of the available regional and teleseismic 3-D tomographies (Bijwaard and Spakman, 2000; Piromallo and Morelli, 2003; Koulakov et al., 2009). The most prominent feature in both types of tomographic images is the low-velocity zone under the Dinarides-Hellenides, the Alps and the Apennines as well as the high velocity anomaly along the Po Basins and the Adriatic Sea. In the western Mediterranean, low velocities are observed south of the Balearic Islands and beneath the Betics. However, significant differences arise between the different tomographies in the Tyrrhenian and Provençal-Ligurian Basin, probably resulting from the lack of resolution in the upper layers in teleseismic tomography, which is greatly affected by abrupt variations in crustal thickness or velocity.

The resolution test discussed in the previous section of this chapter evidenced that the tomographic method here used allows to properly recovering only large-scale anisotropic features, as smaller ones may be the result of artifacts during inversion. Large anisotropic values (Fig. 4.6) appear beneath the Apennines, orientated subparallel to the belt and bending to NE-SW in the Calabrian Arc. The Alps show an arcuate variation of the anisotropic properties, from NS orientated FPD and a small degree beneath SE France to large values and E-W orientated FPD under the Eastern Alps. Clear anisotropy with FPD subparallel to the orogen is also observed beneath the Dinarides and the Hellenides. The Betics have large anisotropy with FPD following the topography of the belt till the Gibraltar Strait, but not clear evidences of anisotropy are observed beneath the Rif. In the Alboran Sea the FPD seem to shift smoothly from NS in the western part to NW-SE in its eastern section. Along the Valencia Trough, the magnitude of anisotropy is moderate and the FPD are parallel to the extension, The FPD shifts around the Balearic Islands to a NE-SW orientation between the Balearic Promontory and Algeria, where the anisotropy is stronger. Beneath Sardinia, FPD are

orientated NW-SW, changing abruptly to E-W under the Tyrrhenian Basin. Further North, another region with significant anisotropy is observed under southern Germany, an area still well-resolved by our data. The observed FPD are in this case oriented close to NNE-SSW. In general, the regions with high velocity anomalies do not show a consistent anisotropic pattern, while there is an overall correlation between the zones with a significant amount of anisotropy and those with low-velocity anomalies.

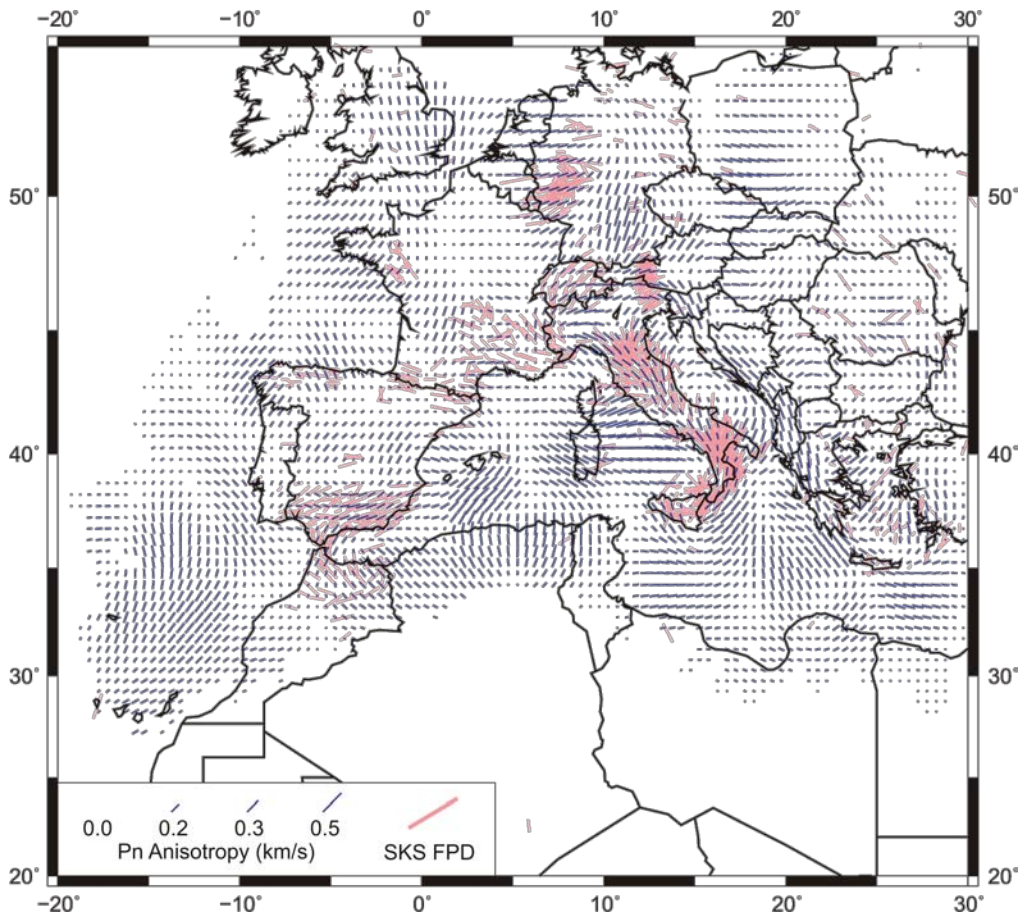


**Figure 4.6:** Anisotropic parameters recovered from the tomographic inversion. The orientation of the blue bars accounts for the fast polarization directions (FPD) in each cell. Its length shows the strength of the anisotropy. Red bars correspond to the published anisotropic parameters in the Euro-Mediterranean region from the analysis of SKS splitting (Wüstefeld et al., 2009)

For the inversion of the *Sn* phases, the same procedure has been considered, even if the number of travel-times and the resulting ray coverage is clearly poorer (Figure 4.1b). In a first step, the inversion is done in the isotropical case. The results (Figure 4.7a) show an overall similarity with the *Pn* inversion, even if some differences can be clearly observed. As discussed in previous selection, the inclusion of an anisotropic

term, although not evident, produces an effect very similar to the case of *Pn* phases. The velocity perturbations are sharper and have more lateral continuity than if only isotropic velocity variations are allowed (Figure 4.7b). This provides an a posteriori argument favoring the inclusion of an anisotropic term in the *Sn* velocity inversion. To better discuss the differences between the *Pn* and *Sn* velocity variations, Figures 4.8 (a) and 4.8 (b) show the  $Vp/Vs$  ratio calculated without and with anisotropic terms. Even if it has been shown that the interpretation of the  $Vp/Vs$  ratios in terms of Poisson ratio is difficult when the quality of the P and S velocities is significantly different (Eberhart-Phillips, 1990), this representation provides a good tool to compare the *Pn* and *Sn* tomographic images. Within the area properly resolved by both *Pn* and *Sn* data, the more stable areas (Adria Plate, Central Iberia, France) have larger  $Vp/Vs$  ratios, while the active zones, including the Betics, Western Mediterranean, Alps, Dinarides and Hellenides displays clearly smaller values.

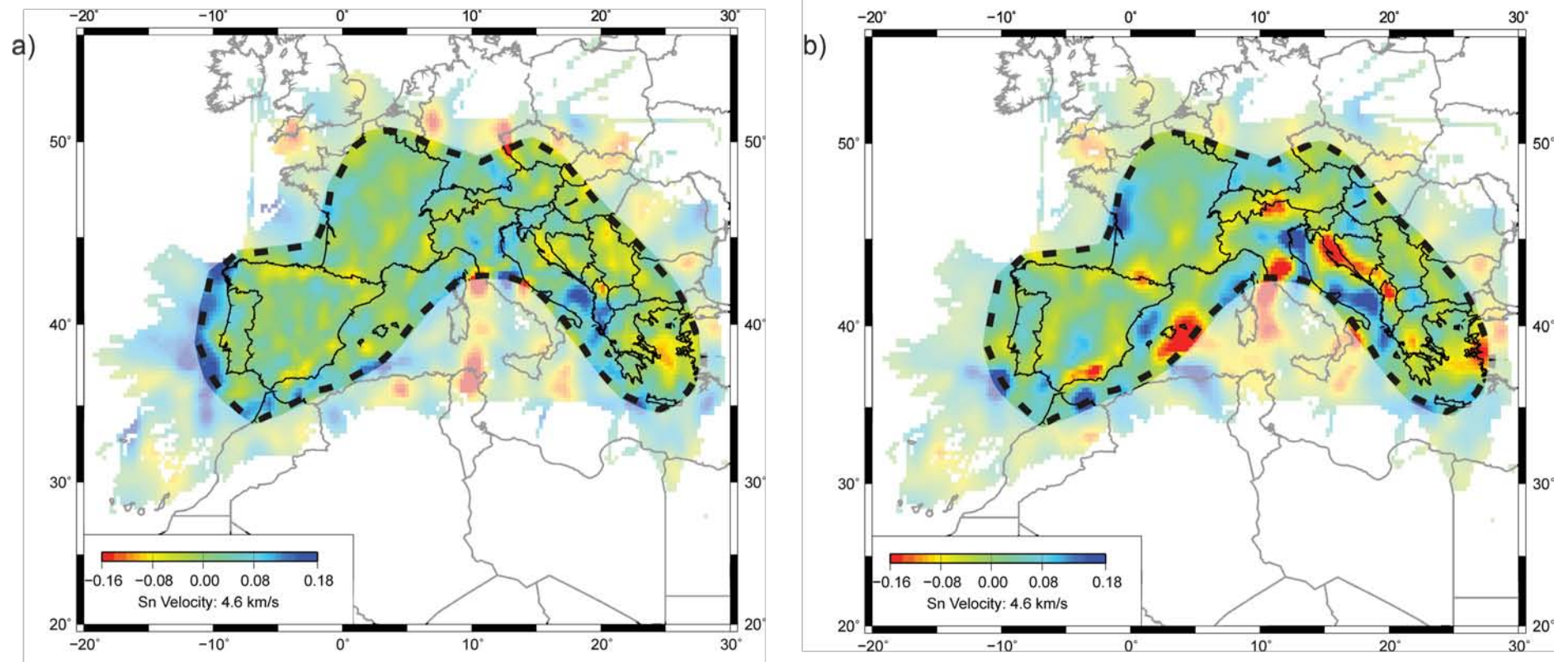


**Figure 4.7:** Obtained  $Sn$  velocity anomalies with respect to 4.6 km/s assuming isotropic propagation (a) and including also an anisotropic term (b). The damping factors are fixed to 600. The dashed line delimits the confidence zone; outside this area, the results are masked.

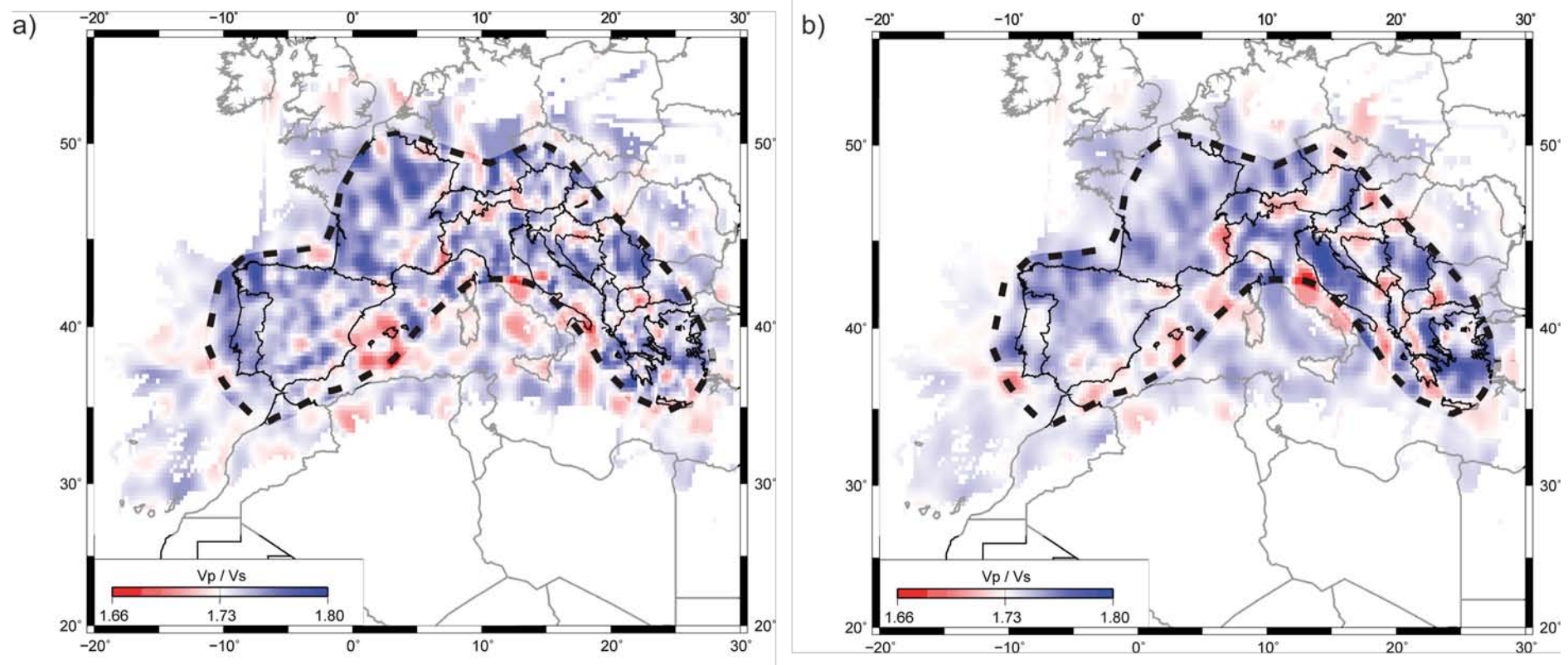


**Figure 4.8:**  $V_p / V_s$  ratios retrieved from the inversion assuming isotropic propagation (a) and including also an anisotropic term (b)

## 4.4 Discussion

Laboratory studies on peridotites samples at high-pressure conditions have shown that seismic velocities rapidly decrease with increasing temperatures (Sato et al., 1989). The presence of even small amounts of water can reduce the solidus temperature in the mantle, resulting in partial melt and low-seismic velocities (Karato and Jung, 1998). Therefore, the low-velocity zone observed beneath the main orogenic belts suggest abnormally high temperature conditions, implying uppermost mantle material close to solidus and related to the building of the orogens. Compositional changes or the presence of some amount of water into the upper mantle as a result of the Neo-Tethys and Mediterranean lithosphere subductions may also explain such low values.

Multu and Karabulut (2011) have recently presented a *Pn* tomography study of Turkey and adjacent regions, updating the previous work by Al-Lazki et al. (2004) and showing low-velocity anomalies beneath western Anatolia, Aegean Sea and Greece. Pei et al. (2011a) obtained a large scale *Pn* and *Sn* tomography model extending from 15° E to the Himalaya. Beneath the Dinarides and the Aegean Sea those authors identify low velocities, while high velocities are observed beneath the southern section of the Adriatic Plate. The results here presented confirm these points, and thus make possible to extend the tomographic images till the Atlantic Ocean, completing the imaging of the Alpine-Himalayan belt. As already proposed by Mele et al. (1998) using a limited number of travel-time readings, the large high velocity zone observed beneath the Po Basin and the Adriatic Sea may be due to its rather stable character, as it is widely accepted that stable cratonic areas result in high *Pn* velocity. The low-velocity is below the Dinarides-Hellenides can be associated to the presence of a mantle wedge (Hearn, 1999). Below the Apennines, the low-velocity zones have probably a thermal origin related to its backarc position. It can be observed that the low-velocity zone in our results is limited to the Apennines and does not extend to the Tyrrhenian Sea as it has been imaged by telesismic tomography (e.g. Kaulakov et al., 2009). Beneath the Alps, the two important low velocities observed seem to be separated by a zone of normal velocity located roughly under the Insubric line, which marks the structure between the European and Adriatic plates. Lippitsch et al. (2003) using high-resolution tomography showed that at 90 km depth the velocity distribution is significantly different, with high velocities beneath Southwest Alps and the Adriatic Plate a low velocity beneath western

Switzerland. The uppermost mantle beneath southern Germany shows a well-defined high velocity anomaly already identified in a regional *Pn* tomography presented by Song et al. (2004) and interpreted as resulting from an ancient process of underplating. Under the Pyrenees, the presence of low velocities only in its Central-Eastern section may reflect the different character of the Alpine orogeny along the chain. The Alpine deformation begins in the Late Cretaceous at the eastern Pyrenees (Vergés et al., 1995) and only in Eocene to Miocene times in the Cantabrian Mountains (Gallastegui et al., 2002). The shortening along the chain has been evaluated in 150 km in central Pyrenees (Muñoz, 1992) but limited to 75 km in the western Pyrenees (Teixell, 1998). Hence, the low-velocity zone corresponds to the area where the Alpine deformation began and where the shortening has been more important.

Active seismic surveys beneath the Betics (Banda and Ansorge, 1980) have evidenced a low-velocity region beneath a thin mantle lid. This region, located between 38-40 km and 60 km depth, is grossly consistent with the large low-velocity observed in both *Pn* and regional and teleseismic tomographies and its origin should be related to hot mantle. Teleseismic wave tomography has identified a high velocity slab under the Alboran Sea at depths exceeding 100-150 km. Garcia-Castellanos and Villaseñor (2011) recently proposed a model that includes a lateral tear of this slab beneath the Betics, which may be consistent with our observation of low velocities beneath the Betics but not further south along the Gibraltar Arc. This region has been investigated using *Pn* phases by Calvert et al. (2000) and Serrano et al. (2005) using different sets of data, which had evidenced the presence of a robust low-velocity anomaly with significant anisotropy beneath the internal Betics. Calvert et al. (2000) observed a high velocity slab beneath the southern part of the Alboran Sea which was related to a rather cold mantle beneath this zone and which appears also in our results. However, heat flow data (Soto et al., 2008) does not seem compatible with this hypothesis, as it defines a hotter region (>650°C) at Moho depths running SW-NE across the central part of the Alboran Sea.

The observation and interpretation of the low-velocity zones close to the Balearic Islands and beneath Sardinia are of particular interest because, even if previous S-wave tomographies depicted the presence of a low-velocity zone in the Algero-Provençal and Tyrrhenian basins at depths of 75-100 km (Marone et al., 2004, and Legendre et al.,

2012), its presence at shallower levels has not been previously described. The Balearic Islands low-velocity zone is limited to the east by the Hannibal Ridge and includes the Emile Baudot escarpment, a large right-lateral transform zone orientated NE-SW and interpreted as marking the western migration of the Alboran microplate (Acosta et al., 2001). Mauffret et al. (2004), suggested that the Hannibal Ridge was an active spreading center until Tortonian (8 Ma) or even after (6 Ma). Multibeam mapping led to the discovery of the SW Mallorca Volcanic Field, an area with a relevant number of volcanic pinnacles related to Miocene to recent volcanism (Acosta et al., 2001). Therefore, the observed low-seismic velocities are probably related to the recent tectonics in the area. The eastward migration of the volcanic area associated to the counter-clockwise rotation of the Corsica-Sardinia block resulted in ongoing volcanism in Sardinia until 12 Ma, followed by a sporadic anorogenic phase developed during the Late Miocene-Quaternary (Beccaluva et al., 2011). Hence, here again the observed low-velocity zones are consistent with the presence of hot materials at shallow levels. The geometry of both low-velocity zones allows speculating with an original unique low-velocity zone, split during the emplacement of the Corsica-Sardinia block. Many reconstructions of the Western Mediterranean suggest continuity between the subducted slabs beneath the Calabrian and the Gibraltar Arcs along the Algerian margin, even if global tomography images do not confirm this point (Rosenbaum et al., 2002). The high velocity anomaly beneath the Kabylies, observed both in our *Pn* results and in global tomographic images, can then be related to a segmented slab affected by vertical tearing.

Comparing *Vp* and *Vs* tomographies it can be observed that tectonically active zones tend to present smaller *Vp/Vs* ratios, while the stable areas have higher values. However, this point has to be taken with caution, as it has been shown that the difference in the number and quality of the *Pn* and *Sn* observations makes difficult the interpretation of this ratio. Pei et al. (2011b) proposed an approach based in the back-projection of *S-P* time differences that can be used in future works to assess the validity of this results.

The presence of anisotropy within the upper mantle is nowadays well established (Babuska and Cara, 1991). The origin of such anisotropy is related to the strain included lattice preference orientation (LPO) of the mantle minerals, in particular of olivine (e.g.

Nicolas and Christensen, 1987). Anisotropy thus provides one of the best tools to investigate deformation in the upper mantle somehow extending structural geology to depth. In tectonically active areas, FPD are expected to mark the direction of flow. In zones without present-day large-scale tectonic activity, LPO result from strain from the last significant tectonic episode preserved in the subcrustal lithosphere or from dynamic flow in the asthenosphere. During the last decades, the analysis of *SKS* splitting has provided a large amount of information related to mantle anisotropy. However, the relationship between the results of those studies and the anisotropic parameters retrieved from *Pn* tomography must be taken with caution, as significant resolution differences arise between both cases. *SKS* provides a good lateral resolution, only limited by the Fresnel zone beneath each station, but fails to constraint the deep location of the anisotropic zone. On the other hand, *Pn* tomography samples only the uppermost part of the mantle thus providing a good resolution in depth but its lateral resolution is limited, as it has been discussed in the previous section of this chapter. Schmid et al. (2004) presented a compilation on FPD inferred from *SKS* splitting analysis over the Euro-Mediterranean zone. In the last years, new experiments have improved the knowledge on anisotropy over this region, as summarized in Figure 4.6, build using the results compiled by the “Splitting Data Base” (Wüstefeld et al., 2009).

The good correlation between the inferred *Pn* FPDs and the trend of the main orogenic belts suggest that the origin of this anisotropy is related to the strain field. In the Aegean region the FPD tends to be orientated NE-SW (trench-perpendicular) in the back-arc, where anisotropy is related to mantle wedge flow. Close to the trench, the FPD tends to be parallel to its orientation, even if the results show significant scattering (Evangelidis et al., 2011). The *Pn* anisotropic parameters obtained in our study show similar pattern, with FPD clearly parallel to the trench and changing to a more scattered, roughly NE-SW orientation in the back-arc region. Enderle et al. (1996) summarized the results from the large amount of deep seismic sounding profiles sampling southern Germany along different directions. They found 3-4 per cent anisotropy with FPD orientated N30°E below the Moho and changing slightly with depth. The results from our study are well consistent with this feature. In the Northern Apennines, the FPD derived from *SKS* splitting are orientated roughly parallel to the belt, even if some variations can be observed between the different domains (Salimbeni et al., 2008). The *Pn* results here presented show very similar pattern, with a main NW-SE component but

shifting to NNE-SSW in the Adrian region and showing a large EW component beneath Tuscany. Large variations in the anisotropic parameters are observed in the Tyrrhenian Basin. While its central and southern part is dominated by a moderate, E-W orientated FPD, the northern edge, between Corsica and Italia, shows higher anisotropy with FPD orientated NE-SW to ENE-WSW. In the southern part of the Italic Peninsula, the observed FPD shows a clear rotation following the Calabrian Arc. The same pattern has been derived from *SKS* splitting and has been interpreted as the result of mantle flow around the subducting slab (Baccheschi et al., 2008). The anisotropic parameters obtained from *Pn* and *SKS* splitting are also very similar beneath the western Alps, with FPD following again the trend of the belt, from a NE-SW orientation to the North, to a roughly NS orientation in the southern termination of the Alps. Here again, the *SKS* results have been related to mantle flow around the subducted slab (Barruol et al., 2011). The available anisotropic parameters retrieved from *SKS* splitting beneath the Pyrenees (Barruol et al., 1998) show a clear ESE-NWN orientation, while our results do not show any evidence of anisotropy, suggesting that its origin is deeper. *SKS* results in the Balearic Islands show a ESE-WNW FPD which clearly differs from the NE-SW oriented anisotropy appearing south of the islands in our work. This suggests again changes with depth of the anisotropic properties. Along the Gibraltar Arc, *SKS* results found a clear rotation of the FPD following the arc curvature, with similar strength in both terminations (Díaz et al., 2010). While the *SKS* results beneath the Betics are clearly consistent with the anisotropic properties inferred from *Pn* tomography, beneath northern Africa the results differ: *SKS* analysis shows NW-SE oriented FPD, while *Pn*-derived fast directions are orientated NNE-SSW with intensity vanishing to the South. Beneath the Alhoceima region, at the SE termination of the Arc, *SKS* data changes abruptly from NW-SE orientation beneath western Morocco and eastern Algeria. In the following chapter we will focus more specifically in the Northern Moroccan area (the Rif Cordillera and surroundings).

The overall similarity between anisotropic parameters retrieved from *Pn* tomography and from the splitting of teleseismic *SKS* observed beneath some orogens (Betics, Apennines, Alps, Dinarides-Hellenides) suggest that the anisotropy is rather uniform from the base of the crust to depths of about 300 km (the lower depth range where significant anisotropy is expected). In those cases, the anisotropic pattern may be explained by deformation in the subcrustal lithosphere beneath the orogens, with

extensions along the arc and compression orthogonal to it. Under those conditions, dewatering of the slab will create near solidus conditions in the mantle, hence explaining the low velocities observed beneath the orogenic belts. The hot temperatures will allow the lithospheric mantle to deform coherently, favoring the LPO and thus enhancing the anisotropy. Beneath some regions where an anisotropic origin related to mantle flow around subducted slab has been proposed (SE Alps, southern Gibraltar Arc) *Pn* and *SKS* anisotropic parameters clearly differ, suggesting different levels of anisotropy.



# Chapter 5: 2-D velocity-depth transects from wide-angle reflection/refraction seismic profiling

## 5.1 Introduction

In this section we present seismic crustal velocity models along two mostly-orthogonal wide-angle seismic reflection (WA) transects crossing the Rif in the NS and EW directions. This geometry is aimed to acquire seismic data over the zone where a significant low Bouguer anomaly has been previously identified Hildenbrand et al. (1988). The Bouguer gravity anomaly database maintained by the International Gravimetric Bureau ([BGI](http://bgi.omp.obs-mip.fr/data-products/Grids-and-models/wgm2012); <http://bgi.omp.obs-mip.fr/data-products/Grids-and-models/wgm2012>) shows that a very prominent -150 mGal gravity low is located to the south of the Internal Zones of the Rif, over the External Zones and the western region of the Gharb foreland basin (Figure. 5.1). The gravity anomaly increases towards the oceanic areas, reaching maximum values of up to 250 mGal over the Atlantic and from 50 to 150 mGal in the Alboran Basin and its transition towards the oceanic Algerian basin. The new seismic models derived in this Chapter from our data will be also converted to density and the predicted Bouguer anomaly compared with the observed one from BGI database.

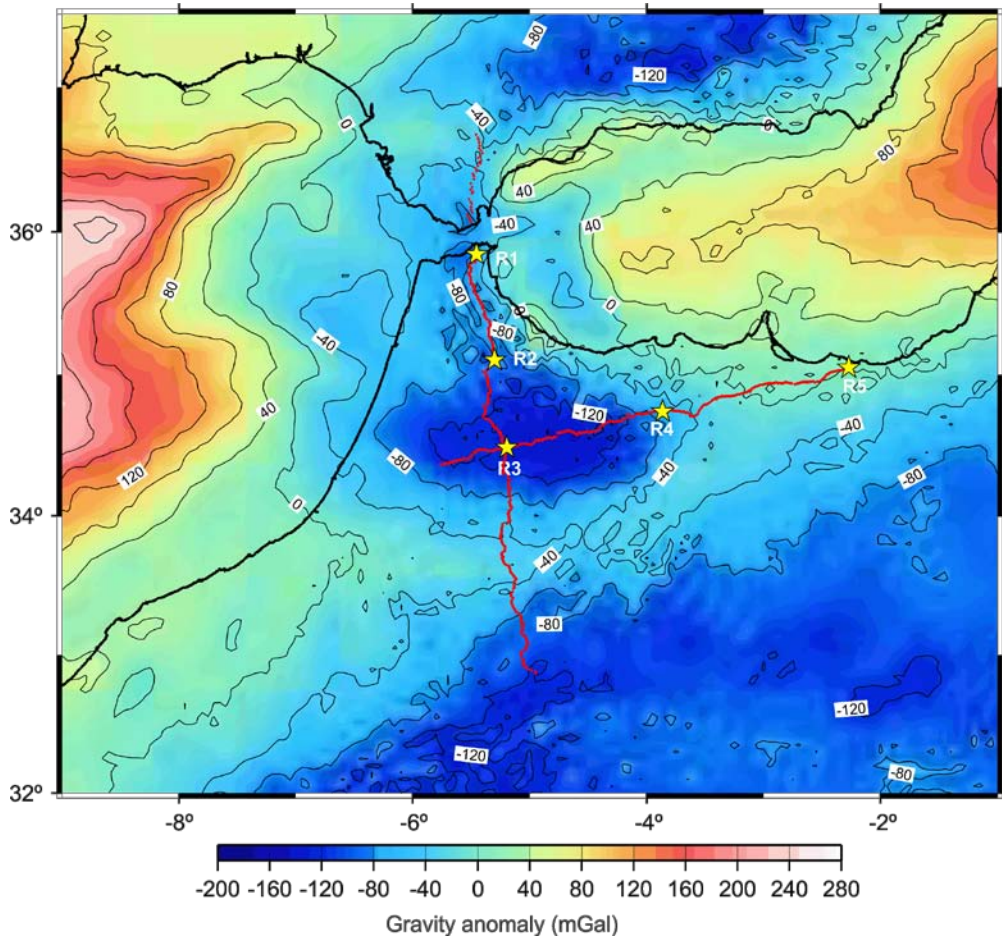


**Figure 5.1:** Gravity anomaly contour map of the southern Iberian Peninsula and northern Morocco. Bouguer anomalies have been extracted from the BGI (Bureau Gravimétrique International, <http://bgi.obs-mip.fr>). The contour interval is 40 mGal. The black lines indicate the location of the seismic profiles. Note that the wide-angle transects closely follow the axes of the minimum of the Bouguer anomaly (-150 mGal) beneath the Rif domain.

In October 2011 we acquired one 330 km-long and another 430 km-long wide-angle seismic reflection profiles oriented, approximately, EW and NS (Figure 5.2). The profile directions were designed to approximate the overall Rif strike and dip directions and conform to major and minor axes of the elliptical Bouguer anomaly pattern (Figure 5.1). The EW transect extends across the Rif orogen from the Gharb Basin to the Algerian border. The NS line extended 70 km into the Iberian Peninsula and over 300 km within Morocco to the Mid-Atlas, overlapping with the SIMA seismic wide-angle transect in the Atlas Mountains (Ayarza et al., 2014). Jointly, SIMA and the NS RIFSIS profile extend 700 km-long from the northern Sahara desert into southernmost Iberia.

The Iberian portion of the NS RIFSIS profile is not reversed as there were no source points in Iberia.

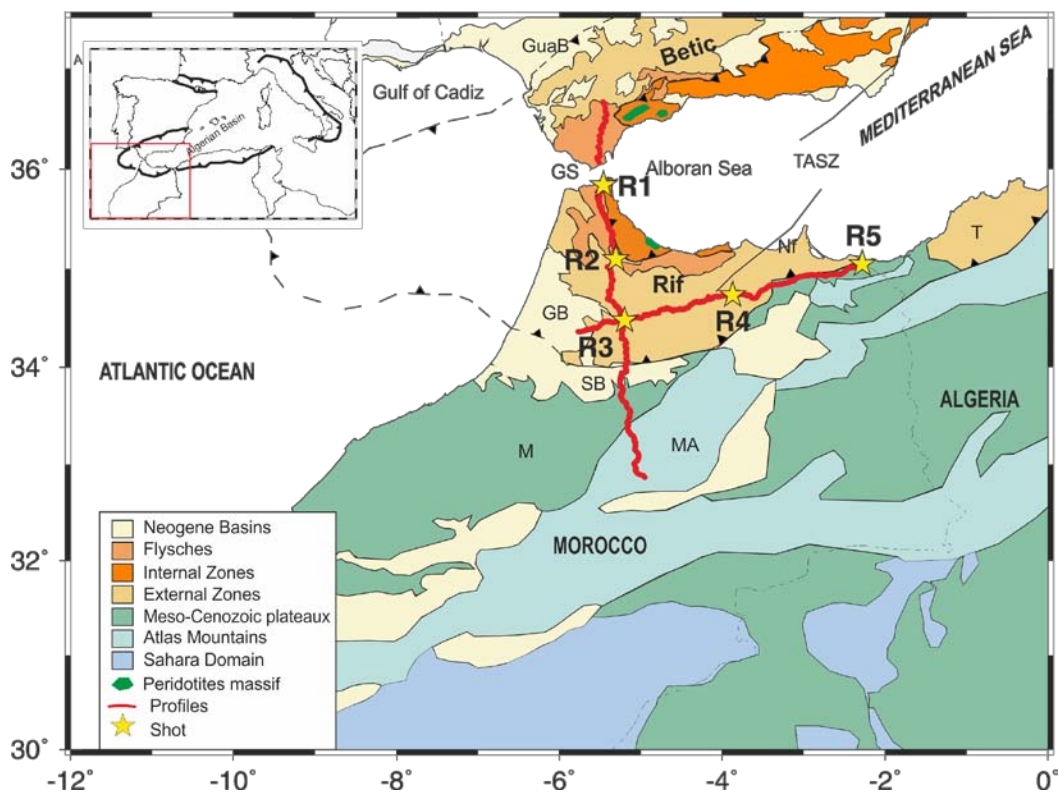


**Figure 5.2:** Map of Southern Iberia and Northern Morocco with the location of seismic wide-angle profiles acquired through the RIFSIS project (in red, the digital stations; stars, the source points) and simplified geology of the study area. The major tectonic domains and boundaries are indicated. GB: Gharb Basin; GuaB: Guadalquivir Basin; GS: Gibraltar Strait; M: Meseta; MA: Middle Atlas; Nf: Nekkor fault; SB: Saïss Basin; T: Tell Mountain TASZ: Trans-Alboran Shear Zone. The dashed line represents the geometry of the Gibraltar Arc. The inset shows location within the Euro-Mediterranean domain and includes an outline of the Westernmost Mediterranean Alpine Belt.

Each of the 5 sources consisted of 1Tn of chemical explosives in 2 boreholes and was recorded by 845 digital seismographs with one-component 4.5 Hz geophones (Reftek RF125 IRIS-PASSCAL Texans). The average receiver spacing was 750 m. Shots R1 through R3 were located along the NS line, and R3-R5 were along the EW line. Shot R3 is at the intersection of the two profiles. All shots were recorded by all the stations producing fan shots for 3-D control on deep structure (Carbonell et al., 2014). Up to 402 seismographs were deployed along the EW profile and 443 along the NS profile including 35 in Spain. The signal-to-noise ratio in our data is within the usual range for

this kind of experiments, providing a reasonably good overall data quality although shot R1 near Gibraltar has low signal-to-noise ratio at offsets larger than 80 km.

The wide-angle seismic data of the two RIFSIS profiles were processed including amplitude recovery, frequency filtering using a classical band-pass Butterworth filter (3–10 Hz) and phase enhancement by a lateral phase coherency filter (Schimmel and Gallart, 2007). This latter procedure allows a better identification of weak seismic arrivals at large offsets, as it was presented previously in Chapter 3 (Figure 3.8). The coherency filter was especially valuable in the case of shot R1 allowing us to identify arrivals from 80 km to 140 km offsets. A total of 2297 picks were obtained, 1154 from the NS profile and 1143 from the EW.

P-wave velocity-depth models were derived by forward modeling travel-times of diving and reflected waves using RAYINVR software (Zelt and Smith, 1992). Additional geological and geophysical constraints were considered in the modeling procedure where available. For the NS profile we start from the velocity-depth model presented by Ayarza et al. (2014) from the interpretation of the SIMA profile, crossing the Atlas and partially overlapping our profile. At the northern edge, the seismic models by Medialdea et al. (1986) were also taken into consideration. Different geological results compiled in Chalouan et al. (2008) have been used to get an initial estimation of the geometry and velocities in the uppermost sedimentary layers. Identified seismic phases (shown and labeled in the figures) follow the conventional nomenclature:  $Ps$  and  $Pg$  denote refractions through the sedimentary cover and the basement, respectively;  $PiP$ ,  $PcP$  and  $PmP$  stand for P to P reflections produced at the top of the middle crust, top of the lower crust and Moho discontinuity, respectively; and  $P1$ ,  $P1P$  identify refraction and reflection events on a locally limited sedimentary layer. Because the shot spacing is rather large, varying from about 80 to 140 km, phases from the sedimentary layers and the upper crust generally are not reversed, whereas the deeper phases  $Pg$ ,  $PcP$ , and  $PmP$  generally are. Despite careful inspection and analysis of the filtered and unfiltered record sections, we have not found clear evidences of arrivals displaying a convincing lateral correlation and which could be attributed to lower crustal or Moho refracted phases. Hence, we have preferred to use only the well identified reflected phases as the observations for modeling. In the following sections we describe: 1) the quality of the data; 2) the parts of the models that are well constrained and 3) the travel-

time picks and fit. Estimated uncertainties of the travel-times picks are, on average 0.05 s for  $Ps$ , 0.1 s for  $Pg$  and between 0.1-0.2 s for reflected phases  $PiP$ ,  $PcP$  and  $PmP$ . The derived P-wave velocity models reproduce the picked travel-time branches with a very good agreement. The observed travel-time misfits (usually less than 0.15 s) are reasonable in view of contributing factors such as the acquisition geometry, local oscillations on topography, outcropping lithologies, etc.

## **5.2 Lateral variations of the structure beneath the External Rif domain: East-West profile from Gharb Basin to the Algerian border**

The EW profile is sampled from shot records R3, R4 and R5 (Figures 5.3, 5.4 and 5.5). Rapid structural variations beneath the External Rif domain can be inferred from the deeper phases  $PcP$  and  $PmP$  recorded along this transect.

Shot R3 was recorded ~50 km to the west, towards the Gharb Basin, and 280 km to the east, along the External Rif to the Algerian border. Two sedimentary arrivals are observed in the eastern section:  $Ps_1$  is the first arrival to ~15 km and  $Ps_2$ , to ~30 km offset. A satisfactory fit in travel-times is obtained (see Figures 5.6 and 5.7) with a velocity gradient between 3.2 and 3.8 km/s for the first sedimentary layer, and 4.25 to 5.2 km/s for the second. In the western part, the first arrival to 15 km offset (-15 km in Figure 5.3), identified as the refracted phase  $P1$ , arrives earlier than the same arrival at similar offsets to the east. This  $P1$  phase, a first arrival to 40 km offset, travels in a layer with an average velocity of 4.8 km/s. This phase and its associated reflection  $PIP$  indicate that the Neogene deposits of the Gharb Basin extend to depths of 10 km. The  $Pg$  phase can be correlated at offsets of 30 to 80 km in the eastern part with an apparent velocity of 5.8 km/s, but is less visible.  $PiP$  energy is observed beyond 30 km offsets at reduced times of ~5 s to the east almost a 1 s delay compared to the west. Weak  $PcP$  arrivals are identified in the eastern section at offsets of 50-90 km, and relatively high amplitude  $PmP$  arrivals at offsets of 80-190 km (Figure 5.3a, b). When examined carefully, we identify two arrivals with different slopes. The first event at 80-130 km offset arrives at ~10 s reduced travel-time. We identify a second event with velocity greater than 8.0 km/s at 110-140 km and 13-10 s travel-times (Figure 5.3). These two arrivals suggest a complex Moho-topography. We have modeled the two arrivals as

different  $PmP$  branches resulting from a west to east shallowing of the Moho from more than 50 km to less than 30 km. The Moho ramp occurs over a distance of 45-50 km beneath the surface expression of the Nekkor fault/TASZ, at the eastern end of the Bouguer gravity anomaly over the Rif (Figures 5.1 and 5.7).

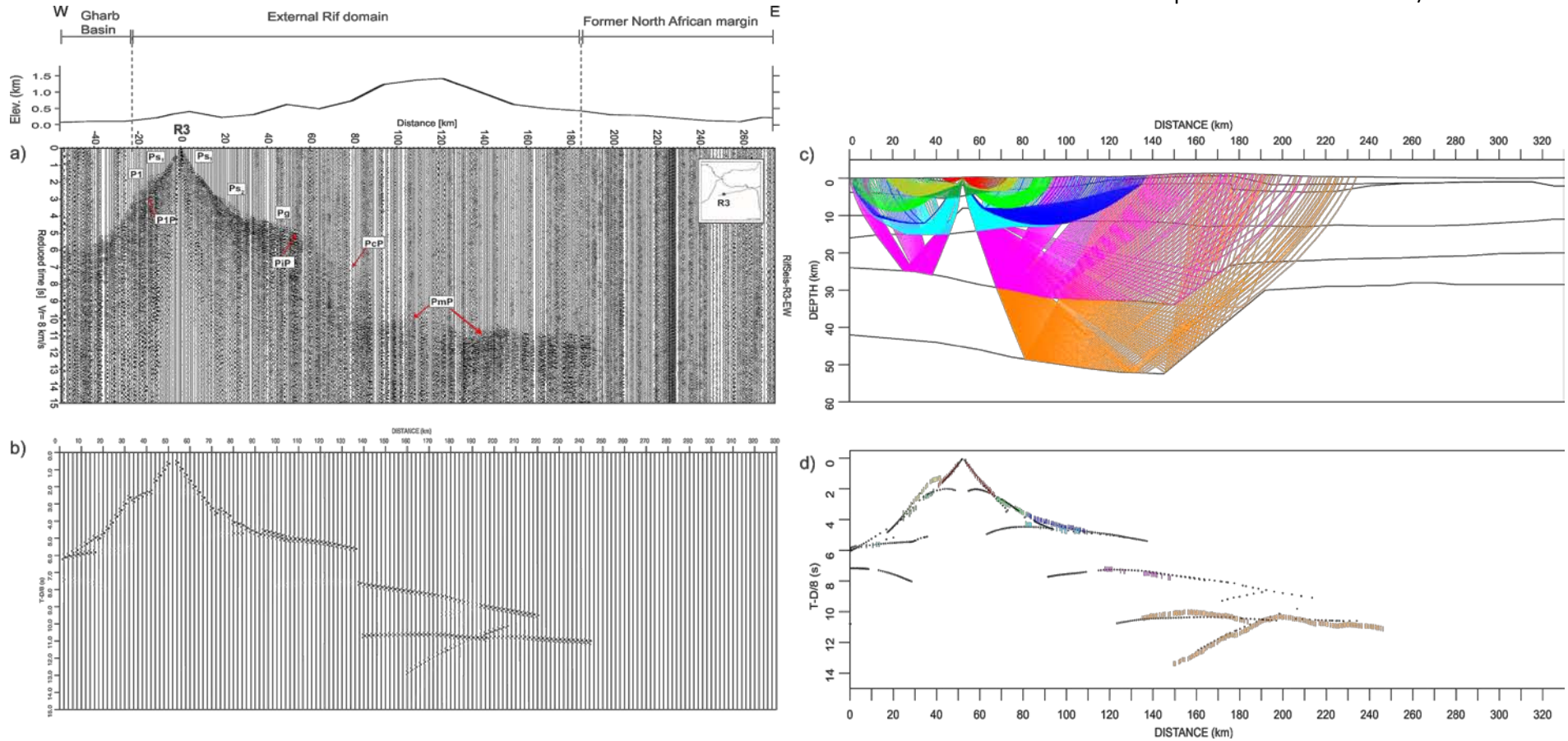


**Figure 5.3:** Shot R3 recorded along the EW profile with the synthetic seismograms, the ray tracing diagram and the travel-time picks considered with topography and geological regions on top. **(a)** R3 shot record, applying a reduction velocity of 6 km/s and a bandpass filter of 3-10 Hz, showing the quality of the data and the phases identified (see label descriptions in text) and used to build up the seismic velocity model. **(b)** Synthetic seismograms calculated from the final model **(c)** Ray tracing diagram revealing the extension of the interfaces constrained in the final model. **(d)** Fitting between travel-time picks determined from the data (in colors according to their travel paths) and the ones modeled (in black) by the RAYINVR package (Zelt and Smith, 1992). The vertical bars associated to the travel-time picks are indicative of the error estimates considered for each pick. Colors meaning: red:  $P_s$  phase; green:  $P_s$ ; light green:  $P_1$ ; dark green:  $P_{1P}$ ; dark blue:  $P_g$ ; light blue:  $P_{cP}$ ; purple:  $P_{mP}$

Shot R4, in the center of the EW profile (Figures 5.2 and 5.4), clearly exhibits extraordinary lateral differences in crustal structure beneath the Rif resulting from the change in lower crustal structure. Sedimentary phases are observed as first arrivals to 20 km offsets to the west and 30 km to the east, suggesting that the sediments thin from east to west from 4 to 2 km thickness. As will be discussed later, this step in the sediment thickness is located beneath the surface expression of the Nekkor fault. The velocity in the sedimentary layers increases from 4.3 to 5.3 km/s. The  $Pg$  phase is visible to 60 km offsets at apparent velocity 5.9 km/s. A reflected event ( $PiP$ ), appearing approximately symmetrically under the shotpoint from 20 to 100 km offset, is interpreted to come from the top of the middle crustal layer at ~16 km depth. To produce the relatively high amplitude of the  $PiP$  arrivals (Figure 5.4a, b), a marked velocity contrast is required, which we model as a transition from 5.9 to 6.3 km/s across the interface. Hence, a 10 km thick upper crust is constrained under R4 in contrast with values of 5 km constrained beneath shotpoint R3 (Figure 5.7).

The  $PcP$  phase is only observed east of R4 (Figure 5.4), at around 5.5 s and at offsets of 60 km. Also to the east of R4, following the  $PcP$  phase we observe a high amplitude  $PmP$  phase at 6.5 s (Figure 5.4). The 1 s delay between both phases suggests the presence of a rather thin, ~5 km lower crust to the east of R4. To the east  $PmP$  is identified at offsets greater than 70 km to the eastern end of the profile, modeled as a reflection from a Moho at 30 km depth.

The most striking feature in the R4 shot record (Figure 5.4) is the asymmetry observed in  $PmP$  across the record section.  $PmP$  in the west appears from -170 to -60 km offset at reduced travel-times of 10-12 s, while in the eastern it is observed around 7 s. For an offset of 120 km, the difference between the  $PmP$  phase arrivals at both sides reaches a 4 s (Figure 5.4). This difference is accommodated in the final model by a 20 km difference in crustal thickness (Figures 5.4 and 5.7).

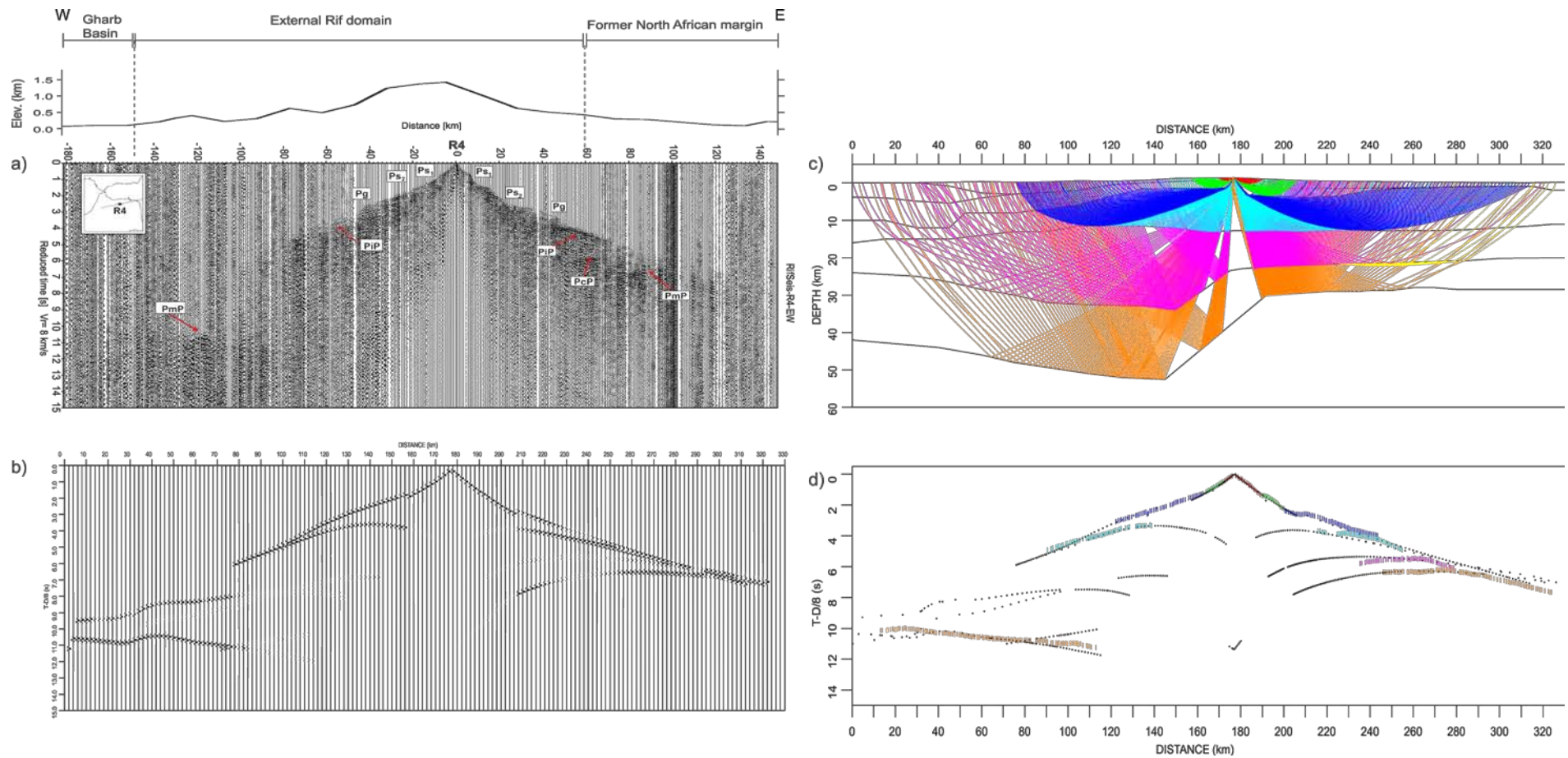


**Figure 5.4:** Shot R4 recorded along the EW profile with synthetic seismograms, ray tracing diagram and the travel picks considered. See caption in Figure 5.3 for details

Shot record R5 (Figure 5.5) reveals events from the sedimentary cover, middle crust, lower crust and Moho. In detail a short sedimentary phase is observed to 10 km offset, resulting from a thin (2-4 km) sedimentary layer with a velocity gradient of 3.0 to 3.8 km/s (Figures 5.5 and 5.7). The  $Pg$  phase is correlated to 100 km offset with an average velocity of 6.0 km/s. The  $PcP$  is visible after 50 km offsets (at about 5 s reduced time at 60 km) and the  $PmP$  after 60 km offsets, at about 2 s later on, constraining a Moho at the eastern end of the profile at ~29 km depth (see Figures 5.5 and 5.7). At offsets between 100-250 km, the observed arrivals from the deep crust are fitted in the model as corresponding to  $PcP$  and refracted energy within the lower crust (yellow travel-time picks in Figures 5.5 and 5.6). They could not be attributed to  $PmP$  to be consistent with the Moho location established after the  $PmP$  fitting from reverse shot R4 (Figure 5.4). Hence, the lower crust in the east is 7-8 km thick with a velocity gradient from 6.75 to 6.9 km/s, in strong contrast with the western part of the profile, where the lower crust thickness exceeds 15 km, although its top is poorly resolved from  $PcP$  phases.

$Pn$  phases that would constrain the upper mantle velocities could not be identified for any of the shots. This is not unusual in areas with significant lateral variations in the crustal thickness, a weak velocity gradient at the uppermost mantle or a smooth crust-mantle transition. However, this latter explanation seems not well in agreement with the short  $PmP$  critical distances generally observed in our sections. We have fixed an average velocity of 8 km/s in the uppermost mantle and verified that even if this value is not constrained by direct  $Pn$  observations, a 2-3% modification of the velocity ratio between the lower crust and mantle velocities results in clear misfits between observed and theoretical  $PmP$  critical distances (Figure 5.6). We increased 0.2 km/s the lower crust velocity, increasing the velocity from 6.8 to 7.0 km/s; and decreased 0.3 km/s the uppermost mantle velocity, decreasing the velocity from 8.0 to 7.7 km/s. The uppermost mantle topography has not been changed.

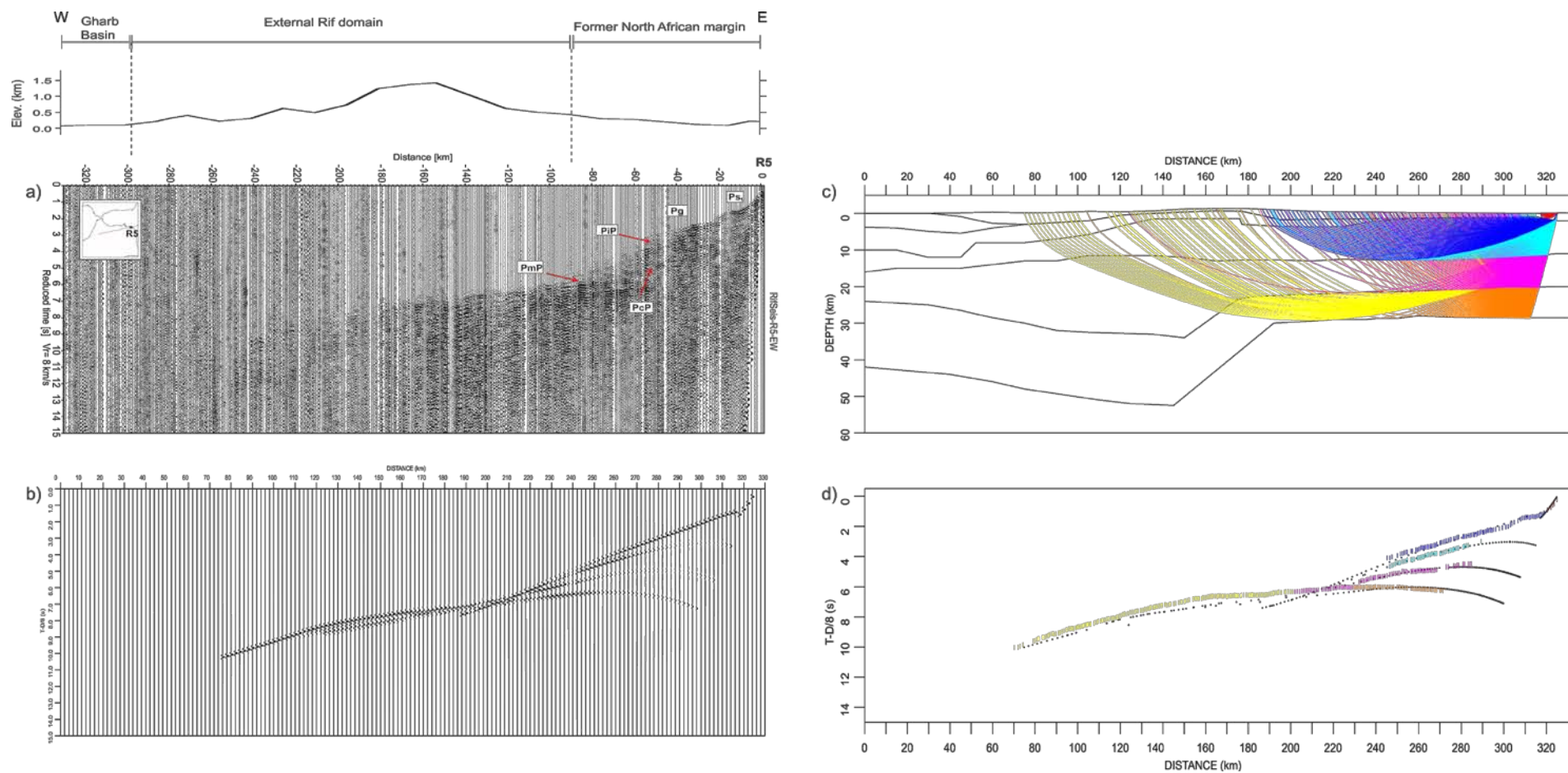


**Figure 5.5:** Shot R5 recorded along the EW profile with synthetic seismograms, ray tracing diagram and the travel picks considered. See caption in Figure 5.3 for details

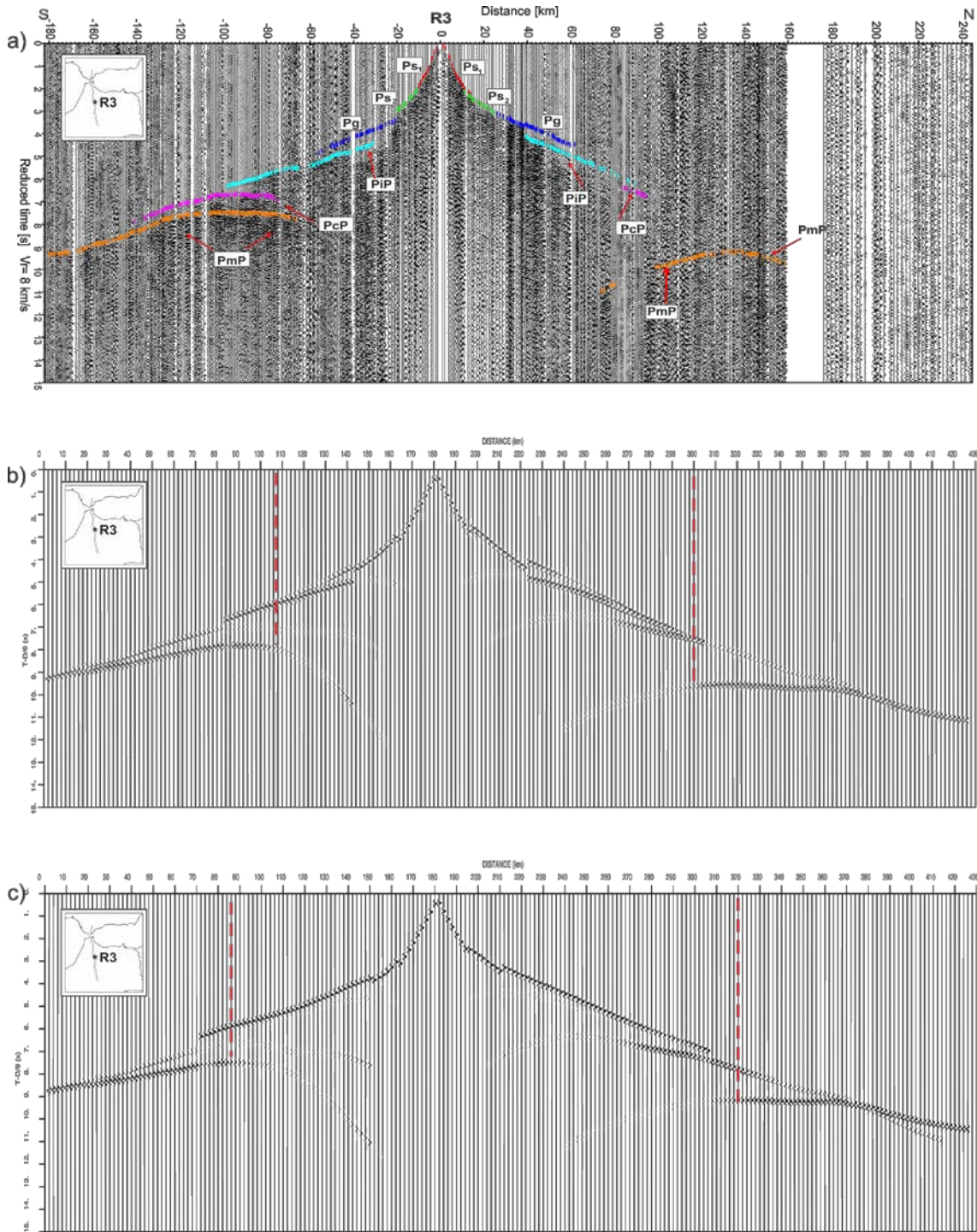


**Figure 5.6:** (a) Amplitude-normalized seismic section for shot R3 along the NS transect, with indication of the phase picking (see labels in the text), (b) synthetic seismograms calculated for the final model, and (c) synthetic seismograms after applying perturbations of 2-3% in the ratio between the lower crust velocity and the uppermost mantle velocity. Red dashed lines show the  $PmP$  critical distances

In summary, in the crustal model along the EW RIFSI transect (Figure 5.7) the thickness of sediments is clearly decreasing from west (Gharb Basin) to east (Algerian border). Near R3 up to three sedimentary layers are interpreted in contrast to only one in R5. Upper, middle and lower crustal levels are constrained by refracted and reflected

phases ( $Pg$ ,  $PiP$ ,  $PcP$  and  $PmP$ , respectively). The bottom of the crust is well defined from  $PmP$  phases, although the lack of  $Pn$  arrivals prevents to constrain upper mantle velocities. A major change in crustal thicknesses can be observed directly in the R4 shot section, which shows differences of 5 s in the  $PmP$  arrivals at offsets of 120 km. Forward modeling has shown that a rapid change of ~20 km in Moho depth within 50 km horizontal distances is needed to explain these observations. The Moho in this area is sampled in both directions (shots R3 and R4) and hence the final model is here well constrained. Maximum depths around 50 km are found beneath the high topography of the External Rif domain, whereas a thin crust with a 29 km Moho depth is interpreted in the foreland and Atlasic terranes up to the Algerian border.

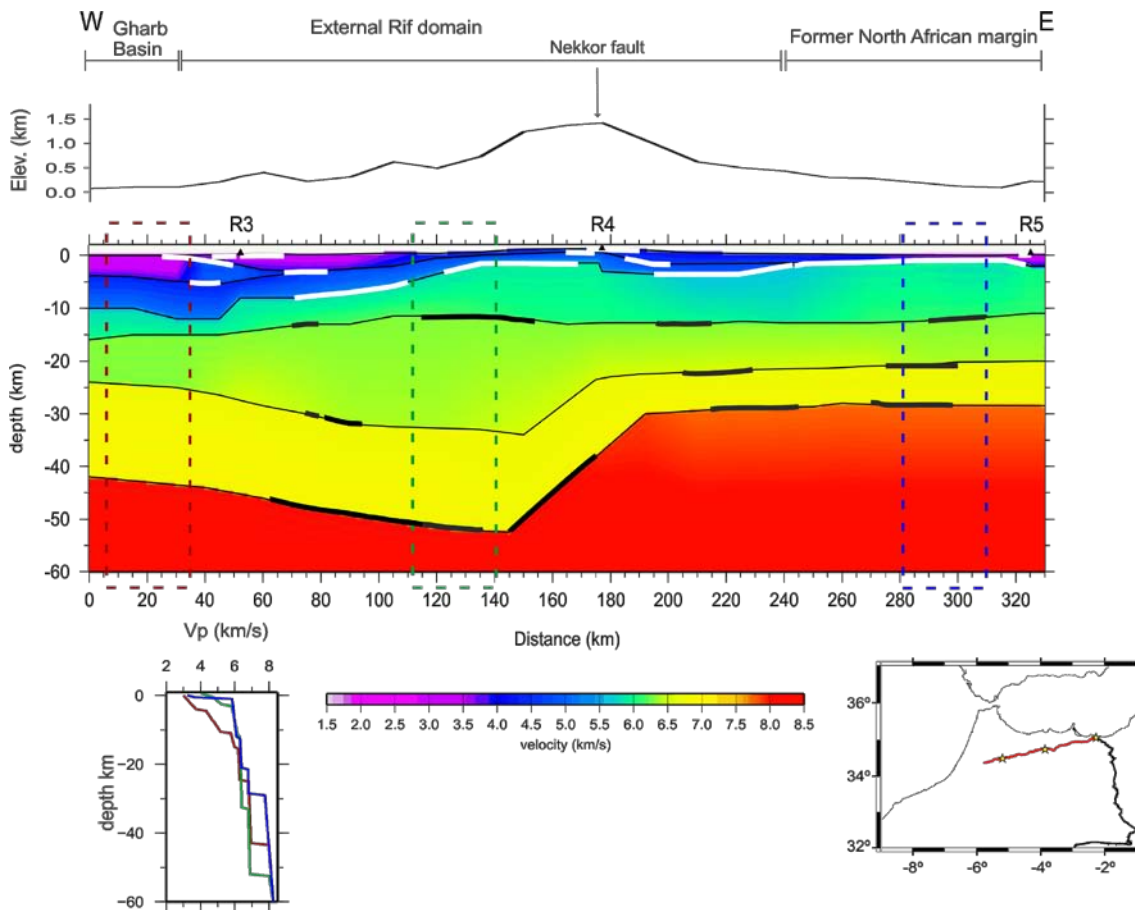


**Figure 5.7:** Crustal velocity-depth model determined along the EW profile with a vertical exaggeration of 2:1. The geologic domains are labeled on top of the model, and the topographic profile is sketched. Bold lines indicate layer segments directly sampled by seismic reflections. The vertical rectangles indicate the position where 1-D velocity-depth functions have been estimated, beneath the Gharb Basin (brown), the External Rif domain (green) and the former North African margin (blue).

### 5.3 North-South Rif Transect, from Middle Atlas domains to the Betics range

The North-South profile crosses the Internal and External Rif domains and the transition to the Middle Atlas in the south and to the Betics in the north. This profile, extending 430 km consisted of three shots, R1-R3 (Figure 5.2). Shotpoint R3 is at the intersection of the NS and EW transects. Shot R1 was located 6 km south of the Moroccan Mediterranean coast (Figure 5.2). In Morocco all three shot records show two sedimentary first arrivals:  $Ps_1$  to 10-20 km offset and  $Ps_2$  to 30-40 km (Figures 5.8, 5.9 and 5.10). North of the Gibraltar strait, the first station on the Iberian Peninsula is located at 35.5 km offset, and no sedimentary waves are visible on R1. From R1 average velocities for  $Ps_1$  and  $Ps_2$  are 4.0 to 4.8 km/s with layer thicknesses of 2 and 5 km, respectively (Figures 5.8c and 5.11). The  $Pg$  phase is visible up to offsets of 60 km north and south, with an average velocity of 5.8 km/s and intercept times of 4.5 to 5 s, probably due to the relatively thick flysch terranes around the shotpoint. The  $PiP$  phase can be identified from 30 to 80 km in both directions. Low amplitude arrivals characterize the  $PcP$  phase, identified between 70-130 km to the south and between 60-80 km to the north. For both  $PiP$  and  $PcP$  phases, arrival times are delayed ~1 s to the north relative to the south one, suggesting 5-10 km thickening of the upper-middle crust beneath the Betics relative to the northern Rif (Figure 5.11). After applying lateral coherency filtering (Schimmel and Gallart, 2007),  $PmP$  can be identified at offsets between 50-140 km to the south and, between 60-90 km to the north. Arrival times are approximately the same for the same offset, indicating a rather constant Moho depth, ~42 km, under the area sampled by R1 (Figure 5.11).

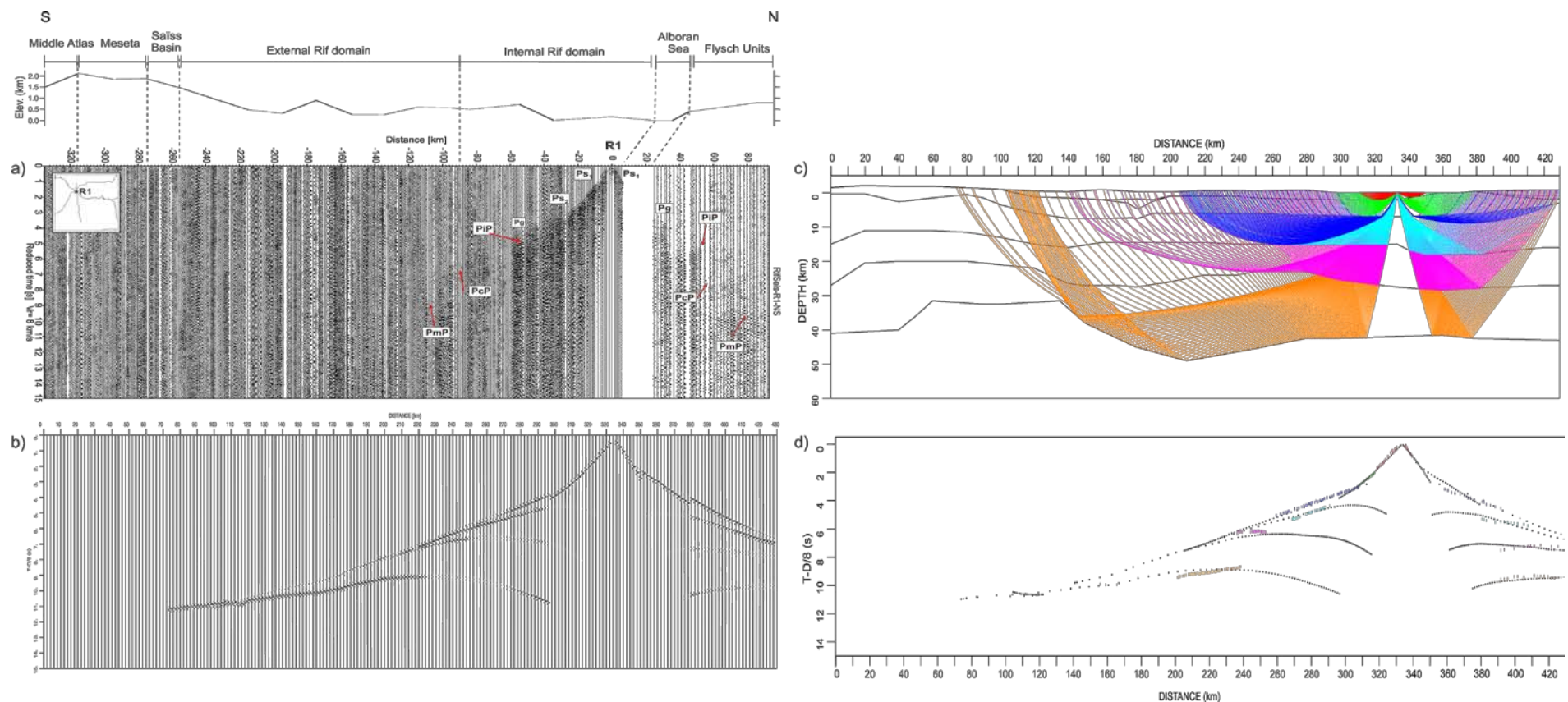


**Figure 5.8:** Shot R1 recorded along the NS profile with synthetic seismograms, ray tracing diagram and the travel picks considered. See caption in Figure 5.2 for details

The R2 shotpoint is located ~85 km to the south of R1 (Figure 5.2). The sedimentary phases,  $Ps_1$  and  $Ps_2$ , have velocity values and gradients similar to those at R1. The  $Pg$  phase is identified to offsets of 80 km with an intercept time of 4.5 s. Intracrustal reflections  $PiP$  and  $PcP$  are similar to R1 (Figures 5.8 and 5.9). The  $PcP$  phase is rather weak to the south, in contrast to higher amplitudes to the north to 140 km offset.  $PmP$  has the highest amplitudes and is identified from 80-180 km offset to the south, at reduced times of 11-8 s.  $PmP$  is not identified to the north.

R3 is located ~155 km from the R1 (Figure 5.2). As in the other shot records,  $Ps_1$  phases are first arrivals to offsets less than 18 km and are followed by a  $Ps_2$  phase which shows clear differences in apparent velocities north and south (Figure 5.10). The  $Ps_2$  phase to the north has a higher apparent velocity than the corresponding phase to the south, and to  $Ps_2$  on the other two shots R1 and R2. Shot R3 in the corresponding EW record section indicated a relatively shallow (1.8 km) sedimentary interface separating  $Ps_1$  and  $Ps_2$ , giving rise to  $P1$  and  $P1P$  in Figure 5.3. Although these phases are not easily recognized in the NS R3 record section (Figure 5.10), the marked difference observed in the  $Ps_2$  apparent velocities to north and south is evidence for the locally limited sedimentary layer from the EW profile.

$Pg$  is clear and can be identified to 90 km offset south, and 60 km offset north (Figure 5.10). The average apparent velocity is 5.7 km/s with rather large intercept times of 4.5 s north and 5 s south. This constrains the thick Neogene basin below the shotpoint to ~5 km depth. The  $PiP$  phase appears from 40-100 km south, and 30-100 km north, with similar arrival times indicating that the upper crust has a near constant thickness on both side of shotpoint R3 (Figure 5.10). In the model (Figure 5.11) the basement is located at 5 km depth, while the bottom of the upper crust is reached at 15 km. The  $PcP$  phase has been interpreted only to the south (see Figure 5.10). This phase is observed at offsets of 80-140 km with low amplitude arrivals at 7.5 to 8 s respectively. The base of the crust is constrained by the  $PmP$  phase, a relatively high amplitude arrival identified at times around 8 s at offsets greater than 70 km south of R3, and with lower amplitudes from 100-160 km to the north, at reduced time of ~9.5 s. The time difference in  $PmP$  arrivals is evidence of an increase in crustal thickness below R3, with the Moho at ~47 km depth (Figure 5.11). This is consistent with the R3 observations along the EW profile (Figure 5.7). Additional constraints on the southern

part of the NS profile are provided by the SIMA project data, a similar wide-angle transect across the High and Middle Atlas that overlapped the NS RIFSIIS transect (Ayarza et al., 2014). At the northern end of the profile, in the Betics domain, constraint on the sedimentary structure and upper crust was provided by Medialdea et al. (1986).

In summary, the crustal model along the NS RIFSIIS transect consists of two sedimentary layers with average velocities of 3.5 and 4.2 km/s inferred from the observed first arrivals ( $Ps_1$ ,  $Ps_2$  and  $Pg$ ). The upper, middle and lower crusts are constrained by the refracted and reflected phases ( $Pg$ ,  $PiP$ ,  $PcP$  and  $PmP$ , respectively). The average velocities within the crust are 5.9, 6.2 and 6.8 km/s. As for the East-West profile we have assumed an 8 km/s velocity below the Moho. Crustal thickness reaches 43 km beneath the Betics and the Internal Rif domain, while under the External Rif sampled area it increases to 47-49 km, with progressive thinning southward into the Middle Atlas where the Moho is found at 31-32 km depth, consistently with the results derived further South by Ayarza et al. (2014).

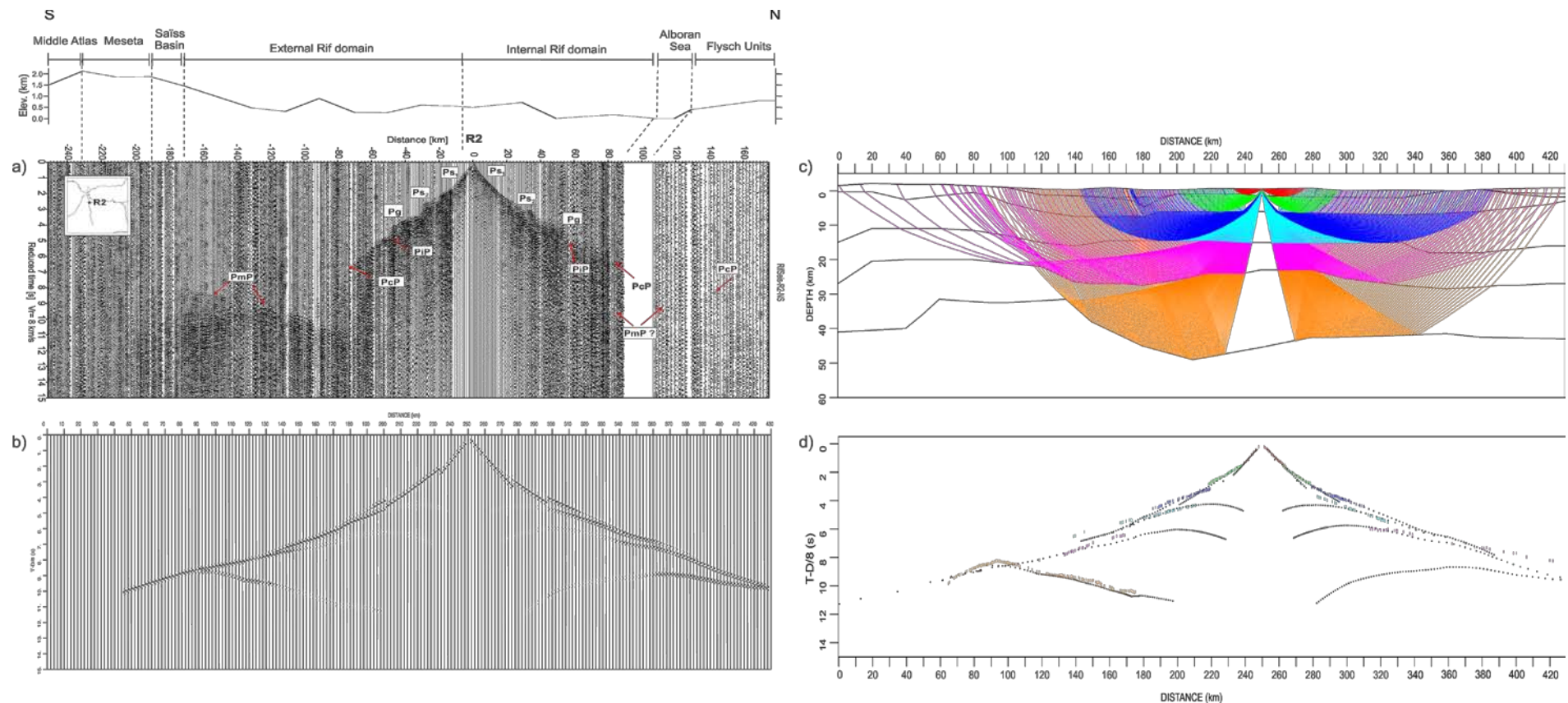


**Figure 5.9:** Shot R2 recorded along the NS profile with synthetic seismograms, ray tracing diagram and the travel picks considered. See caption in Figure 5.3 for details

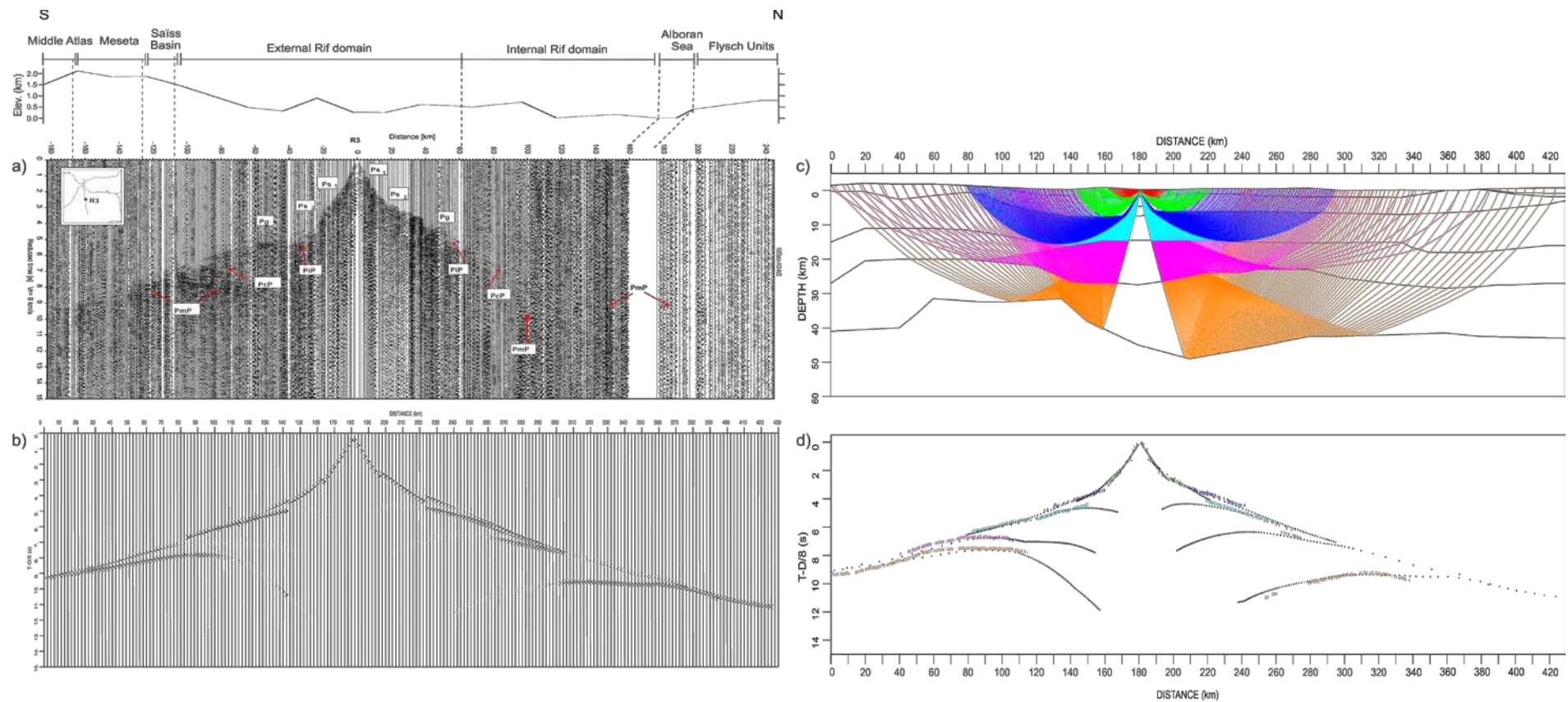


**Figure 5.10:** Shot R3 recorded along the NS profile with synthetic seismograms, ray tracing diagram and the travel picks considered. See caption in Figure 5.3 for details

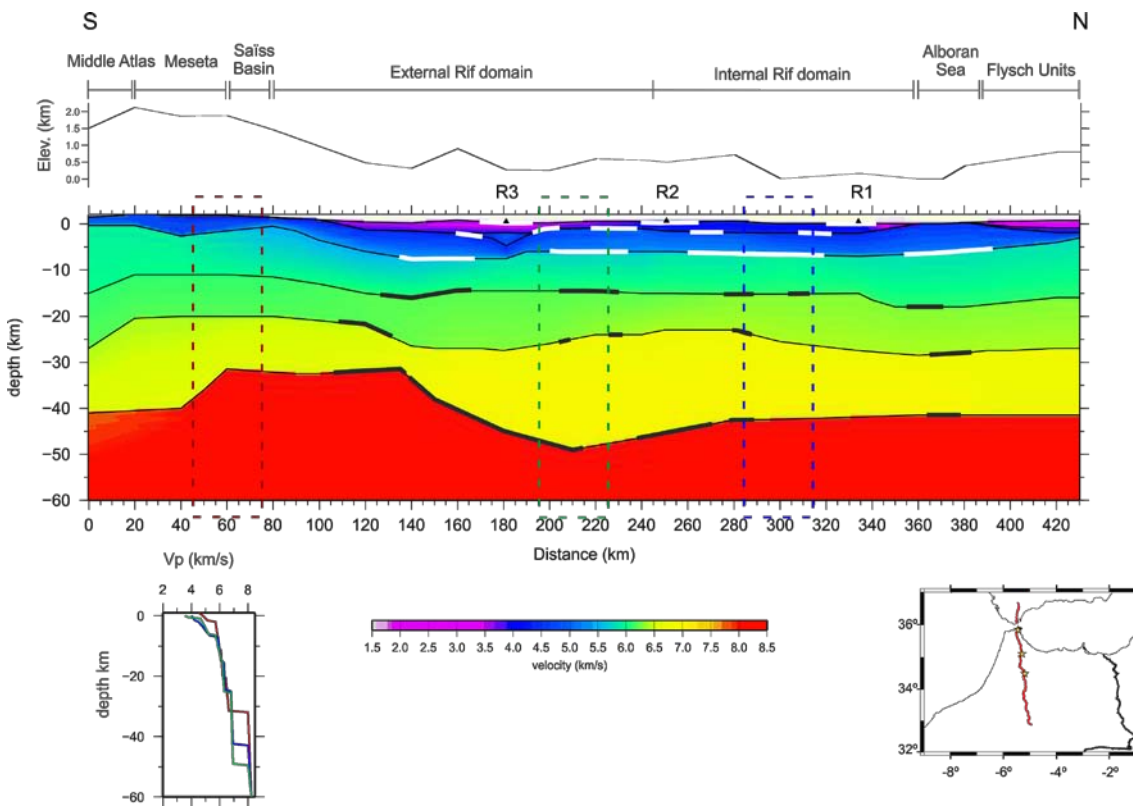


**Figure 5.11:** Crustal velocity-depth model determined along the NS profile, with a vertical exaggeration of 2:1. The geologic domains are labeled on top of the model, and the topographic profile is sketched. Bold lines indicate layer segments directly sampled by seismic reflections. The vertical rectangles indicate the position where 1-D velocity-depth functions have been estimated, beneath the Moroccan Meseta (brown), the External Rif domain (green) and the Internal Rif domain (blue).

## 5.4 Gravity control of wide-angle models

The marked lateral variations in crustal thickness inferred from the seismic models are an outstanding structural feature that can be checked against the corresponding gravity signature. The gravity anomaly beneath the Rif is remarkably low,  $\sim -150\text{mGal}$  (Figure 5.1). These Bouguer values are of similar magnitude as those over the Betics and the Atlas, where gravity lows are found over significantly higher elevations. The Rif gravity low is an ellipse slightly shifted to the southwest of the Internal Zones, centered over the External Zones and the western region of the Gharb foreland basin (Figures 5.1 and 5.2). The latter is most likely related to the presence of a large volume (up to 8 km) of continental sediments in the western part of the basin (Hafid et al., 2008).

To account for lateral variations perpendicular to the strike of the profiles, gravity data have been averaged over a  $\pm 25\text{ km}$  strip of the profiles with the resulting standard deviation computed and displayed in Figures 5.12-5.14. The gravity models have been built using the geometry derived from seismic modeling. An averaged P-wave velocity value has been considered for each layer in the seismic model and the corresponding densities were calculated using the empirical relations by Brocher (2005), which applies to most lithologies, except mafic- and calcium rich rocks, as it was described in Chapter 3 (Figure 3.14). Although the modeled crustal density distribution appears compatible in overall with the P-wave seismic velocity models, the corresponding Bouguer anomalies showed around 20% misfit with the observed ones along the transects (Figure 5.12). A significant improvement in the fitting has been reached just by keeping the layering geometry and considering rather small variations in the density distribution in specific areas, especially in the sedimentary layers (see Figures 5.13 and 5.14).

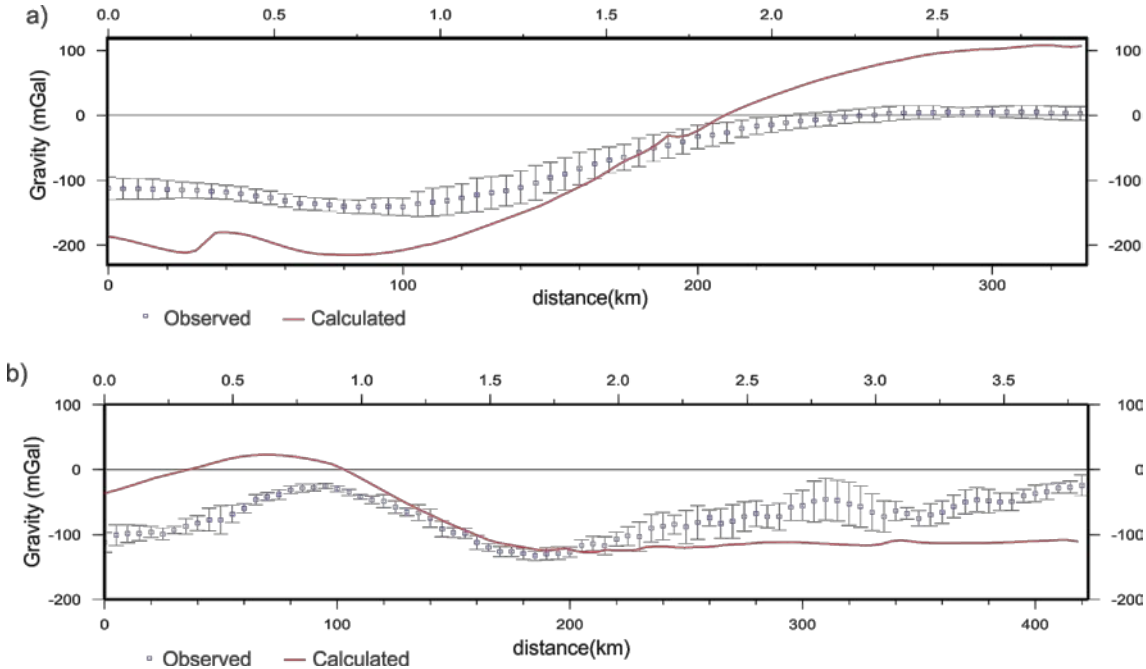


**Figure 5.12:** 2-D projection of the gravity measures extracted from the gravity anomaly map (Figure 5.1) along a 50 km wide strip. The vertical bars denote standard variation at each measure point, data fitting with 2-D gravity profile (in red) generated by density crustal model directly from the average  $V_p$  of each layer. **(a)** Crustal density model from the EW profile. **(b)** Crustal density model from the NS profile.

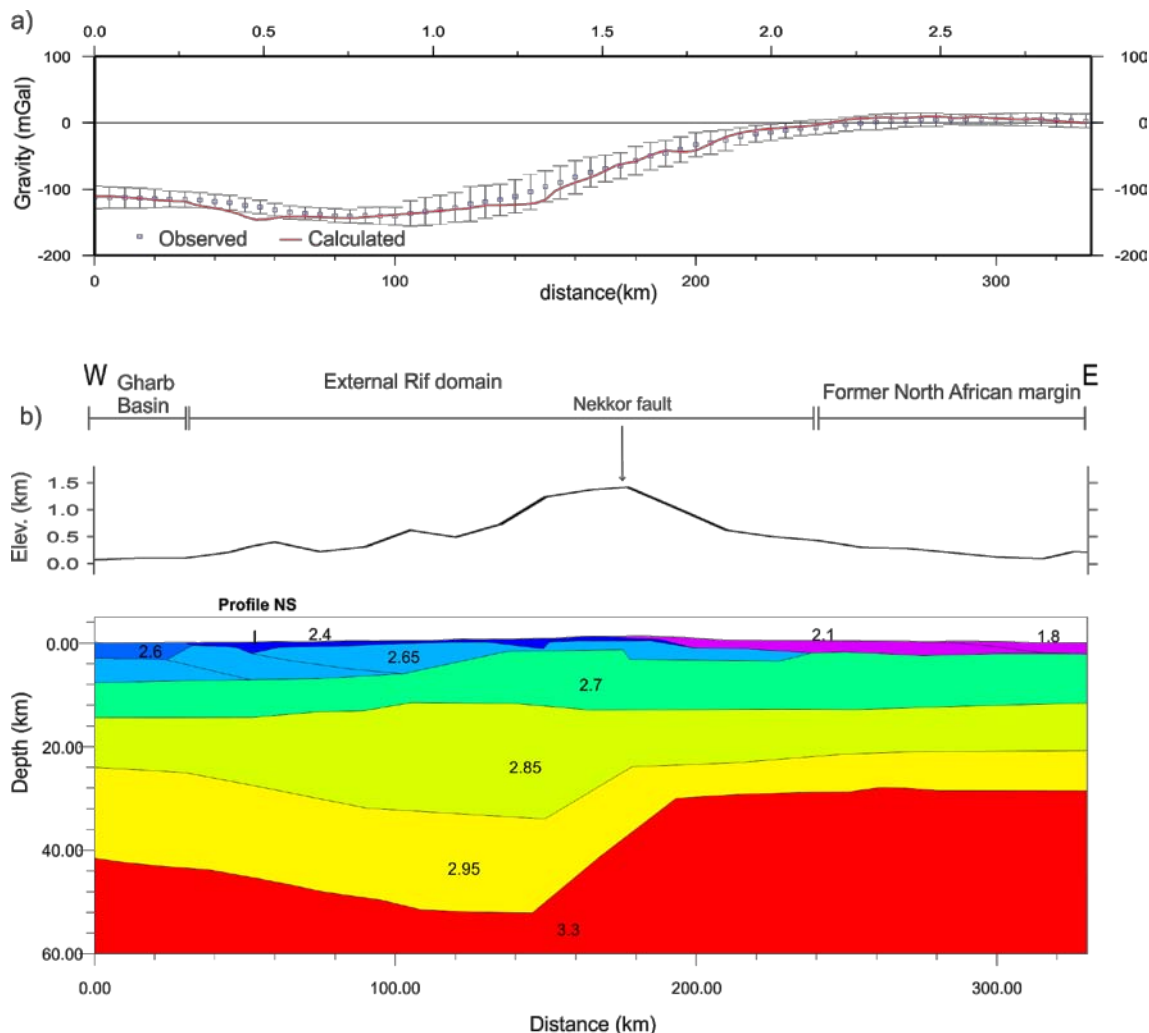


**Figure 5.13:** Crustal density model obtained by gravity forward modeling along the EW transect. (a) 2-D projection of the gravity measures extracted from the gravity anomaly map (Figure 5.1) along a 50 km wide strip. The vertical bars denote standard variation at each measure point, and the red line denote the data fitting with the 2-D gravity profile generated by the density crustal model; (b) distribution of the densities within the crust, inferred from the seismic model (Figure 5.7). Numbers are density values in  $\text{g}/\text{cm}^3$ . The geometry for the crustal bodies has been kept and the density structure has been slightly modified to improve the fitting.

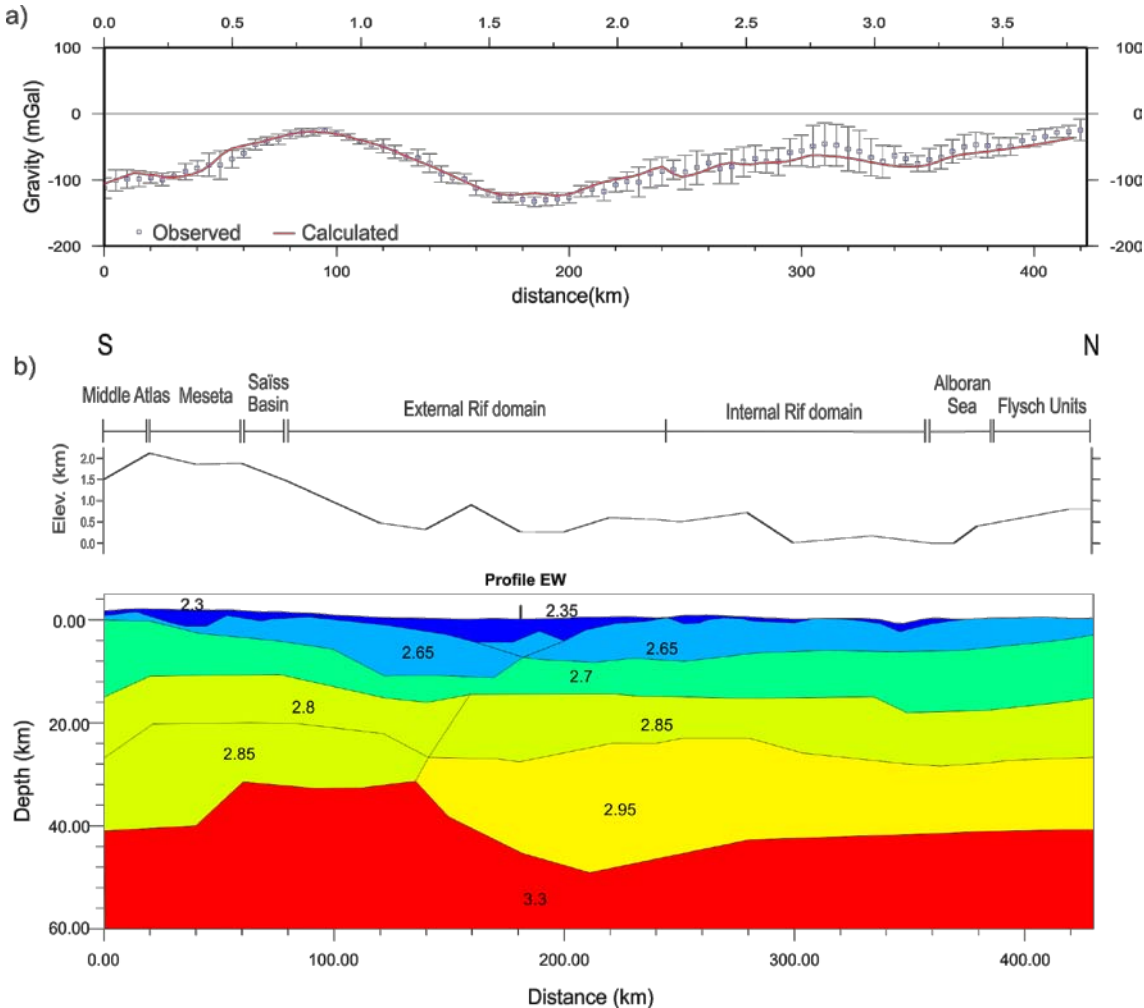


**Figure 5.14:** Crustal density model obtained by gravity forward modeling along the NS transect. **(a)** 2-D projection of the gravity measures extracted from the gravity anomaly map (Figure 5.1) along a 50 km wide strip. The vertical bars denote standard variation at each measure point, and the red line denote the data fitting with the 2-D gravity profile generated by the density crustal model; **(b)** distribution of the densities within the crust, inferred from the seismic model (Figure 5.11). Numbers are density values in  $(\text{g}/\text{cm}^3)$ . The geometry for the crustal bodies has been kept and the density structure has been slightly modified to improve the fitting.

For both transects (Figures 5.13 and 5.14) the calculated gravity values lie very close to average measurements and well within the standard deviation of the projected gravity estimates. Particular attention has been taken in the segments directly sampled by seismic reflections (thick black and white lines in Figures 5.7 and 5.11) where we have kept the exact geometry as obtained from the velocity model. In all cases the preferred option has been to slightly change the density profile of the crustal layers instead of modifying their geometry. Accordingly, the NS profile (Figure 5.11) displays lateral density variations at crustal levels from north to south. Densities slightly lower than

expected are inferred in the northern segment (from 0 to 140 km), in particular in the lower crust.

## 5.5 Discussion

The seismic refraction/wide-angle reflection experiment presented in this P-wave study provides the previously poorly known first order crustal structure of the Rif Mountains in northern Morocco. Crustal interface structure, particularly that of the sedimentary basins and the Moho (Figures 5.7 and 5.11) need to be taken into consideration in any geodynamic model attempting to address the complex tectonic evolution of the Gibraltar Arc System.

The western end of the EW profile, sampling the Gharb Basin, shows a thick sedimentary cover reaching 10 km. At the transition between the External Rif domain and the Gharb Basin the observation of a fast sedimentary layer westward of shot R3, altogether with the significant change in the total sedimentary thickness, is interpreted as being the deep expression of fold-and-thrust belt, which will reach at least depths around 10 km. This is consistent with previous geological results showing the presence of those structures at an analogue area between the Saïss Basin and the External Rif (Bargach et al., 2004; Chalouan et al., 2006). Further east, the sedimentary cover thins in a progressive manner to about 2 km near the point at which the Moho is deepest at ~53 km, increases abruptly to 4 km beneath shot R4 and remain 1-3 km thick up to the Algerian border.

From the western end of the profile, the Moho deepens rather smoothly eastward to model coordinate 145 km, where it thins abruptly from 53 km to less than 30 km by 190 km. That is, it decreases around 23 km in thickness over a distance of 40 km. This large and unexpected variation in crustal thickness takes place under the External Rif domain. Farther east, the crustal thickness between model points 190-330 km remains constant, at ~29 km.

The abrupt change in crustal thickness between 145 and 190 km suggests a tectonic boundary separating two different crustal types, which we attribute to juxtaposition of crustal blocks along the seismically active left-lateral Nekkor strike-slip fault, the

onshore continuation of the TASZ. The low shot density and the obliqueness of the profile across the shear zone limits our ability to resolve vertical features. However, a 2 km step in the sedimentary thickness, passing from 4 km eastward of the fault to 2 km westward, has been documented. The Nekkor fault has been active from the late Miocene (Chalouan et al., 2006) and has been linked to the normal faults beneath the Alhoceima region (Booth-Rea et al., 2012). This region has large seismic activity in the upper crust, but also moderate seismicity at depths reaching 40 km depth (El Moudnib et al., submitted in Tectonophysics 2014), hence suggesting that the Nekkor fault penetrates through the entire crust. The abrupt change in the Moho depth beneath this area depicted by our models strongly supports this hypothesis.

The density model along the EW transect is compatible with the gravity data. Relatively high velocities and densities characterize the root zone. The high  $PmP$  amplitudes under the root suggest that the Moho is a relatively sharp impedance contrast, as smooth transition will result in changes in the critical distance inconsistent with the data. The lower crust velocities in the southernmost part of the profile are around 6.6 km/s, while beneath the Rif they reach values of 6.8 km/s. This suggests an increase in metamorphic grade of the rocks in the root beneath the Rif. At this point it is difficult to assess the increase of this metamorphic degree, as it could be characteristic of the lower crustal rocks of the Rif's crustal domain or it could result from the increased pressures in the crustal root.

Our velocity-depth model evidences a significant mismatch between surface topography and Moho geometry, as the major topographic elevations reaching 1700 meters, are found around shotpoint R4, coinciding not with the crustal root but with the steep thinning Moho ramp. This effect has previously been observed in active orogens as the Carpathians or the Caucasus and can be explained by an elastic effect, even if other hypothesis, as the presence of mantle mechanisms that contribute to sustain present-day topography cannot be discarded.

Along the NS crustal model the Moho shows also relatively large variations in depth. In the Middle Atlas the Moho is constrained from SIMA wide-angle seismic reflection data (Ayarza et al., 2014) and reaches values a little over 40 km depth (Figure 5.11). The low-density lower crust inferred from the seismic model in this area suggests a

mantle contribution to sustain topography. Northward, the Moho shallows to 32 km beneath the northern Meseta and the southern part of the External Rif, then thickens again from model coordinate 140 to 50 km depth at model point 210 km forming the root beneath the northern External Zone of the Rif.

Hence, the most conspicuous structural feature, well constrained from both profiles, is the presence of a 47-53 km thick crust below the External Rif domain, which conforms well to the overall gravity pattern. Moreover, clear lateral variations are observed, particularly a thinning of the crust by ~20 km east of the Nekkor fault. A similar crustal pattern was suggested in recent receiver functions analyses from Topo-Iberia and PICASSO passive seismic surveys (Mancilla et al., 2012; Thurner et al., 2014), as well as in the velocity anomaly variations inferred from local earthquake tomography and ambient noise datasets (El Moudnib et al., submitted in Tectonophysics 2014). GPS observations show that the Rif block is moving S to SW relative to Nubia, with an eastward termination roughly coincident with the Nekkor fault (Kuolali et al., 2011). At the lithospheric scale other datasets such as SKS splitting (Díaz and Gallart, 2014) and surface wave and teleseismic body wave tomography (Bezada et al., 2013; Palomeras et al., 2014) also show first order discontinuities below this area. Our results are not consistent with the Moho depth values of 32-36 km previously estimated from heat flow data (Soto et al., 2008) or from combining elevation, geoid, gravity and petrological constraints (Fullea et al., 2010, 2014).

We emphasized that the Moho depths of ~50 km found below the External Rif domain are significantly greater than those below the Middle or High Atlas and most of the Betic Range (Ayarza et al., 2014; Thurner et al., 2014). This increase in crustal thicknesses is accommodated at middle and lower crust levels, while the upper crust has a homogenous thickness of 12-15 km. Our profiles do not provide enough control to discern between a middle or lower crustal thickening (see Figures 5.5 and 5.9). Another highlight of these profiles is the existence of a fast sedimentary layer beneath shotpoint R3, the fast layer of 4.8 km/s and double thickness of sediments, is likely due to a thrusting, which can be associated to a thrust front and fold axes, similar to what is described by Bargach et al. (2004) and Chalouan et al. (2006) in the Prerif area.

The complex crustal structure of the Rif domains is a consequence of the Miocene collision between the Iberian and Africa plates combined with the westward rollback of the Neo-Tethys slab. The crustal thinning observed east of the Nekkor fault may be associated with the Neo-Tethys passive margin, the result of Mesozoic rifting (Gomez et al., 2000; Tesón, 2009). The crustal thickening under the External Rif can be attributed to slab pull from the downgoing Alboran slab under the Gibraltar Arc System which is imaged in a variety of tomographic images (Spakman and Wortel, 2004; Garcia-Castellanos and Villaseñor, 2011, Bezada et al., 2013; Palomeras et al., 2014). However, these interpretations remain open questions to be developed in further investigations.

# Chapter 6: Mapping the Moho beneath the Rif Cordillera from off-line wide-angle reflections

## 6.1 Introduction

In this chapter, we present complementary results of crustal depth investigations beneath the Rif Cordillera arising from the interpretation of active seismic profiles. Here, we investigate the information provided by the offline time arrivals recorded during the RIFSIS experiment as well as data from the GASSIS WestMed campaign. The latter project (Gracia et al., 2012) focused on the acquisition of multichannel reflection seismic profiles across the Alboran Sea, using air-gun shots every 50 m by the Spanish vessel Sarmiento de Gamboa. Figure 6.1 shows the three profiles considered in this work, labeled Prof. 21, Prof. 19 and Prof. 17. Here we only considered signals from on land stations in Northern Morocco, allowing the investigation mainly of the offshore-onshore transition.

Figure 6.1 compiles, on top of the Bouguer anomaly map, the two wide-angle seismic reflections experiments carried out simultaneously in October 2011, the RIFSIS and the GASSIS-WestMed projects (Gil et al., 2014; Gracia et al., 2012). Observe how the Profiles 21 and 19 are sampling the limits of the lowest Bouguer anomaly (~-150 mGal) to the north and the east, respectively. Profile 21 has a NE-SW orientation, crossing the Beni-Boussera peridotites (~50 mGal) and passing through the Internal and External Zones and the Gharb Basin. Profile 17 was located at the very end of the low Bouguer anomaly, in the boundary between -50 mGal and 0 mGal and, like Profile 19, it crosses the Nekkor fault (Figure 6.1). As previously mentioned, the RIFSIS profiles were deployed following the axes pattern of the low Bouguer anomaly (Figure 5.1).

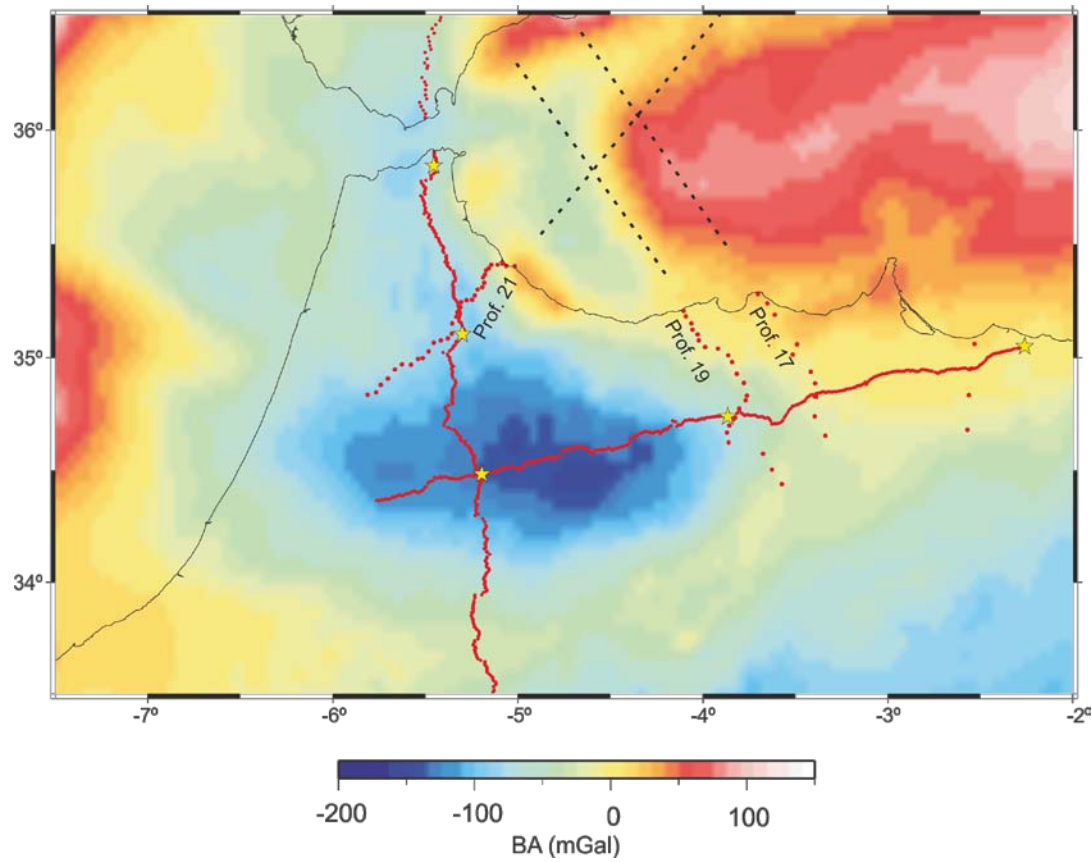
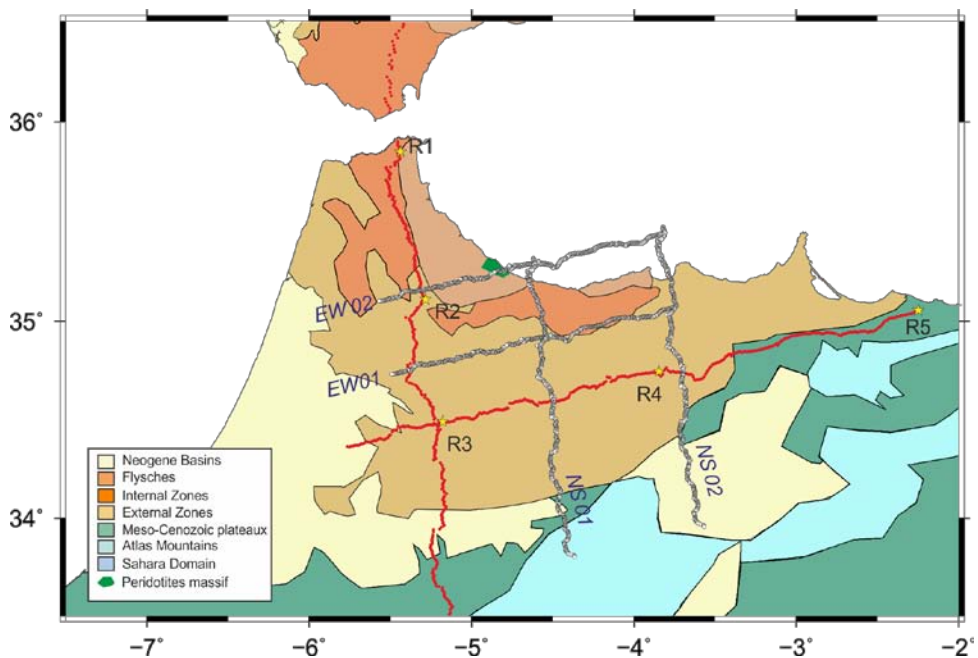


**Figure 6.1:** Bouguer anomaly map with the representation of the geometry of the wide-angle seismic reflection experiments. Shot point locations are indicated by yellow stars. The red dots indicate the location of the seismic recorders, and the black lines show the contributing GASSIS-WestMed offshore profiles labeled as Prof. 21, Prof. 19 and Prof. 17.

## 6.2. Low-fold wide-angle stacks and offline $PmP$ measurements

The deployment logistics during the RIFSIS project allowed that all the stations recorded all shots, not just the shots aligned with the two profiles (see Figure 6.2). Hence, the stations forming the NS profile recorded shots R4 and R5. Similarly, the stations of the EW profile recorded R1 and R2. From these profiles we can obtain a deep crustal image in-between the profile and the shot, as it is represented in Figure 6.2 (white dots). We considered these offline records as pseudo-profiles, and added 01 or 02 to indicate their proximity to the main profile (in Figure 6.2 EW00 strands for the EW wide-angle profile, EW01 for the R2 records, EW02 for the R1 records, and NS00 for the NS wide-angle profile, NS01 for R4 records and EW02 for R5 records). Moreover, all shots R1 to R5 were recorded also in all the stations deployed in land with the main purpose of recording the air-gun shots of marine profiles 17, 19 and 21 (Figure 6.2b), therefore providing additional, shorter length pseudo-profiles.

a)



b)

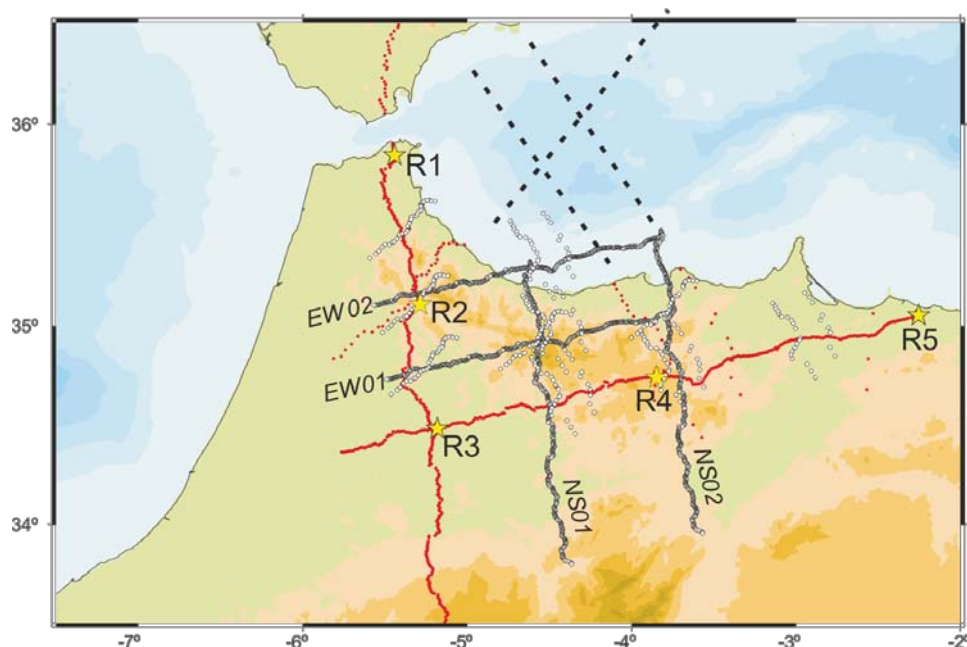


**Figure 6.2:** a) Geometry of the RIFSIS wide-angle seismic reflection experiments overprinting the geologic map. Shot point locations are indicated by yellow stars. Red dots indicate the location of the seismic recorders while white dots indicate the CMP (Common Mid Points) used for the low-fold wide-angle seismic stacks. b) Includes contribution of the R1-R5 recordings at the three land segments deployed to record marine profiles of GASSIS experiment

Here, we will consider firstly a complementary approach to the interpretation of the RIFSIS profiles (see Chapter 5), in terms of multichannel imaging to emphasize the deep reflectivity. The application of a hyperbolic move-out to  $PmP$  phases and the

building up of CMP (Common Mid-Point) images of normal incidence data sets will provide low-fold wide-angle stacks along the two profiles as well as a 2-D approximation to the lateral extent of the Moho in zones outside the wide-angle profiles (Figures 6.3-6.5).

The obtained images provide another view of the increase in crustal thickness beneath the external Rif domain, and document genetic differences in the crust across the different domains (Internal and External Rif domains).

The results arising from the investigation of those offline data will be merged with the models resulting from ray-tracing modeling of the land and the onshore-offshore profiles to provide a global 2-D map of the crustal thickness in northern Morocco.

### 6.2.1 Data processing

As a first approach, conventional seismic processing was considered for all data sets, including the onshore-offshore recordings and the RIFISIS shot-gathers. Several steps have been applied to increase the signal-to-noise ratio (SNR), including band pass frequency filtering, spherical divergence amplitude corrections, spectral whitening (spectral balancing), and amplitude gain (trace balancing). Even if the shot records have relatively large offsets, they have been processed to obtain low-fold wide-angle seismic stacks. Following Carbonell et al. (2002), a hyperbolic time reduction has been applied to the data, resulting in stacks in which the reflections from the Moho are expected to appear as sub-horizontal lines. In Figure 6.3 we present a low-fold stack from the EW wide-angle profile dataset which illustrates the main idea of the event descriptions that will be presented in the following section (6.2.2) for profiles EW01 and NS01. Unfortunately, profiles EW02 and NS02 (see Figure 6.2) are not useful in view of their low resolution, due to the far-offsets of the stations from shots R1 and R5 (Figures 6.4a and 6.5b; respectively), too large to record visible *PmP* phases.

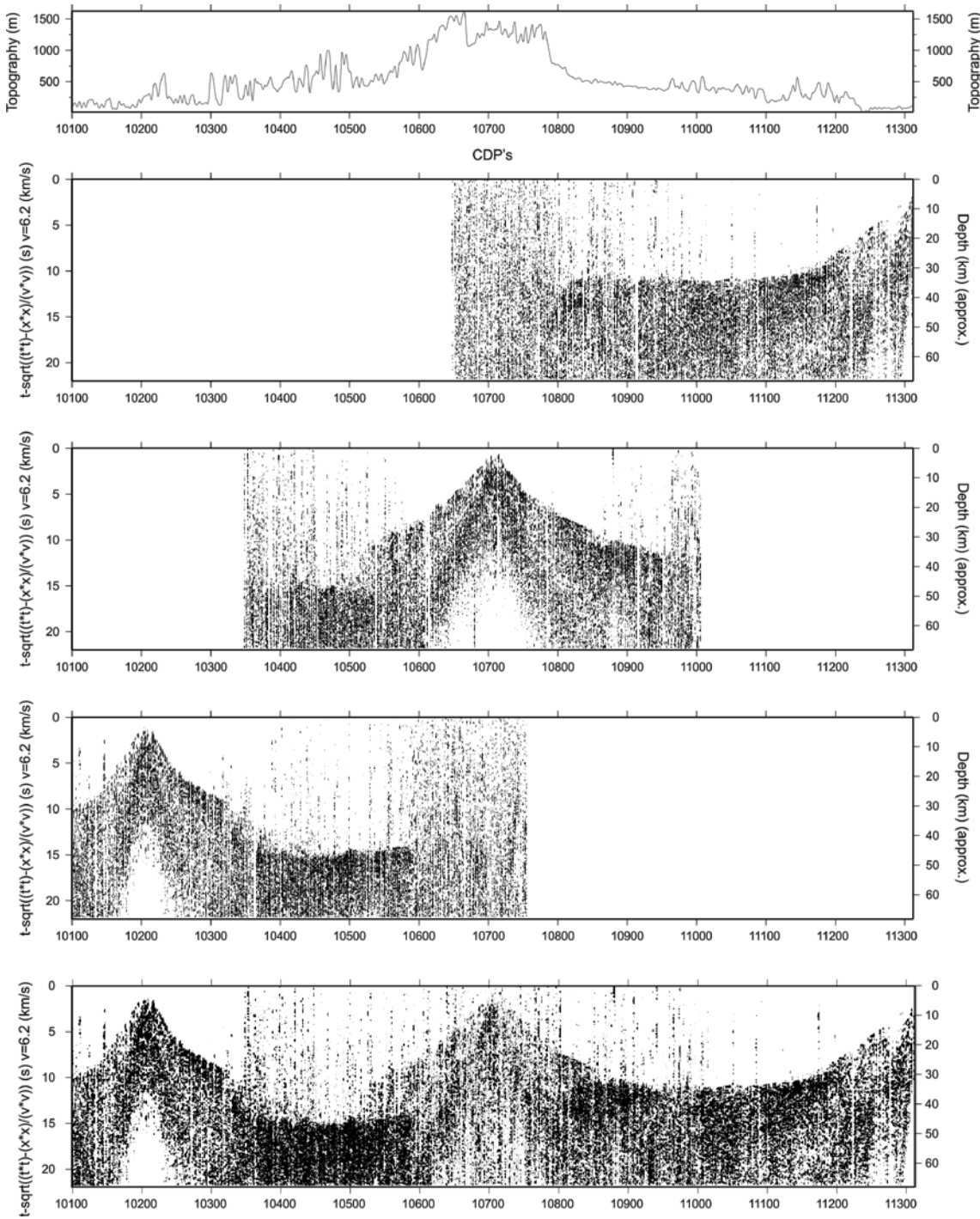


**Figure 6.3:** From top to bottom: topography along the EW profile, shot-gathers R5, R4 and R3 and corresponding stack. The shot-gathers are displayed in the CDP domain after applying a hyperbolic time shift. Data presented using a hyperbolic time reduction  $tr = \left( t - \sqrt{t^2 - x^2/v^2} \right)$  with  $Vp=6.2$  km/s.

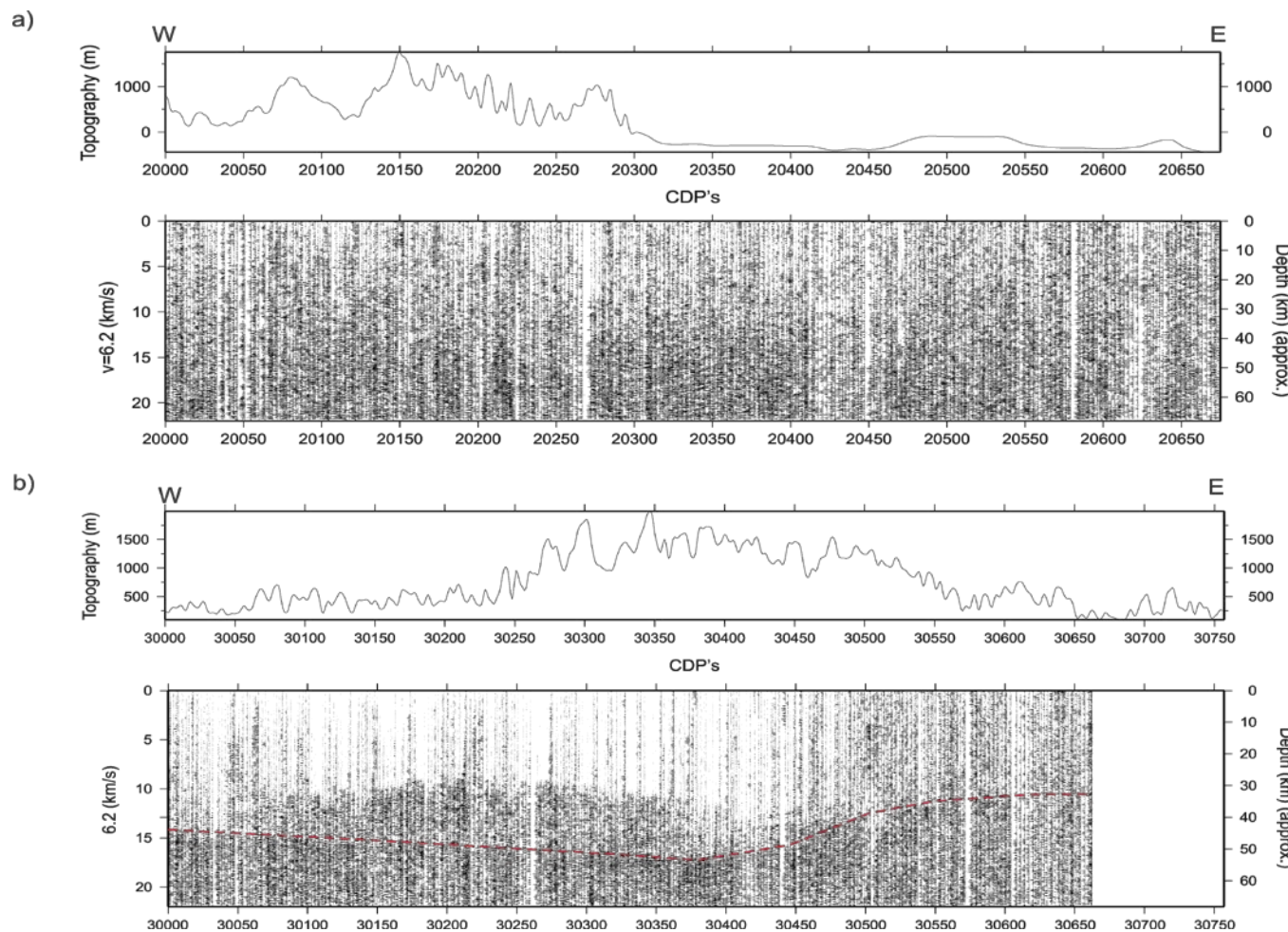


**Figure 6.4:** Low-fold wide-angle stack of the offline shots (a) R1 and (b) R2 recorded along EW profile (called EW02 and EW01 in Figure 6.2). The topography along the low-fold stack profiles is plotted on top of each stack. *PmP* phases are identified on the latter section by red dashed lines.

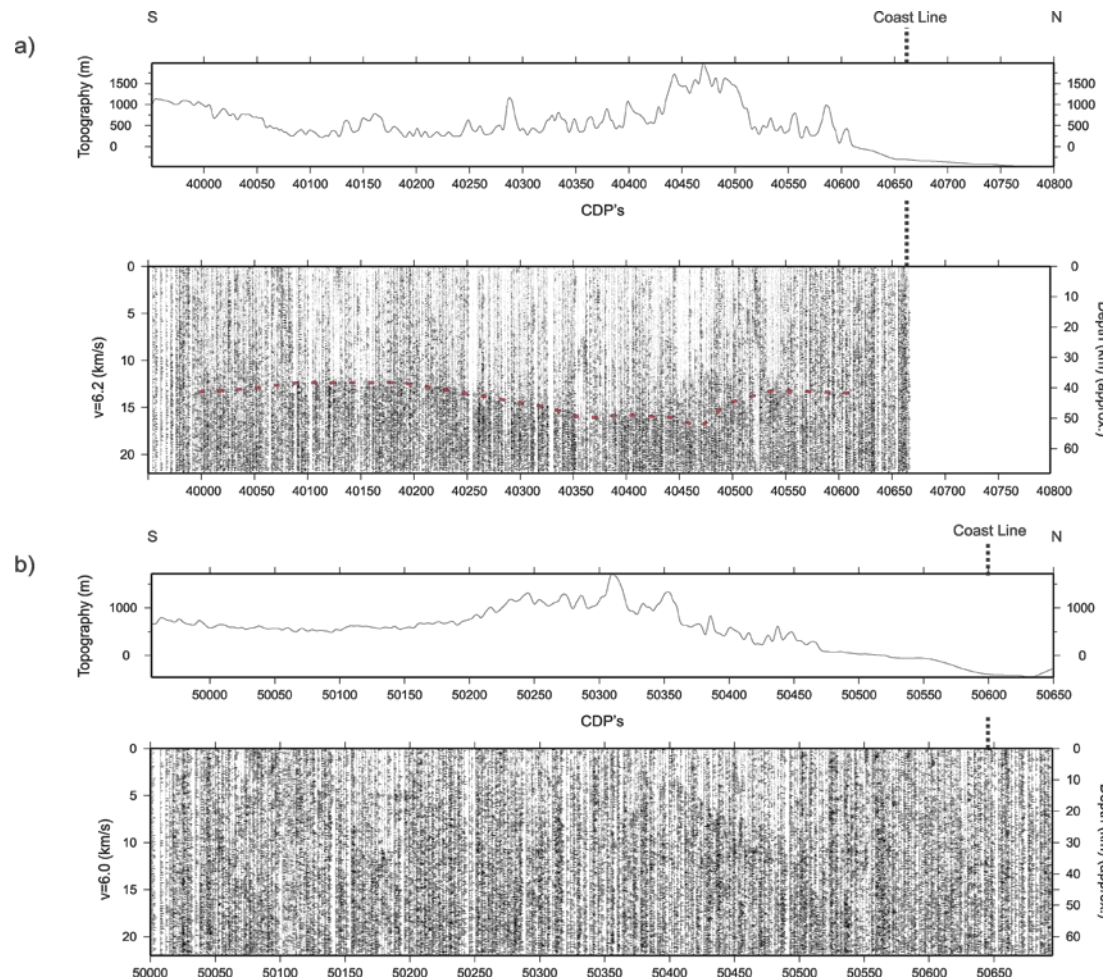


**Figure 6.5:** Low-fold wide-angle stack of the offline shots (a) R4 and (b) R5 recorded along the NS profile (called NS01 and NS02 in Figure 6.2). The topography along the low-fold stack profiles is plotted on top of each stack.  $P_{mP}$  phases are identified on the former section by red dashed lines.

A second, complementary approach arises from the identification and reading of the arrivals corresponding to *PmP* phases in the ‘classical’ offline record sections of the land shots recorded on the RIFSIIS and GASSIS stations deployed. Figures 6.6 and 6.7 illustrate for the latter data the approach followed here. The time-arrivals interpreted to correspond to *PmP* phases are read from the fan record sections. Assuming a uniform crust with a mean velocity of 6.2 km/s, the depth of the reflection point is calculated. This value is then assigned to the midpoint between the shot and the receiver positions (white dots in Figure 6.2). These assumptions imply that large errors can arise in case of heterogeneities, but we will show that this method nonetheless provides significant results in this region. The fan shot gathers may not always display such prominent *PmP* arrivals as the ones observed in the in-line transects. Even so, some relatively high amplitudes corresponding to the *PmP* reflector can be identified and interpreted (see red dashed picks in Figure 6.6).

As mentioned previously, the crust beneath the Alboran Sea was also targeted by the independent GASISS WestMed project coincident in time with the acquisition of the RIFSIIS profiles. An additional logistic effort was made to use some of the seismic instruments for the recording of onshore-offshore profiles using the air-gun source operated by the Sarmiento de Gamboa vessel. Even though this source was not optimized for wide-angle purposes, we were able to obtain valuable record sections allowing a conventional ray tracing analysis. The complexity of the area difficult the detailed interpretation, but preliminary models have been presented by Cembroski (2012) and Cembroski et al. (2013). Here, we have only focused in obtaining the depths attributed to the Moho interface around the onshore-offshore transition of GASSIS profiles 17, 19 and 21 (see location in map Figure 6.1). As a complementary example, we present in Figure 6.7 the wide-angle stack for shot R5 recorded at the inland stations prolonging Profile 17.

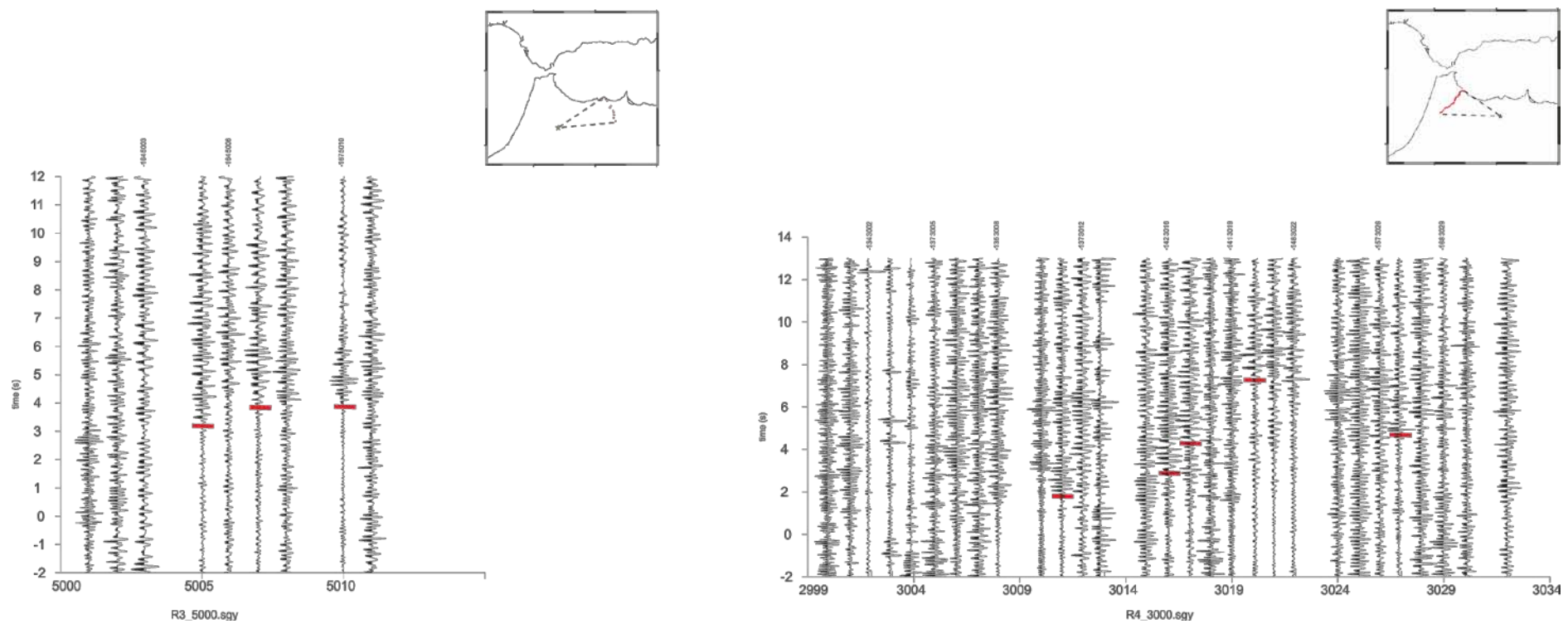


**Figure 6.6:** Examples of  $PmP$  pickings of RIFSI shots recorded on the complementary ‘GASSIS’ profiles. **Left panel:** Shot R3 recorded at line 5000 (Profile 17 stations inland). Distance ranges: 164-167 km. **Right panel:** Shot R4 recorded at line 3000 (Profile 21 onshore stations). Distance ranges: 120-170 km. Times are reduced using  $Vp=6.0$  km/s

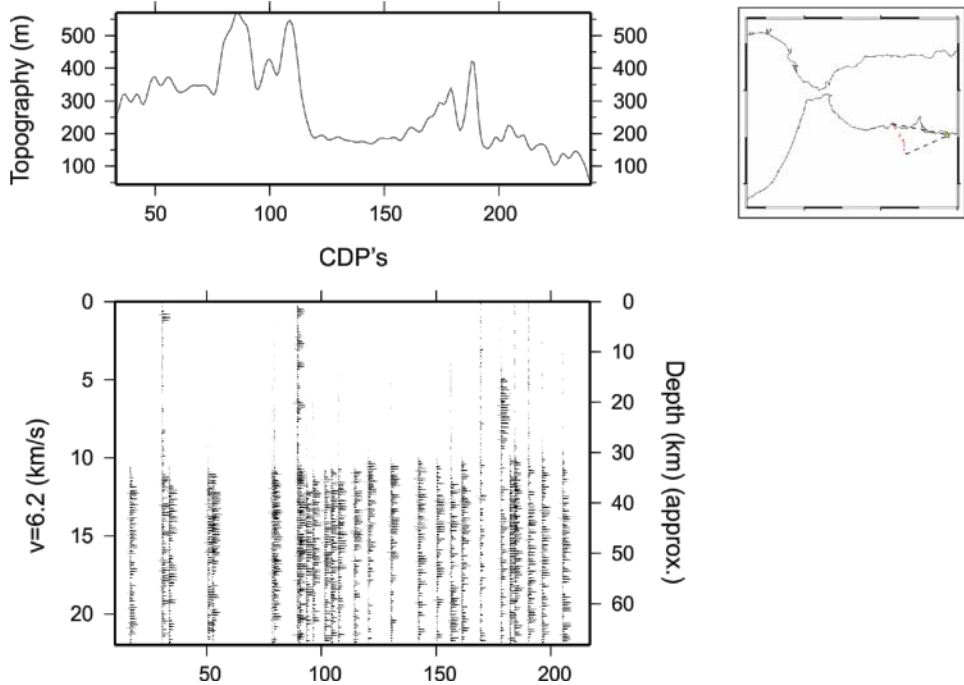


**Figure 6.7:** Example of the low-fold seismic stack of line 5000 that recorded shot R5 on a distance range between 164 and 167 km. On top of the seismic stack is represented the topography along the profile, and at the right the profile and shot locations.

### 6.2.2 Data interpretation

To facilitate the data analysis, we will follow the same organization as in the previous chapter. Therefore, firstly we describe the data from the EW profiles, followed by the profiles with NS orientation. Finally, we will look at the ‘onshore’ profiles, from west to east (Profiles 21, 19, and 17; see Figures 6.1 and 6.2 for locations). In the discussion section we will follow the same organization as in this section.

#### *East-West sections*

In the following we describe the data presented in Figure 6.3. Shot R5 images strong reflectivity in the Moho discontinuity (starting at ~10 s TWTT) between CDPs 10800 and 11200, in contrast with almost no energy visible in the farther part (until CDP 10600). In shot R4 the Moho is imaged as a strong reflector to the west of the shotpoint, at about 15-16 s TWTT, from CDP 10650 to 10350. East of point R4, after CDP 10800, the *PmP* phase is recognized at 10 s TWTT. Finally, shot R3 images strong Moho reflectivity (15 to 13.5 s TWTT) from CDPs 10350 until 10600, then loosing energy rapidly.

From the stacked image in Figure 6.3, we can observe a flat Moho reflector around 45 km depth between shot-points R3 and R4, as reported in Chapter 5 from conventional ray-tracing interpretation. The section between CDPs 10660 to 10800, in the area beneath shot-point R4, does not provide evidence of the Moho, which can be explained by the existence of a steep ramp at Moho level imaged in ray tracing modelling (Chapter 5), an structure which can hardly be solved by the CDP technique that works best for quasi flat reflectors. Eastwards of shot-point R4, after CDP 10800 until shot-point R5, the *PmP* phase is again observed almost flat, varying from 33 km to 30 km along the eastern half of the profile.

Figure 6.4(b) represents the EW01 pseudo-profile, which lays in-between shot-points R3 and R2 (see Figure 6.2). This section evidences large variations in the Moho depth. Its eastern termination depicts a Moho located at around 35 km. Further west, the Moho depth increases progressively until at least 50 km beneath CDP 30375, and then smoothly decreasing throughout the western half of the section, to reach 43 km at its western end. Note that in the western half of this section, a secondary arrival is consistently observed at 10 s TWTT, i.e. around 30 km depth. Taking into account the recording offsets for these stations, ranging from 70 to 135 km, and the phases observed in the record sections along the E-W profile, we interpret these early arrivals as an intra-crustal phase associated with the top of the lower crust (*PcP* phase).

#### *North-South sections*

The stacked image of NS profile that we present directly in Figure 6.8 (only the Moroccan part has been processed) shows continuous Moho reflectivity along most of the section, except in the area below shot-point R2. In the first 100 km from the south (CDPs 100-300) the Moho depth slightly decreases, from ~13 to 11 s TWTT (around 40 to 35 km). Between CDPs 300-650 the reflectivity becomes weaker but still continuous, and the Moho progressively increases from 11 to 15 s TWTT (around 45 km depth). The crustal bottom reflectivity is very weak in the area marked by CDPs 650-850. Farther north, between CDPs 850 to 1100 we observe again medium to weak reflectivity at 14 s TWTT (around 43 km depth)

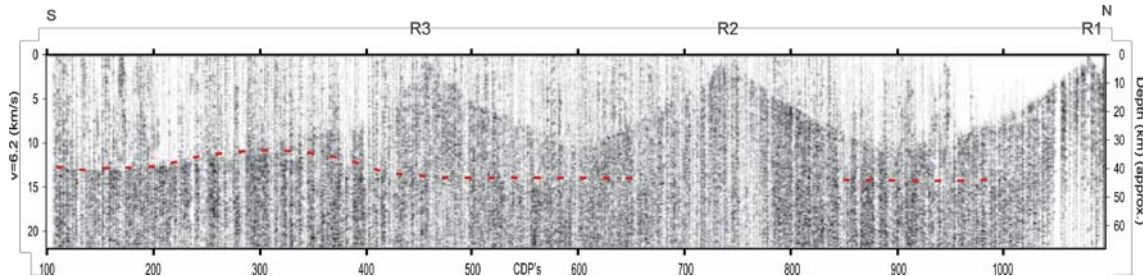


**Figure 6.8:** Low-fold stack image along the NS profile.  $PmP$  phases appear as horizontal lines (red dashed line)

The north-south section constructed from the records along the NS profile of the shot R4 (which is shifted to the east of the line) is shown in Figure 6.5(a). The sample area is depicted in Figure 6.2 as NS01. As in the previous case for the shifted EW02 section (Fig. 6.4b), significant differences in the time arrivals of the  $PmP$  phases can be observed. In the southern part of the section, the arrivals can be interpreted as generated by a Moho located slightly above 40 km. Northward, the Moho position deepens to reach a value exceeding 50 km at the junction with the previously discussed EW01 pseudo-profile. Further north, the signal becomes weaker, but still depicts a crust that thins quickly to reach values not exceeding 35 km. Those large variations are consistent with the ray-tracing models presented in the previous section along the NS and EW RIFSIS profiles (compiled now in Figure 6.9a), which revealed a large Moho step and an area of crustal thickening in both directions, largely coincident with the Bouguer gravity anomaly (Fig. 6.1). The EW RIFSIS profile (Figs. 6.3 and 6.9) shows a thin crust beneath north-east Morocco, with thicknesses close to 30 km which increase further to the west reaching depths around 50 km. The EW01 pseudo-profile presented here is located about 30 km north and shows similar results, taking into account the uncertainties of the method.

#### RIFSIS shots recorded on deployments for GASSIS-WestMed profiles

Data from the  $PmP$  phases along Profile 21 provide clear evidence of a deep Moho beneath the coastline, with depths exceeding 55 km (Figure 6.6a). We observe the  $PmP$  arrivals at 4.5 and 6 s for offsets of 140 and 152 km, respectively. On the contrary, the NW-SE oriented profiles 17 and 19 show a Moho deepening smoothly beneath the coastline to depths of about 17 and 20 km (Figure 6.6b), where we observe the  $PmP$  arrivals at 3-3.5 s for offsets of 164 to 167 km.

All the Moho depth estimations from this second type of approach, based on direct travel-time  $PmP$  pickings, have been integrated into a grid file using a classical “nearest neighbor” gridding algorithm with a small radius to avoid unnecessary extrapolations (Figure 6-9b). Additionally, we have also included in our database the main results derived from an unpublished wide-angle profile from WestMed project (Galve et al., 2007) running north-south at about Melilla-Nador longitude; in this case the Moho dips gently from about 28 km inland to values reaching 18 km below the center of the Alboran Sea.

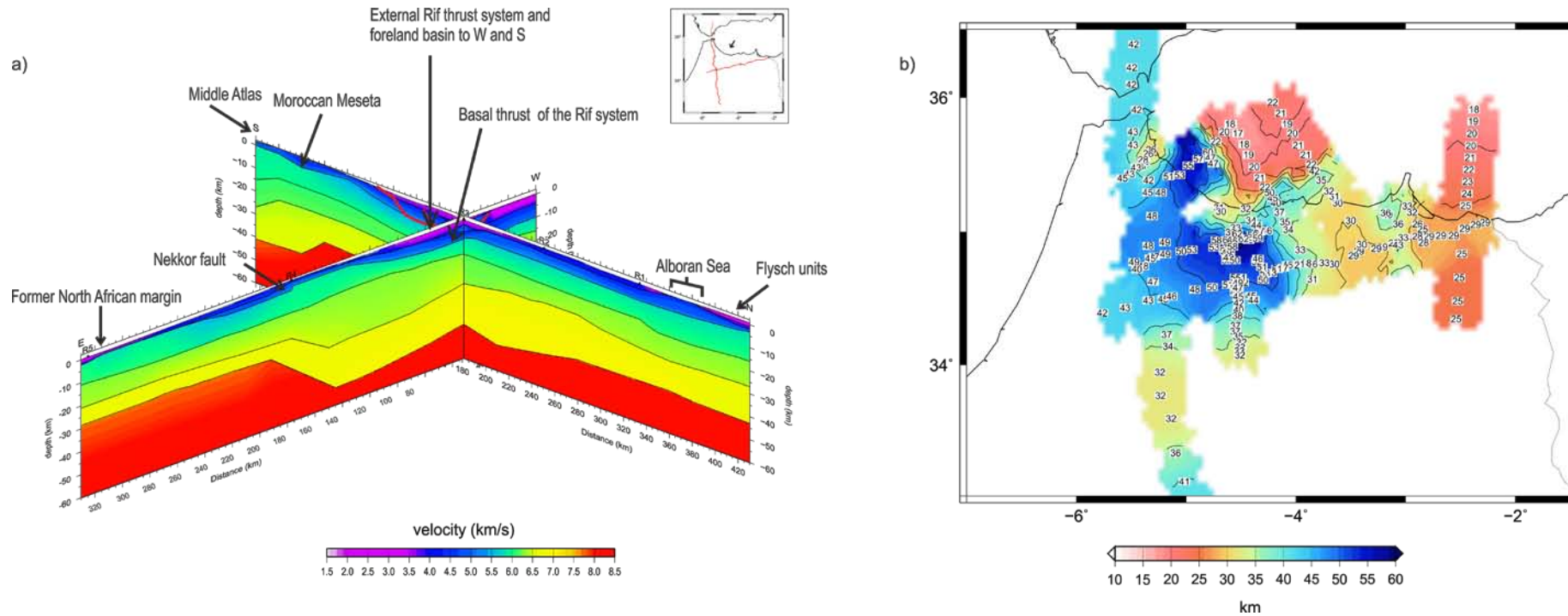


**Figure 6.9:** (a) data from ray-tracing modeling of the main wide-angle profiles, observed from the north-east, presented in the previous chapter and in Gil et al. (2014); and (b) Moho depths inferred from direct  $PmP$  pickings of the different wide-angle datasets. Numbers show Moho depths at the mid-points where a measurement is available. Color grid interpolates between those points using a nearest-neighbor algorithm.

## 6.3 Discussion

The Moho discontinuity is clearly imaged in the shot-gather stacks along the EW profile (Figure 6.3) and the NS profile (Figure 6.8), as well as in the low-fold stack images of pseudo-profiles EW01 and NS01 (Figures 6.4b and 6.5a). In the EW stack section the Moho is imaged with high energy in most areas of the profile, except at the easternmost end and beneath shot-points R3 and R4 where the reflectivity is weaker due to the lower coverage there. A marked change in the reflectivity depth pattern along the EW profile is evidenced, which indicates heterogeneity in the deeper part of the crust and mantle transition (see Figure 6.9a). The Moho discontinuity is observed around 15 s TWTT at the western part of the section (~47 km depth), and thins abruptly to the eastern half, where it is reached at 10 s TWTT. This variation in time arrivals is well compatible with the structure previously constrained by the forward modeling (Figure 6.9 and Figure 5.11 in Chapter 5).

Concerning the pseudo-profiles, section EW01 (Figures 6.4b) shows similar characteristics as the shot-gathers and stack presented in Figure 6.3. Both evidence high energy Moho reflections associated to the Moho. The EW01 pseudo-profile shows that the Moho is thickening from west to east, reaching ~17 s TWTT (around 53 km depth) at CDP 30380 and then abruptly thinning by about 20 km, in less than 50 km lateral distance. The Moho is observed then around 10-12 s TWTT up to the eastern end of the section. Therefore, an interesting, unexpected result arising from the image of this EW pseudo-profile is that the crust appears to be even a few km thicker northwards of main EW profile, in the area between shot-points R3 and R4. Both EW sections show a marked crustal thinning in their eastern part that samples the North African margin. Therefore, the crust eastward of the Nekkor fault zone seems to have a different architecture than the crust below the central external Rif domain. This is supported also by the velocity-depth pattern from ray-tracing modeling presented in Chapter 5 (Figure 6.9a). It is interesting to observe that the area with stronger Moho reflectivity is coincident with the map of absolute shear velocity at 35 km depths presented by Palomeras et al. (2014) and with the crustal discontinuity map generated from receiver functions (Thurner et al., 2014). This area coincides also with the region where the slab is attached to the Rif Cordillera as suggested by recent GPS, teleseismic body-wave and

surface-wave tomographies (Pérouse et al., 2010; Bezada et al., 2013 and Palomeras et al., 2014, respectively).

In the NS stack section (Figure 6.8) the Moho is imaged with high energy at the beginning of the profile (from CDPs 100 to 350) reaching depths of 40 to 35 km below the Middle Atlas and the Moroccan Meseta, respectively. Northward, the Moho deepens and reaches ~46 km, then becoming a flat, weak reflector across almost 100 km below the External Rif domain between shots R3 and R2 (see Figures 6.8 and 6.9). At the northern part of the section the Moho is imaged as a flat reflector of weak reflectivity at ~43 km depth. The differences of reflected energy along the NS profile presented in Figure 6.8 evidence high crustal heterogeneity, which can be understood as the traverse across three different domains (from south to north: the Middle Atlas, Moroccan Meseta and the Rif domains). Nevertheless, the EW profile (Figure 6.3), where it crosses the Rif domain, does not present these changes in reflectivity patterns, while across the North African Margin, we observe a decrease in signal amplitude.

The Moho reflectivity imaged by the NS01 pseudo-profile (Figure 6.5a) is stronger and more continuous than in the main NS section (Figure 6.8), although the observed Moho geometry is similar in both cases. In the stacked image presented in Figure 6.5(a), the Moho reaches 43-44 km depths along the first 250 CDPs, from this point it then deepens by around 10 km, reaching 50 km depths between CDPs 40350 and 40450. A rather abrupt thinning is observed further north, where Moho reaches 40 km depth. As mentioned before, one of the interesting features of the NS and NS01 profiles (Figures 6.8 and 6.5a, respectively) is the marked difference in Moho reflectivity between them. In Figure 6.5(a) the Moho is as a strong reflector between the 40100 to 40450 CDPs, while along the stacked profile presented in Figure 6.8 it is only strong at the southernmost part of the profile (the first 250 CDPs), then becomes much weaker. Taking into account that both sections are sampling similar geological domains, the reflectivity differences evidenced should be attributed either to differences in the efficiency of energy propagation at the vicinity of the shot-points, or to crustal differences in seismic attenuation along travel paths mainly in the NS or in the EW directions (or a combination of both effects). Investigation of crustal attenuation properties is out of the scope of this PhD work, but could be a relevant target for future studies.

The complementary data obtained from the GASSIS-WestMed stations, show a flat crust around 30 km deep in the eastern part of our study area (Figure 6.7), similar to the depths inferred from the *PmP* arrivals, observed at around 3-4s reduced time in the record section of this fan-like profile (Figure 6.6a). These results suggest that the crustal thickness to the east of the Rif domain limit (Nekkor fault) is almost flat and does not reach thicknesses more than 30 km. In contrast, the fan-like section from shot R4 recorded along Profile 21 (or line 3000; Figure 6.6b) shows remarkable strong variations in the *PmP* arrival times, hence in crustal thickness. *PmP* arrivals are identified at about 2 s reduced times in station n° 3011, at 135 km offset from shot-point, then travel times increase even though offsets also increase (3 to 4 s at 135-140 km offsets), reaching farther north (stations n° 3020-3022) unusual values of 7 s at about 145 km offset. This corresponds to crustal depths of 50-55 km at midpoints located right beneath the shoreline, in the area where Beni-Bousera peridotites outcrop, and even reaching 10-15 km offshore. Additional constraints from the onshore-offshore recordings (Cembrowski et al., 2013) show that farther offshore in the Alboran Sea, a thin crust of 18-20 km depth is present. Hence, the combination of different wide-angle data sets available suggest a complex crustal architecture in this area, with a Moho thickening seawards and probably under-crusting the Alboran Sea crust.

The Moho map resulting from the 2-D analysis of *PmP* phases is presented at Figure 6.9(b). It allows identifying the geometry of the crustal root, which is not limited to the central Rif zone, as determined in Chapter 5 (Figure 6.9a), but extends northwards until the coastline in a limited region. Observe that the crustal thicknesses below Beni-Boussera are around 50-55 km depth (Figure 6.9), while in the Bouguer anomaly map they are associated to 20-25 mGal (Figure 6.1). These deep Moho values are similar to those inferred below the Central part of the external Rif domain, about 60-70 km to the SE of Beni-Boussera. However, if we observe the Bouguer anomaly map (Figure 6.1), the Central Rif domain has a low Bouguer anomaly assigned (~-150 mGal); which is significantly lower than the one observed in the northeastern coast, near the peridotites (Figures 6.1 and 6.2). This low value of the anomaly observed is most probably due to the shallow location of peridotitic bodies, not deeper than 10 km (Chalouan et al., 2008; Azdimousa et al., 2013; Romagny et al., 2014). Moreover, the Ronda peridotites, which are located on the southern east Iberian coast, are identified by

a Bouguer anomaly of 80-100 mGal (see Figure 6.1; Torne et al., 1992). However, both are arranged on top of the Sebtides and Malaguides zones, respectively (see Vergés and Fernández, 2012). We might assume that the difference in the Bouguer anomaly is associated with the geometry of the mineral deposits (Précigout et al., 2013; Romagny et al., 2014). That is, Ronda signature may reach between 85 and 140 km depths (Vergés and Fernández, 2012), while the Beni-Boussera one may be limited to around 10 km depth (Azdimousa et al., 2013; Romagny et al., 2014). In contrast, if we look at the recent teleseismic body-wave and surface-wave tomographic models, both reproduce the shape of a slab connected beneath the Rif and Betics ranges (Bezada et al., 2013; Palomeras et al., 2014). On the other hand, our results are compatible with the lateral tear slab first described by Spakman and Wortel (2004) (see Vergés and Fernández, 2012; van Hinsbergen et al., 2014). We suggest that the rather low Bouguer anomaly in the Beni-Boussera peridotites may be the result of the combined effects of the small dimensions of the peridotites and their shallow location (Romagny et al., 2014), together with the presence of a rather thick crust beneath them (around 55 km; Figures 6.1 and 6.9b).

The results presented here, derived from 2-D analysis of wide-angle surveys, also confirm the progressive thinning to the east already described (Chapter 5) and the previous RF results from Mancilla et al. (2012) and Thurner et al. (2014). The difference between the Moho-depth map presented here and the one previously presented by Mancilla et al. (2012), is that in the latter the thicker crust is limited to the central part of the external Rif domain, while our data suggest that the thickest crust encompasses a larger area in Rif domains. Our Moho map seems more compatible with the images presented by Thurner et al. (2014), even if our crustal thicknesses are larger than the Moho depths they suggest.

Moreover, our Moho-depth map seems to agree with geodynamical models of the Gibraltar Arc presented by Bezada et al. (2013) and Spakman and Wortel (2004). Both explain that the length of the slab is consistent with the Africa-Iberian plate convergence history. The recent tectonic reconstruction from van Hinsbergen et al. (2014) also suggests that the slab rollback in the western Mediterranean was affected by the Africa-Iberia convergences, causing a contractional deformation farther to the west, as shown in the Chertova et al. (2014) 3-dimensional models. Consequently, in the

Moho-depth mapping presented here, we consider the crustal signature as the consequence of the Miocene collision between the Iberian and Africa plates combined with the westward rollback of the Neo-Tethys slab (Vergés and Fernández, 2012; Chertova et al., 2014; van Hinsbergen et al., 2014). We associate the crustal thinning observed eastward of the Nekkor fault to the Neo-Tethys passive margin (see Figure 6.9), as a consequence of Mesozoic rifting (Gomez et al., 2000; Tesón, 2009).

# Chapter 7: Moho-depth constraints from receiver functions (Topo-Iberia and Picasso networks)

## 7.1 Introduction

In order to infer additional constraints on the crustal thickness knowledge of northern Morocco we decided to investigate this issue using a completely independent dataset and methodology. We based our work in the well-known receiver function (RF) method for the analysis of teleseismic seismicity. We profit from the data gathered by the Topo-Iberia and PICASSO ([iberarray.ictja.csic.es](http://iberarray.ictja.csic.es), [www.iris.edu/PICASSOproject](http://www.iris.edu/PICASSOproject)), two large-scale multidisciplinary research initiatives to investigate Earth's structure and dynamics in Spain and northern Morocco carried on during the last years. As part of the Topo-Iberia project, 20 stations were deployed over northern Morocco forming a regular, 60x60 km spaced grid. In the framework of PICASSO projects over 40 broadband stations were deployed, most of them along N-S profile reaching the Sahara Craton. Around 25 of those PICASSO stations were installed in Rif domains and NE Morocco. Additionally, 13 of the TopoIberia stations were redeployed over northern Morocco in late 2013, supported by the RIFSIIS project, to densify the zones where anomalous features were suspected from the so-far available results.

Even if previous works dealing with receiver functions (RF) on this area have already been published, we benefit here from a more extended database. Most of the TopoI-beria stations have been active till 2013 and hence provided additional data to those analyzed in the Mancilla et al. (2010) paper. Thurner et al. (2014) presented their results in terms of migrated record sections, but did not analyze the crustal depth beneath each particular station. Additionally, the Topo-Iberia stations redeployed over northern Morocco have not been analyzed so far. Although the number of valid measurements is limited due to the short time deployment (about 6 months), their results allow to better constrain the final image.

The good regional coverage and fairly dense station spacing (~60 km for Topo-Iberia stations, and ~30 km for Picasso stations) permits interpolating single station measurements into a continuous map of crustal thickness for the entire study area. The compilation of all the available data has greatly improved the Moho depth estimations

based on teleseismic data over the area, allowing their comparison with analogous results arising from wide-angle profiling previously discussed in this thesis.

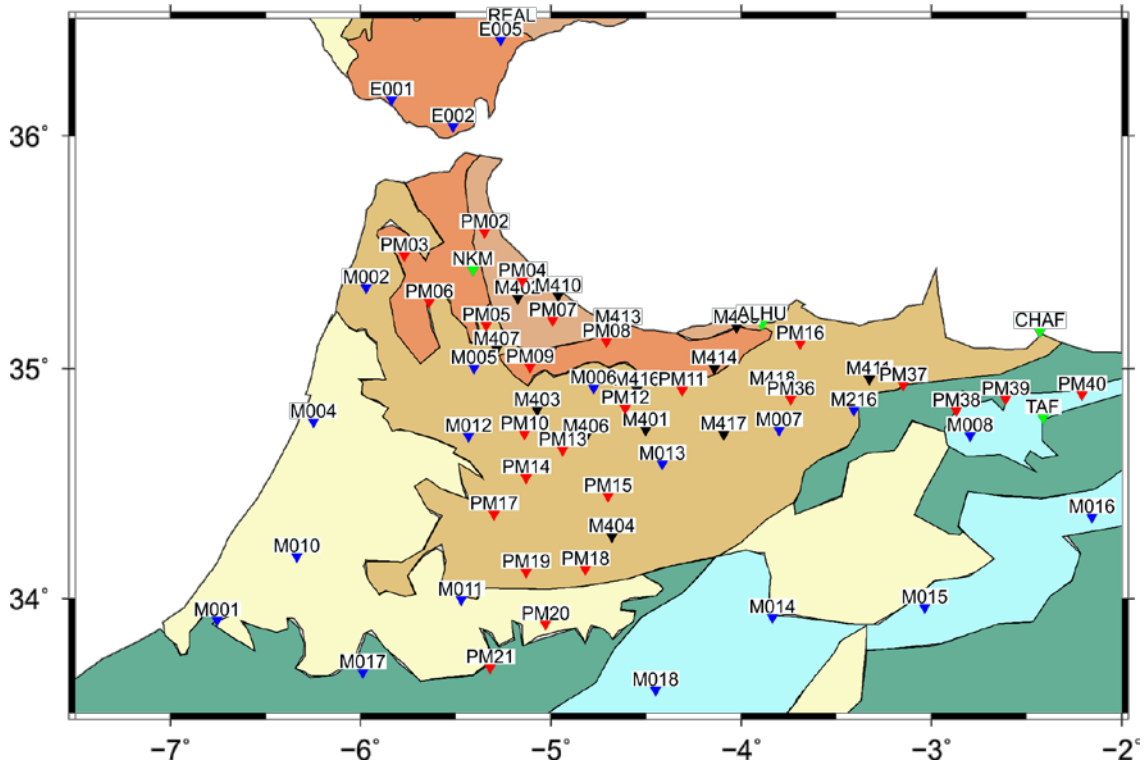


**Figure 7.1:** Geologic map of northern Morocco, including the different stations analyzed here; the triangle colors: blue for the original Topo-Iberia stations; black for redeployed Topo-Iberia stations; red for Picasso stations; green for permanent stations.

## 7.2 Data selection and processing

We analyze waveforms from seismic events that were selected based on standard criteria: (1) teleseismic events with magnitudes higher than 5.5 (2) epicentral distances between  $30^\circ$  and  $90^\circ$  (Figure 7.2) to avoid wavefield complexities that likely arise from upper mantle discontinuities or diffraction at the core-mantle boundary, and (3) high signal-to-noise ratio (SNR) allowing identifying clear P arrivals.

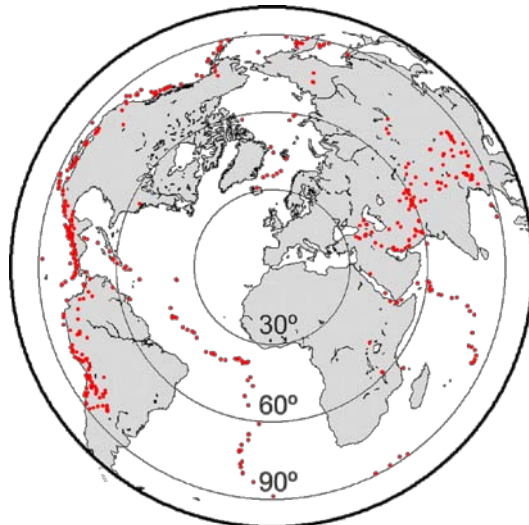


**Figure 7.2:** Location of teleseismic events used in the study (red dots). Note the good azimuthal coverage.

We have taken into account the already published results for the stations already investigated by Mancilla et al., (2010) that have shown evidences of structural complexity, which have been reanalyzed, considering additional data when available. All the Picasso and the 13 redeployed Topo-Iberia stations have been analyzed from scratch. The number of retained RF for each of the investigated stations ranges between 50-60 RFs for the originally deployed Topo-Iberia sites and 7-26 RFs for the redeployed sites, which provide approximately 6 months of data. The PICASSO sites typically provide an intermediate number of retained RFs, ranging between 15 and 41.

We have used H- $\kappa$  analysis (Zhu and Kanamori, 2000, see Chapter 3.3) to infer an estimation of crustal depth (see Chapter 3.3). Figures 7.3, 7.4 and 7.5 present the H- $\kappa$  analysis for some representative stations. The left panels show the variation of the estimator function in the H-K space, with reddish colors depicting the highest correlation values and hence the best solution (see Chapter 3.3 for further details). Right panels show the radial and transverse components of the RFs sorted by back azimuth and corrected by Ps-moveout. The upper panels show the summation of all the retained RFs after the application of the moveout correction. This correction aims at equalizing differences in ray parameters in the phase arrival times to allow for direct comparison of receiver functions for earthquakes from different distances.

This method is known to have limitations in the presence of a dipping conversor, a gradient-type boundary or in presence of sedimentary environments (e.g. Julià et al. 2003; Lombardi et al. 2008). In those cases, the lack of clear multiples of the Ps results in several local maxima appearing in the grid search (e.g. PM19, Figure 7.4c) or in unrealistic  $Vp/Vs$  values (e.g. over 1.83 or less than 1.67). For the limited number of stations presenting this problem, we have estimated the crustal thickness by picking the arrival time of the Ps converted phase in the stacked RF and then converting the delay time to depth using an a-priori  $Vp/Vs$  ratio consistent with that derived for other stations in the same domain. Additionally a few number of stations have provided complex results including two close conversors. On those cases, the general rule has been to interpret the deeper conversor as the Moho, even if each case has been analyzed in detail. Table 1 summarizes the crustal depth inferred for each station.

Figure 7.3 to 7.5 present some representative examples of the HK analysis. PM09 is a good example of the HK results for stations located in the central part of the Rif domains, illustrating the thick crust observed under this region. Figure 7.3 (a) show a well-defined maximum located at a depth of 45 km and a  $Vp/Vs$  of 1.74. The individual and the stacked RFs show a clear conversor at 5.6 s, consistent with the inferred crustal thickness. As it will be discussed later, this thickened crust is consistent with the results derived from active seismic. PM15, still located in the Rif external domain but 90 km further SE, shows a slightly more problematic result (Figure 7.3b). It can be observed that the H-K estimator displays some local maxima, even if one of them is clearly stronger than the rest. The preferred result corresponds to a 48 km thick crust and a  $Vp/Vs$  value of 1.76 and corresponds with the peak observed at 5.9 s in the stacked RF.

The progressive thinning of the crustal thickness to the east is illustrated in Figure 7.4. Station PM36, located westwards of the Nekkor Fault, shows a well-defined peak at 35 km depth. Station PM39, close to the Algerian border, shows also a clear maximum in the grid search, but the crustal thickness is of only 26 km. These results are consistent with those presented by Mancilla et al. (2012).

PM19 (Figure 7.4c) provides an example of a more complex case, for which two prominent maxima at 25 km and 35 km depths can be identified. The observation of the individual and stacked RFs shows that the most consistent peak appears at 4.5 s, hence

corresponding to the second maximum in the HK analysis. This conversor is interpreted as the Moho, while the conversor at 25 km is interpreted to correspond to an intra-crustal discontinuity.

PM20 (Figure 7.4d) located in the southern part of the investigated area, not far from the Middle Atlas, shows again a clear result, with the Moho conversor located at 30 km. This marks the southern termination of the thickened crust.

Even if only few months of data are available, the Topo-Iberia stations redeployed over the Rif domain allow to infer some valuable results. As an example, Figure 7.5 shows the analysis of two of these stations. M418, located close to the Nekkor Fault area, shows a clear maximum in the grid search, resulting in a crustal thickness of 30 km. On the contrary, M416, located in the Rif Domain, shows a more complex image. The stacked RF shows two maxima at 4.25 and 6.4 s, corresponding to depths of approximately 34 and 54 km. In this case, the decision on which of them is related to the Moho is unclear. Finally, we have identified the Moho with the first conversor because it seems to be more consistent along the different backazimuths.

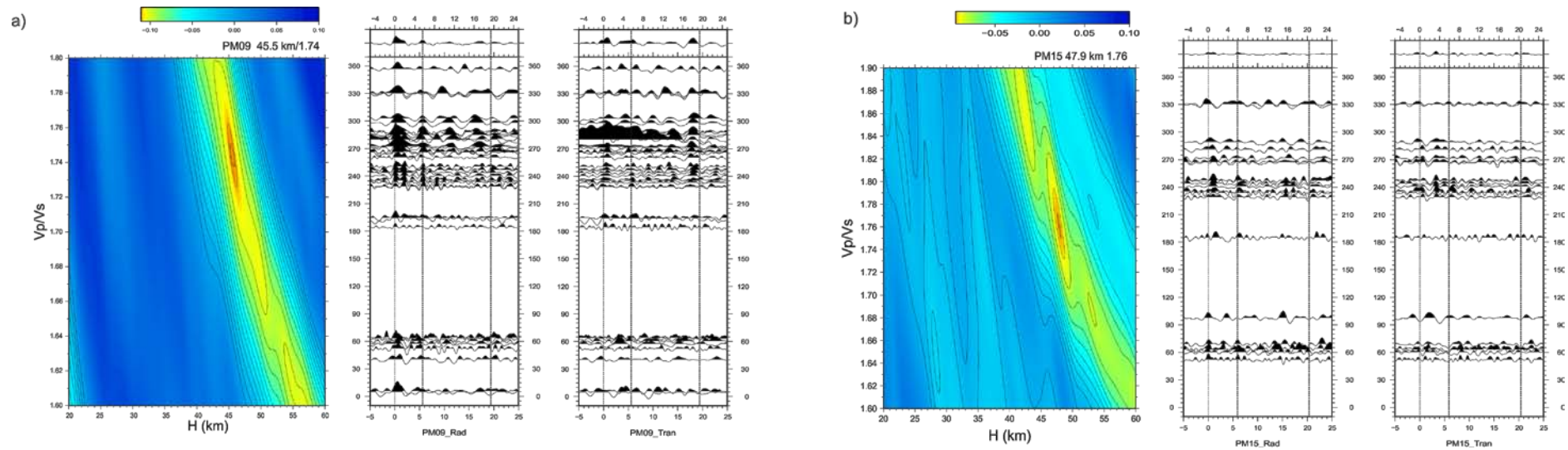


**Figure 7.3:** H-k analysis for the stations located in the Flysch domain, near the internal Rif domain (a) and the external Rif domain (b). The thick back ellipse denotes the estimated uncertainty in the definition of the Moho. The right part of each panel shows the radial and transverse components, respectively, corrected for Ps-moveout and stacked into bins of 10° of back azimuth. The dashed lines correspond to the direct P arrival followed by the converted phase (Ps) and the multiples (PsPs+PpSs). On top of each panel are shown the radial and transverse stacked RFs.

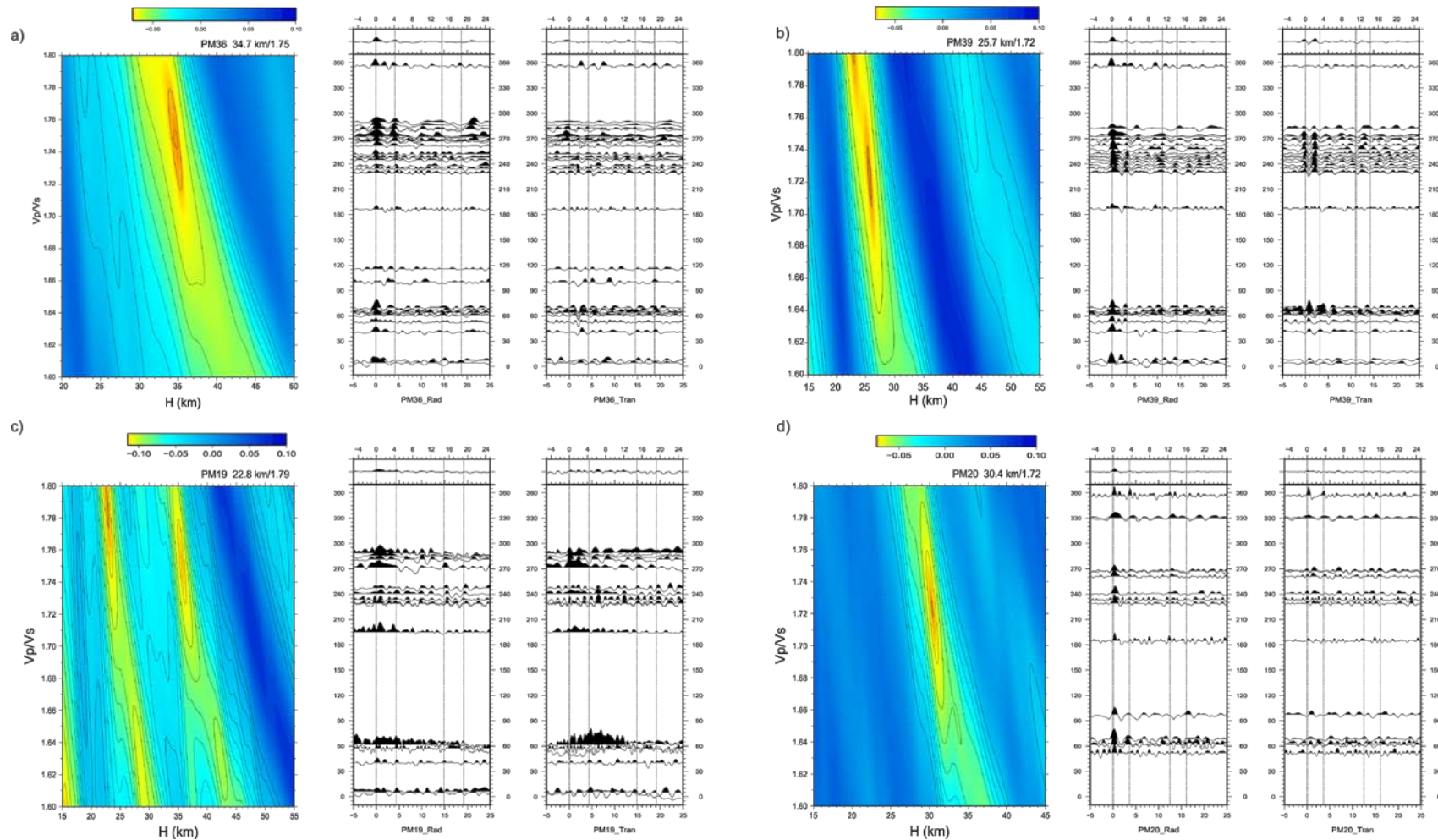


**Figure 7.4:** H-k analysis for the stations located eastward of Nekkor fault (**a, b**), the southernmost part of the Rif Doman (**c**) and in the Gharb Basin (**d**)

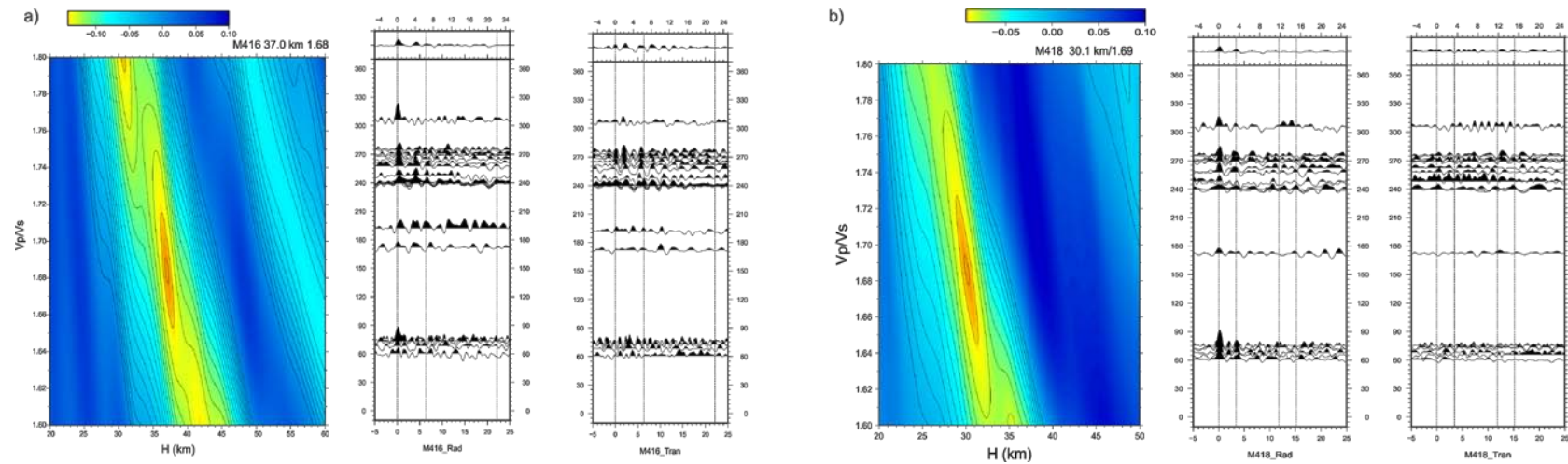


**Figure 7.5:** H-k analysis for the stations located westward (a) and eastward of Nekkor fault (b).

**Table 1:** Summary of results obtained by H-κ analysis and Ps arrival time for each station

STATION	H <sup>zhu</sup>	Vp/Vs <sup>zhu</sup>	T <sub>Ps</sub>	H <sup>Ps</sup>
M002	37.9	1.69		
M005	42.0	1.75f		
M006	53	1.75f		
M007	42.5	1.70		
M008	20.0	1.62		
M012	41.2	1.79		
M013	55.0	1.75f		
M401	41.0	1.75f		
M402	46.0	1.80		
M403	-	-	6.1	50.2
M406	43.2	1.75		
M407	37.5	1.75f		
M408	26.0	1.75f		
M410	48.5	1.75f		
M411	28.5	1.73		
M413	38.0	1.75f		
M414	30.0	1.82		
M416	52.0	1.75f		
M417	-	-	4.8	39.5
M418	30.1	1.69		
PM02	38.5	1.75f		
PM03	43.4	1.72		
PM04	41.5	1.75f		
PM07	44.0	1.77		
PM09	45.5	1.74		
PM10	46.3	1.71		
PM11	34.0	1.82		
PM12	46.2	1.72		
PM13	-	-	6.5	53.5
PM14	54.0	1.75f		
PM15	48.0	1.76		
PM16	28.5	1.75f		
PM17	42.9	1.75		
PM18	-	-	4.5	37.0
PM19	35.0	1.75f		
PM20	30.4	1.72		
PM36	34.7	1.75		
PM37	25.7	1.75		
PM38	24.6	1.82		
PM39	25.7	1.72		
PM40	21.8	1.81		

## 7.3 Crustal thickness map

Once a value of crustal thickness and Vp/Vs has been assigned to each station, a grid can be interpolated using a similar approach to that for active seismic data (See Chapter 6). Figure 7.6 allows comparing the results derived from our contribution (left panel) and those published by Mancilla et al. (2012). Both images have been calculated using the same method but different stations and teleseismic events. Even if some local differences do appear, there is an overall similarity between them, confirming the robustness of the results. The more relevant of those differences is located south of Alhoceima, where Mancilla et al. (2012) gave a thickness of 26 km beneath station M007. After reprocessing data from this station, which provide complex RFs, we favor an alternative interpretation fixing the crustal depth at 42 km. The large difference between both interpretations is in fact linked to the peak interpreted as generated by a conversion in the Moho. Station PM36, located few kilometers north, give a crustal thickness of 35 km, arguing in favor of our reinterpretation. Nevertheless, this discrepancy is only relevant for the precise mapping of the eastward crustal thinning, but does not change the global image derived from those results. In a next step, both data sets have been merged together, thus providing a crustal thickness map of the region derived from passive seismic data (Figure 7.7a). This map is compared to the one derived in the previous chapter from active seismic (Figure 7.7b). Both maps are remarkably similar, taking into consideration that they come from completely independent data sets and methodologies. Finally, results from WA and RFs are gathered to obtain the final crustal thickness map of north Morocco (Figure 7.8). The main feature is the large crustal root observed beneath the central Rif Domain, which reaches, at least, 50 km. This root is in good agreement with the area presenting large negative Bouguer anomaly values (refer to Figure 6.1 in Chapter 6). Active seismic data seem to extend this root until the coastline in a limited region close to 5° W, nearby to the Beni-Boussera peridotites. RF results are not able to discern clearly this feature, but the newly deployed M410 station gives also a crustal depth of 48 km, consistent with the WA results. Different authors have proposed that the Alboran slab may still be attached to the lithosphere beneath this area (Pérouse et al., 2010; Bezada et al., 2013; Levander et al., 2014; Palomeras et al., 2014; Thurner et al., 2014). The crustal root delineated by our results may be the result of this process, thus confirming the hypothesis (see Figure 7.8).

To complete the seismic exploration of the Rif Domain, at Figure 7.9 we overlaid our final crustal thickness map with the hypocentral distribution during the period 2000-2014, as reported in the IGN catalogue. An extended discussion on the seismicity pattern of this area is beyond the objectives of this work, but the main points are the presence of a well defined, N-S oriented, alignment of deep seismicity in the westernmost Alboran sea (approx.  $4.6^{\circ}$  W) and a large amount of superficial seismicity distributed around the Alhoceima region ( $4^{\circ}$  W,  $36^{\circ}$  N approx.) and south of Nador ( $3^{\circ}$  W,  $36^{\circ}$  N). To the West an arcuate alignment of seismicity, including both superficial and deep events can be defined from about  $5.5^{\circ}$  W,  $34.5^{\circ}$  N to  $7^{\circ}$  W,  $35.5^{\circ}$  N. The origin of this seismicity remains unclear, even if its location can now be resolved correctly, the installation of several permanent stations in Morocco. It is worthy to note that the zone with thickened crust corresponds to the area in between the seismically active regions. Few events have been located so far inside the region defined by the 40km depth isoline. The relationship between the crustal thickening, the seismic gap and the presence of an attached slab is still an open issue to be explored in the next future.

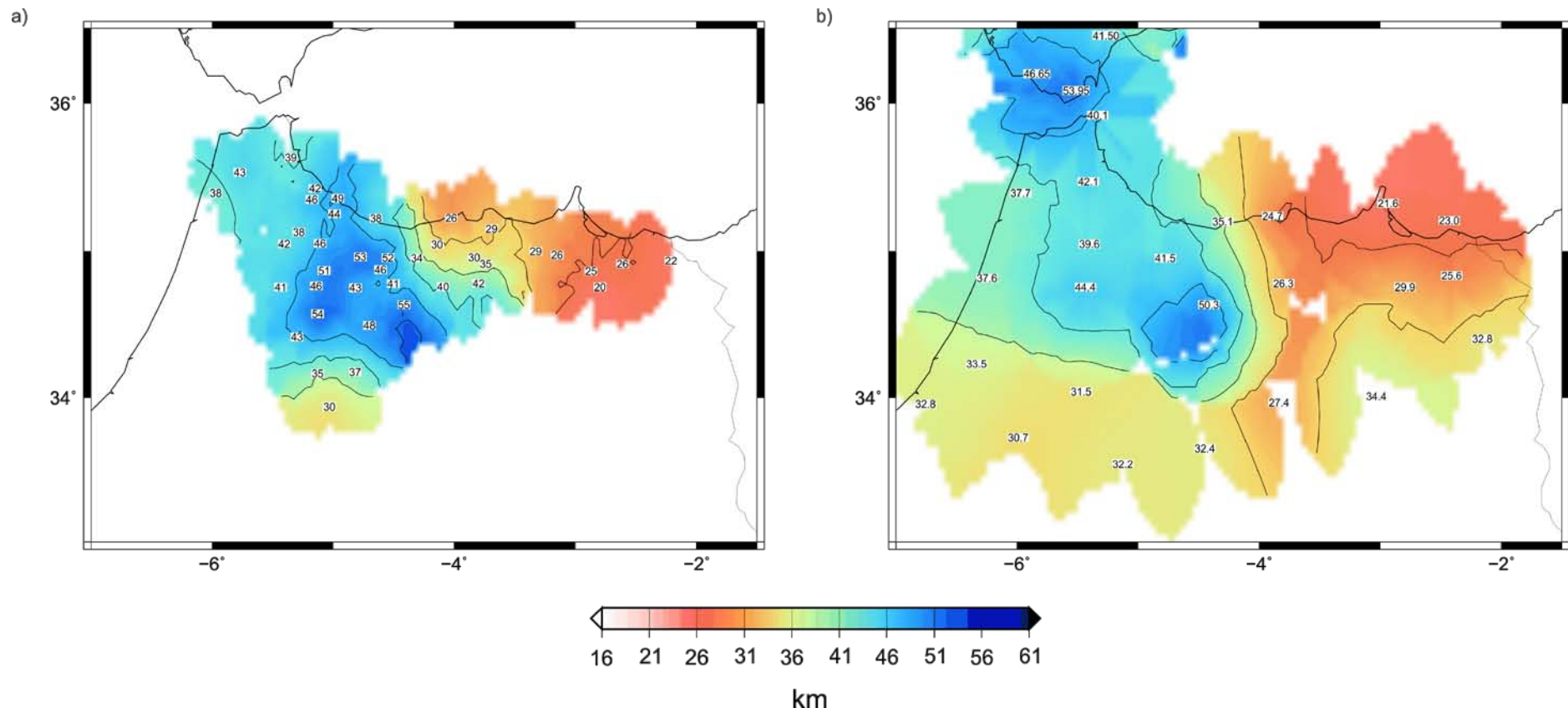


**Figure 7.6:** Moho depth contour map inferred from RF analysis beneath Northern Morocco, by the RFs (a) analyzed in this chapter (b) and the ones provided by Mancilla et al. (2012). Large variations, strong gradients, and a division into different domains are observed. Numbers show the sites for which a measurement is available. Color grid interpolated using a nearest-neighbor algorithm.

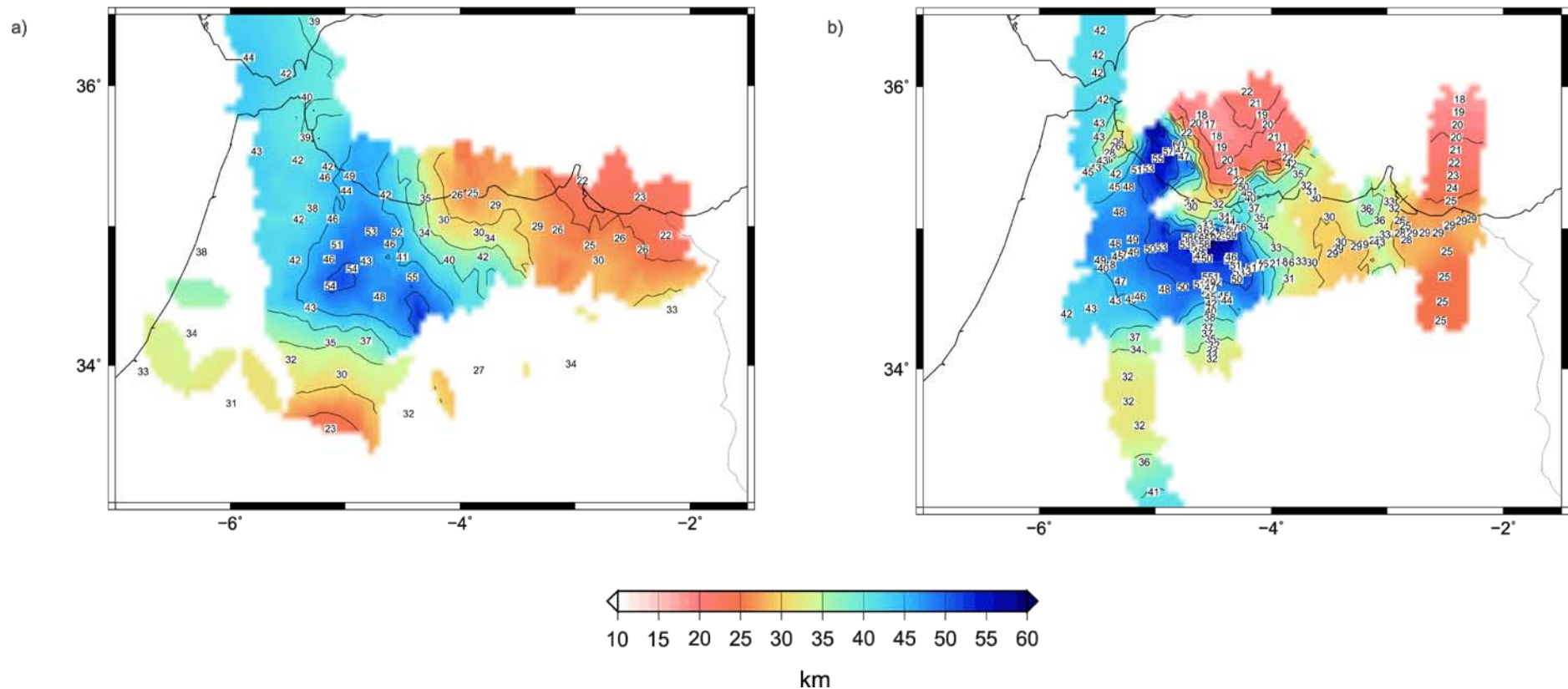


**Figure 7.7:** Moho depths inferred from wide-angle experiments (a) and RFs analysis (b) beneath Northern Morocco. Numbers show the points for which a measurement is available. Color grid interpolated using a classical nearest-neighbor algorithm.

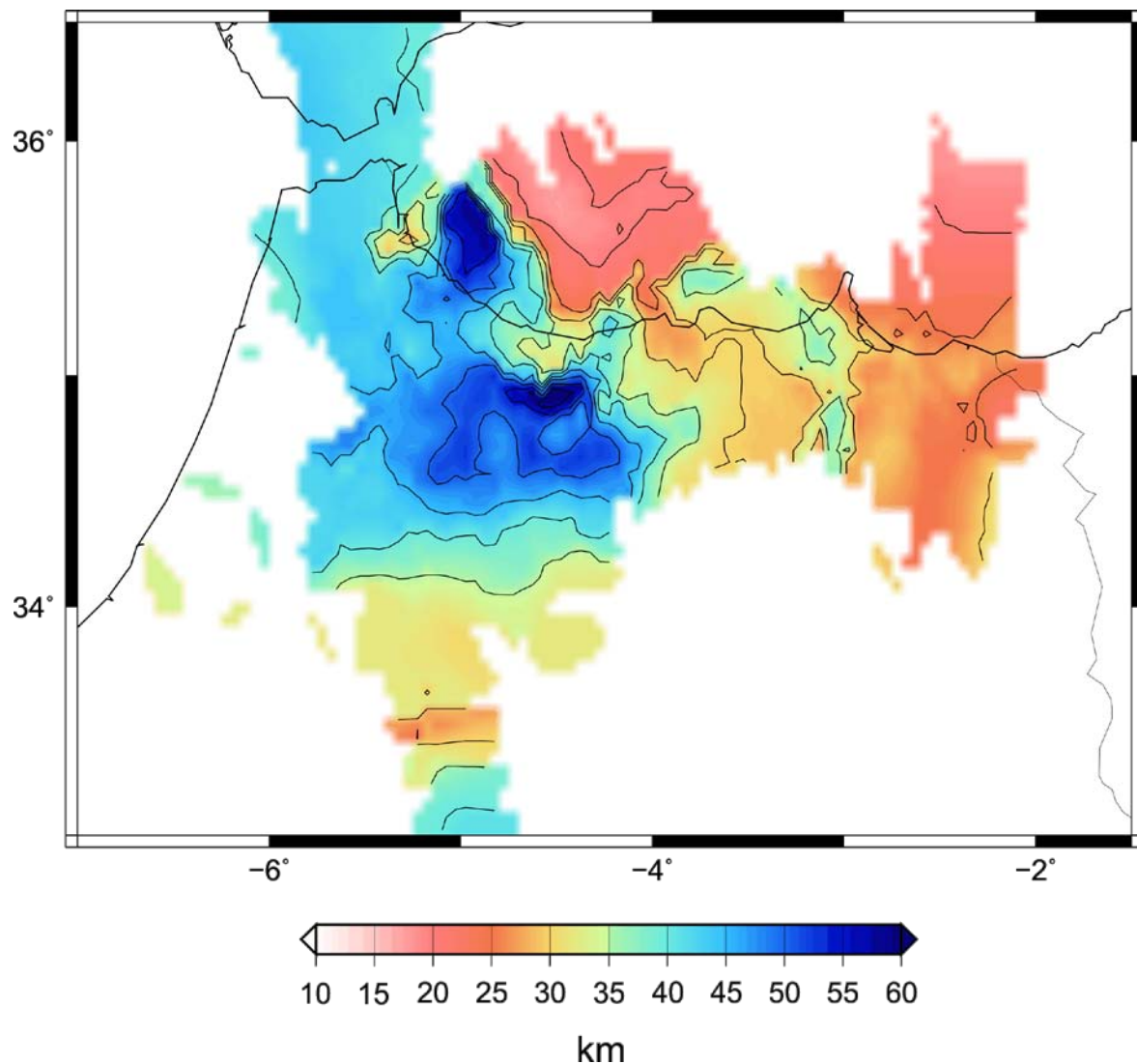


**Figure 7.8:** Moho-depth map as inferred from the combined results from wide-angle and RFs data. Thick black line outlines the isoleine of 40 km.

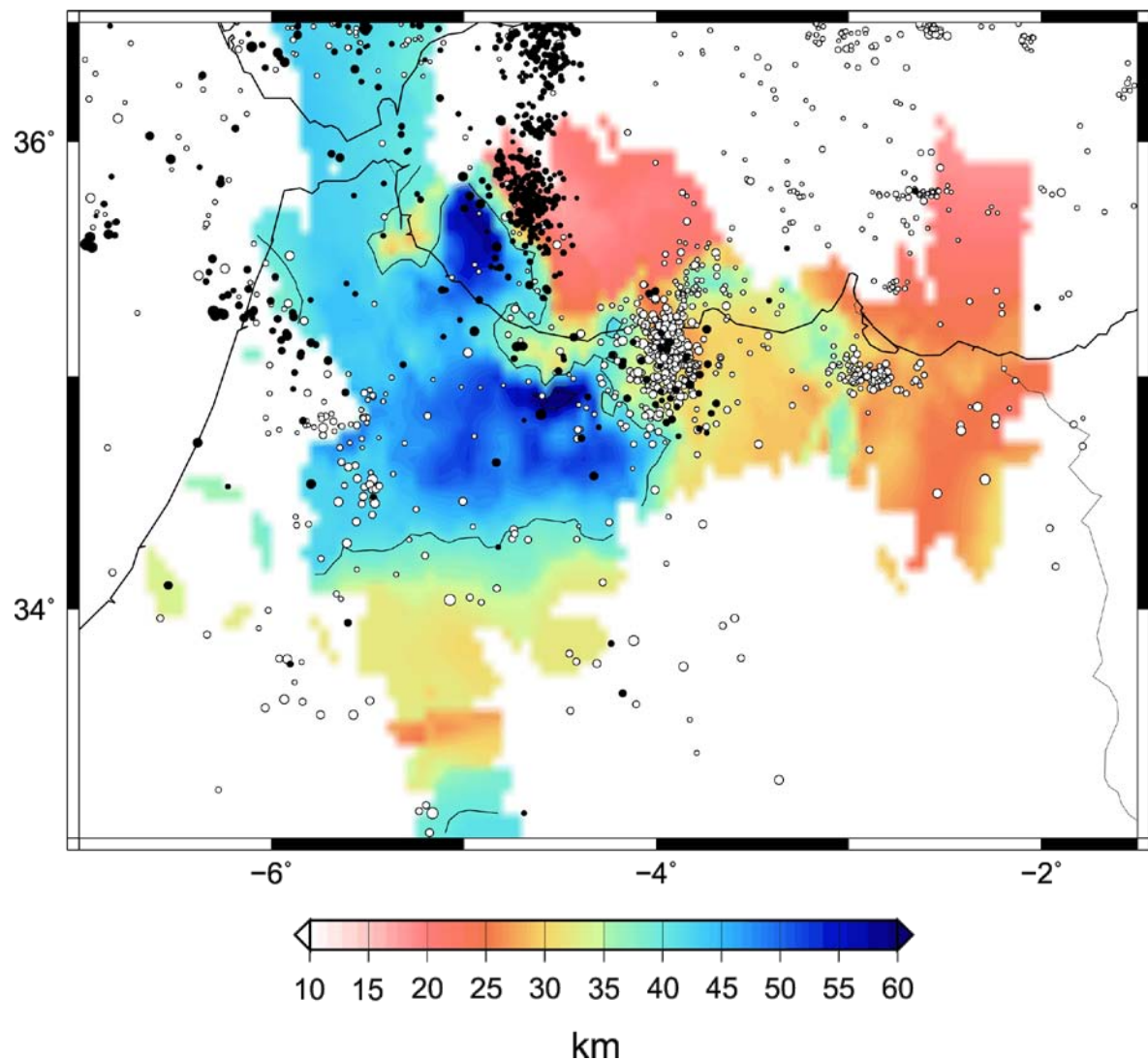


**Figure 7.9:** Moho-depth map overlaid by the seismicity with magnitude > 2 reported by the IGN catalogue in the period 2000-2014. White dots are for events with hypocenters above 40 km depth, black dots denote deeper events.



# **Part III: CONCLUSIONS**



## Chapter 8: Conclusions

The Rif Cordillera, situated in northern Morocco, together with the Betic Range, forms the Gibraltar Arc around the Alboran Sea. This asymmetric curved mountain belt originated during a Miocene continental-continental collision as a result of the westward motion of the Alboran domain between northwest Africa and Iberia. The complexity of this area led to several tectonic models. Previous geophysical studies reported a crustal thickness of 30-40 km beneath the Rif (Hatzfeld and Bensari, 1997; Wigger et al., 1992). Models that integrate both elevation and geoid gravity models anomalies assuming local isostasy suggest a poorly marked orogenic root below the Central Rif Cordillera that does not exceed 30 km depth (Fullea et al., 2010). However, recent Receiver Functions (RFs) studies (Mancilla et al. 2012; Thurner et al., 2014) reveal large variations of the crustal thickness under northern Morocco (between 22 km and 44 km). One of the main problems which have motivated to undertake this thesis is the scarce information of the crustal structure of the Rif Cordillera. The reflection/wide-angle seismic profiles carried out in the Rif Cordillera and presented here have provided high-quality data to resolve this question, and the analysis and interpretation of these data are essential contributions of this thesis. In addition, efforts have been made to compare and integrate the results with those deduced from other seismic methodologies for which data were also available. This analysis was likewise considered of interest to complete the scientific training. Therefore, one chapter has been devoted to the study of seismic velocity and anisotropy, covering the entire Euro-Mediterranean region from  $Pn$  (and  $Sn$ ) phases of regional earthquakes, and another two chapters compares the results of crustal depths with those obtained from low-fold wide-angle data, coming from the RIFSIS and WestMed projects, as well as Receiver Functions data, obtained from Topo-Iberia and PICASSO projects.

Thus, in this thesis we have considered and implemented various geophysical methodologies, such as seismic refraction and wide-angle reflection profiling, low-fold wide-angle seismic stack techniques, RFs and seismic tomography. The latter technique has been used to study  $Pn$  velocity and anisotropy of the Euro-Mediterranean region. The other three techniques have been used to study the crust beneath Northern Morocco. In the seismic refraction and wide-angle reflection case, the final velocity-depth models

have also been verified with the corresponding model densities (obtained from the classical relation  $Vp-\rho$  established by Christensen and Mooney, 1995), corroborating that they fit reasonably well with the Bouguer gravity anomalies.

The study of uppermost mantle seismic velocity and anisotropy tomography is based on the method developed by Hearn (1996), which determined temperature anomalies, pressure, compositional change and/or the presence of water in the crust-mantle boundary. This methodology has been applied to the entire Euro-Mediterranean region, by using  $Pn$  and  $Sn$  data. The results of the  $Pn$  tomography are quite consistent with previous 3-D tomographic images (Piromallo et al., 1997; Garcilla-Castellanos and Villaseñor, 2011) and show significant features well correlated with the geological structures. Low-velocity anomalies ( $<7.8$  km/s) are focused under orogenic areas (Betics, Pyrenees, Alps, Apennines and Calabrian Arc, Dinarides-Hellenides), while the high-velocities ( $>8.3$  km/s) are evidenced under tectonic stable areas. Large low-velocity zones are identified beneath Sardinia and the Balearic Islands, probably reflecting the presence of asthenospheric material at shallow levels.  $Pn$  anisotropy shows consistent FPD (fast polarization direction) orientations subparallel to major orogenic structures, such as Betics, Apennines, Calabrian Arc and Alps in agreement with the anisotropic parameters retrieved from teleseismic shear-waves splitting. This similarity suggests that the anisotropy lies within the subcrustal lithosphere beneath the orogens. On the contrary, at some regions (south-east Alps, southern Gibraltar Arc) the anisotropy results inferred from the two methods (the  $Pn$  anisotropy and the analysis of  $SKS$  splitting) clearly differ, suggesting that at least two anisotropy zones with different origin may exist. The  $Sn$  tomographic image has lower resolution but allows confirming independently most of the features evidenced in the  $Pn$  tomography. The overall velocity variations are similar to the  $Pn$  image, but the inspection of the  $Vp/Vs$  variations allow to associate the tectonically stable areas with increased  $Vp/Vs$  values and the most active ones with lower  $Vp/Vs$  ratios. The results and discussions presented in Chapter 4 have been published in the paper entitled “Uppermost mantle seismic velocity and anisotropy in the Euro-Mediterranean from  $Pn$  and  $Sn$  tomography” (Díaz, J., A. Gil and J. Gallart, Geophysical Journal International, 192, pp. 310-325, 2013)”.

In the Wide-Angle seismic chapter, we have worked with the two new seismic profiles acquired in the Rif Cordillera; the first one was orientated NS (70 km within the Iberian Peninsula and 330 km from Tetouan to the Middle Atlas) and the second profile was orientated EW (330 km from the Gharb Basin to Algerian border). Up to five shots of 1 Tn each have been detonated at selected sites in North Morocco and recorded by about 800 vertical-component seismic stations. Average station spacing was about 750 m along the profiles. The models were obtained from RAYINVR forward modeling program. The interpreted crustal structure differentiates two sedimentary layers on top of the basement (inferred from the observed first arrivals at short offsets), followed by upper, middle and lower crustal levels constrained by reflected phases visible in the record sections. The bottom of the crust is well defined from *PmP* phases, although the absence of *Pn* arrivals prevents to constrain upper mantle velocities. Average velocity values for the different layers in the models are, respectively: 3.5 and 4.7 km/s for the sediments, 5.9, 6.3 and 6.8 km/s within the crust, and 8 km/s below the Moho. These velocity-depth models obtained at the Rif Cordillera hold major variations in crustal thickness, especially along the EW profile, that shows a rapid change of 20 km in Moho depths within 40 km horizontal distances. Maximum depth around 50 km are found below the external Rif domain, while thinnest values of about 28 km are located eastwards of Nekkor fault zone, in the foreland and Atlasic terranes up to the Algerian border. The model along NS profile displays also marked differences in crustal thicknesses, ranging from 40 km beneath the Betics and internal Rif sampled domains, to 48 km beneath external Rif, as well as a progressive thinning southwards to Middle Atlas domain where the Moho is found at 30 km depth. Such strong lateral variations in crustal structure and particularly the importance of the crustal root beneath the external Rif area, are rather unexpected results according to surface topography. These velocity-depth models have been converted to density in order to compare the theoretical and observed results for Bouguer gravity anomalies in the region. The density models obtained are found to be quite consistent with the observed gravity anomalies. The results and discussion presented in the Chapter 5 have been published in the paper entitled “Crustal structure beneath the Rif Cordillera, North Morocco, from the RIFSIIS wide-angle reflected seismic experiment” (Gil, A., J. Gallart, J. Díaz, R. Carbonell, M. Torne, A. Levander and M. Harnafi, *Geochemistry, Geophysics, Geosystem*, 15, 2014, in press).

As a next step, we processed the wide-angle data as low-fold seismic stacks. We decided to undertake this analysis because the deployment logistics during the RIFSIS project permitted that all the stations recorded all the shots, not only those aligned with each profile, but also the offline shots. A hyperbolic time reduction was applied to the data, resulting in stacks in which the reflection from the Moho appears as subhorizontal energy arrivals. This provides also insights into the Moho depth variations offline the main seismic profiles. We also estimated the Moho geometry from the *PmP* phases identified in the stations deployed inland to record marine GASSIS experiment, from the recordings of both their air-gun shots and the five RIFSIS land shots. Considering all these *PmP* records and the locating the origin of the reflections at the midpoint of the corresponding ray-tracing, a 3-D was obtained in the northern Morocco region. Those arrival times are tentatively related to crustal thickness assuming a homogeneous crustal velocity. Even if those assumptions imply that large errors can arise in case of marked heterogeneities, we showed that the method could provide significant additional results in this region. At the same time, we analyzed RFs in the Rif domain area, to determine the crustal thickness beneath northern Morocco from passive seismics. We reprocessed data from both the Topo-Iberia and PICASSO experiments (see references in Chapter 7) and installed some additional stations to densify the data in the more complex region of interest. From the technique of H- $\kappa$  stack, we calculated the Moho discontinuity beneath each seismic station and the Poisson ratio (via velocity ratio  $Vp/Vs$ ). These studies support the results of crustal thickness obtained from the active seismic profiles. In some stations it was possible to observe more than one conversor related to the Moho discontinuity, which we associated with the internal complex architecture of an area that underwent multiple tectonic processes. These Moho-mapping results from the low-fold stacks and the RFs studies are currently in preparation for submission to a scientific journal.

A major achievement of this study is that a large crustal root is well documented in the central part of the Rif Cordillera, in good agreement with the area presenting large negative Bouguer anomaly values. Different authors have proposed that the Alboran slab may be attached to the lithosphere beneath this area (Vergés and Fernández, 2012). Other authors suggest that the crustal root beneath the external Rif domain is related to the Alboran slab (Pérouse et al., 2010; Bezada et al., 2013; Palomeras et al., 2014). The identified crustal root seems to support this hypothesis. However, both active and

passive data suggest that a crustal root extends to the coastline in a limited region close to 5° W, around the Beni-Boussera peridotites. From the Moho-depth maps presented, the regions with crustal thicknesses of 40 km defines an area with a small amount of seismicity, between the arcuate seismicity beneath western Alboran Sea and the more superficial seismicity in the Alhoceima area.

We interpreted the Rif Cordillera crustal structure as resulting from a complex interaction of the Miocene to present continent-continent collision between Iberia and Africa plates, coupled with rollback of the Neo-Thethys Alboran slab, which is agreement with the final 3-D numerical modeling of the western Mediterranean region, presented by Chertova et al. (2014) and van Hinsbergen et al. (2014). It is clear that even after several detailed studies, the debate on the tectonic evolution of the Gibraltar Arc System will be still ongoing. But we expect that the results presented in this thesis should deserve useful constraints for future geodynamic modeling on its evolution.



## References

- Acosta, J., A. Muñoz, P. Herranz, C. Palomo, M. Ballesteros, M. Vaquero and E. Uchupi (2001), Geodynamics of the Emile Baudot Escarpment and the Balearic Promontory, western Mediterranean, *Mar. Petrol. Geol.*, 18, 349–369.
- Aki, K. (1973), Scattering of P waves under the Montana Lasa, *J. Geophys. Res.*, 78, 1334-1346
- Aki, K., A. Christoffersson and E.S. Husebye (1977), Determination of the three-dimensional seismic structure of the lithosphere, *J. Geophys. Res.*, 82
- Al-Lazki,A.I., E. Sandvol, D. Seber, M. Barazangi, N. Turkelli, and R. Mohamad (2004), Pn tomographic imaging of mantle lid velocity and anisotropy at the junction of the Arabian, Eurasian and African plates, *Geophys. J. Int.*, 158, 1024–1040. doi: 10.1111/j.1365-246X.2004.02355.x
- Alonso-Zaraza, AM., I. Armenteros, JC. Braga, A. Muñoz, V. Pujalte, E. Ramos (coors.), J. Aguirre, G. Alonso-Gavilán, C. Arenas, JI. Baceta, J. Carballeira, JP. Calvo, A. Corrochano, JJ. Fornós, A. González, A. Luzón, JM. Martín, G. Pardo, A. Payros, A. Pérez, L. Pomar, JM. Rodríguez and J. Villena (2002), in *The Geology of Spain* by Gibbons W. and T. Moreno, 293-334, Geol. Soc., London
- Alpert, L.A., M.S. Miller, T.W. Becker and A. Allam (2013), Structure beneath the Alboran from geodynamic flow models and seismic anisotropy, *J. Geophys. Res.*, 118, 4265-4277, doi:10.1002/jgrb.50309.
- Ammon, C.J. (1997), An overview of receiver function analysis. <http://eqseis.geosc.psu.edu/~cammon/HTML/RftnDocs/rftn01.html>.
- Anahnah F., J. Galindo-Zaldívar, A. Chalouan, J. Poum, P. Ruano, A. Pedrera, A. Ruiz-Constán, M, Alhmamou, M. Benmakhlof, P. Ibarra and E. Asensio (2011a), Crustal resistivity structure of the southwestern transect of the Rif Cordillera (Morocco), *Geochem., Geophys., Geosystem.*, 12, Q12016, doi:1029/2011GC003783
- Anahnah, F., J. Galindo-Zaldivar, Chalouan, A. Pedrera, J. Ruano, J. Pous, W. Heise, A. Ruiz-Constan, M. Benmakhlof, A.C. López-Garrido, M.F.Ahmamou, C. Sanz de Galdeano, J. Arzate, P. Ibarra, L. González-Castillo, N. Bouregba, F. Corbo, and E. Asensio (2011b), Deep resistivity cross section of the intraplate Atlas Mountains (NW Africa): New evidence of anomalous mantle and related Quaternary volcanism, *Tectonics*, 30, TC5014, doi:10.1029/2010TC002859.
- Andrieux, J., JM. Fontbote and M. Mattauer (1971), Sur un modèle explicatif de l'arc de Gibraltar, *Earth Planet. Sci. Lett.*, 12, 191-238
- Ayarza, P., R. Carbonell, A. Teixell, I. Palomeras, D. Martí, A. Kchikach, M. Hanafi, A. Levander, J. Gallart, M.L. Arboleya, J. Alcalde, M. Charroud and M. Amrhar (2014), Crustal thickness and velocity structure across the Moroccan Atlas from long offset wide-angle

## References

- reflection seismic data: the SIMA experiment, *Geochem., Geophys., Geosystem.*, doi:10.1002/2013GC005164
- Azañón JM., J. Galindo-Zaldívar, V. García-Duñas and A. Jabaloy (2002), Alpine tectonics II: Betic Cordillera and Balearic Islands, in *The Geology of Spain* by Gibbons and T. Moreno, 401-416, *Geol. Soc, London*
- Azdimousa, A. J. Bourgois, G. Poupeau, M. Vázquez, L. Asebriy and E. Labrin (2013), Fission track thermochronology of the Beni Bousera peridotite massif (Internal Rif, Morocco) and the exhumation of ultramafic rocks in the Gibraltar Arc, *Arab. J. Geosci.*, doi:10.1007/s12517-013-0924-3
- Babuska, V and M. Cara, Modern approach in geophysics. Seismic anisotropy in the Earth. Kluwer Academic publishers, London, (1991)
- Baccheschi, P., L. Margheriti, and M. S. Steckler (2008), SKS splitting in southern Italy: Anisotropy variations in a fragmented subduction zone, *Tectonophysics*, 462, 49–67, doi:10.1016/j.tecto.2007.10.014.
- Backus, G.E. (1965), Possible forms of seismic anisotropy of the uppermost mantle under oceans, *J. Geophys. Res.*, 70, 3429-3439.
- Balanya, J. C., V. Garcia-Duenas, J. M. Azanon, and M. Sanchez-Gomez (1997), Alternating contractional and extensional events in the Alpujarride nappes of the Alboran Domain (Betics, Gibraltar Arc), *Tectonics*, 16(2), 226 – 238.
- Banda, E. and J. Ansorge (1980), Crustal structure under the central and eastern part of Betic Cordilleras, *Geophys. J. R. Astron. Soc.* 63, 515–532
- Bargach, K., P. Ruano, A. Chabli, J. Galindo-Zaldívar, A. Chalouan, A. Jabaloy, M. Akil, M. Ahmamou, C. Sanz de Galdeano, and M. Benmaklouf (2004), Recent Tectonic Deformations and Stresses in the Frontal Part of the Rif Cordillera and the Saïss Basin (Fes and Rabat Regions, Morocco), *Pure appl. Geophys.*, 161, 521-540, doi:10.1007/s00024-003-2461-6
- Barruol, G., A. Souriau, A. Vauchez, J. Díaz, J. Gallart, J. Tubia and J. Cuevas (1998), Lithospheric anisotropy beneath the Pyrenees from shear wave splitting, *J. Geophys. Res.*, 103, 30039-30054.
- Barruol, G., M. Bonnin, H. Pedersen, G. H.R. Bokelmann and C. Tiberi (2011), Belt-parallel mantle flow beneath a halted continental collision: The Western Alps, *Earth and Planetary Science Letters* 302 429–438. doi:10.1016/j.epsl.2010.12.040
- Beccaluva, L., G. Bianchini, C. Natali and F. Siena (2011), Geodynamic control on orogenic and anorogenic magmatic phases in Sardinia and Southern Spain: inferences for the Cenozoic evolution of the western Mediterranean, *Lithos*, 123, 218-224.
- Bezada, MJ., C. Zelt (2011), Gravity inversion using seismically derived crustal density models and genetic algorithms: an application to the Caribbean-South American Plate boundary, *Geophys. J. Int.*, doi:10.1111/j.1365-246X.2011.04965.x

## References

- Bezada, M.J., E.D. Humphreys, D.R. Toomey, M. Harnafi, J.D. Dávila, and J. Gallart (2013), Evidence for slab rollback in westernmost Mediterranean from improved upper mantle imaging, *Earth Planet. Sci. Lett.*, 368, 51-60, doi:10.1016/j.espl.2013.02.024
- Bijwaard, H. and W. Spakman (2000), Non-linear global P-wave tomography by iterated linearized inversion, *Geophys. J. Int.*, 141, 71– 82.
- Blanco MI and W. Spakman (1993), The P wave velocity structure of the mantle below the Iberian Peninsula: evidence for subducted lithosphere below Spain. *Tectonophysics.*, 221, 13–34, doi:10.1016/0040-1951(93)90025-F
- Booth-Rea, G., A. Jabaloy-Sánchez, A. Azdimousa, L. Asebriy, M. VázquezVilchez and M. Martínez-Martínez (2012), Upper-crustal extension during oblique collision: the Temsamane extensional detachment (eastern Rif, Morocco). *Terra Nova*, 24, 505-512, doi:10.1111/j.1365-3121.2012.01089.x
- Boschi, L., B. Fry, G. Ekström, and D. Giardini (2009), The European upper mantle as seen by surface waves, *Surv. Geophys.*, 30, 463–501, doi:10.1007/s10712-009-9066-2.
- Bouybaouene, ML., B. Goffé and A. Michard (1998), High-Pressure granulites on top of the Beni Bousera peridotites, Rif Belt, Morocco: a record of an ancient thickened crust in the Alboran domain, *Bull. Soc. Géol. Fr.* 169, 153-162
- Brocher, TA (2005), Empirical relations between elastic wavespeeds and density in the earth's crust. *Bull. Seism. Soc. Am.*, 95, 6, 2081-2092, doi:10.1785/01200050077
- Buontempo, L., G.H.R Bokelmann, G. Barruol and J. Morales (2008), Seismic anisotropy beneath southern Iberia from SKS splitting, *Earth Planet. Sci. Lett.*, 273, 237-250, doi:10.1016/j.epsl.2008.06.024
- Calvert, A., E. Sandvol, D. Seber, M. Barazangi, S. Roecker, T. Mourabit, F. Vidal, G. Alguacil, and N. Jabour (2000a), Geodynamic evolution of the lithosphere and upper mantle beneath the Alboran region of the western Mediterranean: Constraints from travel times tomography, *J. Geophys. Res.*, 105, 10,871-10,898.
- Calvert, A., E. Sandvol, D. Seber, M. Barazangi, F. Vidal, G. Alguacil and N. Jabour (2000b), Propagation of regional seismic phases (Lg and Sn) and Pn velocity structure along the Africa-Iberia plate boundary zone: tectonic implications, *Geophys. J. Int.* 142, 384-408
- Carbonell, R., J. Gallart and A. Pérez-Estaún (2002), Modelling and imaging the Moho transition: the case of the southern Urals, *Geophys. J. Int.*, 149, 134-148
- Carbonell, R., A. Levander and R. Kind (2013), The Mohorovicic discontinuity beneath the continental crust: An overview of seismic constraints *Tectonophysics.*, 609, 353-376, doi:10.1016/j.tecto.2013.08.037
- Carbonell, R., P. Ayarza, J.Gallart, J. Diaz, M. Harnafi, A. Levander, and A.Teixell (2014), From the Atlas to the Rif a Crustal seismic image across Morocco: The SIMA & RIFSEIS control source wide-angle seismic reflection data. Paper presented at EGU General

## References

- Assembly, European Geosciences Union, Vienna, Austria
- Carminati, E. and C. Doglioni (2004), Europe-Mediterranean tectonics. In Encyclopedia of Geology, Elsevier, 135-146.
- Cembrowski, M. (2012), Crustal Structure in the Northern Part of Morocco from Wide-Angle Seismics, Master Thesis, Westfälischen Wilhelms-Universität Münster, Münster, Germany
- Cembrowski, M., J. Gallart, M. Schimmel, J. Diaz, R. Carbonell, E. Gracia, C. Ranero, J. Schmaltz, C. Thomas, D. El Ouai, and I. Palomeras (2013) Mapping the onshore-offshore crustal transition at the Westernmost Mediterranean from seismic profiling. Paper presented at EGU General Assembly, European Geosciences Union, Vienna, Austria
- Cerveny, V., I.A. Molotkov and I. Psencik (1977), Ray method in seismology, Charles University, Praha, Czech Republic.
- Chalouan, A. and A. Michard (1990), The Ghomarides nappes, Rif coastal Range, Morocco: a Variscan chip in the Alpine belt, Tectonics, 9, 1565-1583
- Chalouan, A., A. Ouazani-Touhami, L. Mouhir, R. Saji and M. Benmakhlouf (1995), Les failles normales à faible pendage du Rif interne (Maroc) et leur effet sur l'amincissement crustal du domaine D'Alboran, Geogaceta, 17, 3.
- Chalouan, A., A. Michard, H. Feinberg, R. Montigny, and O. Saddiqi (2001), The Rif mountain building (Morocco): a new tectonic scenario, Bull. Sec. geol. France, 172(5), 603-616.
- Chalouan, A., and A. Michard (2004), The Alpine Rif Belt (Morocco): a case of mountain building in a subduction-subduction-transform fault triple junction, Pure appl. Geophys., 161, 489-519, doi:10.1007/s00024-003-2460-7
- Chalouan, A., J. Galindo-Zaldívar, M. Akil, A. Chabli, P. Ruano, K. Bargach, C. Sand de Galdeano, M. Benmakhlouf, M. Ahmamou and L. Gourari (2006), Tectonic wedge escape in the southwestern front of the Rif Cordillera (Morocco), in Tectonics of the Western Mediterranean and North Africa, edited by Moratti, G and A. Chalouan, 101-118, Geological Society, London
- Chalouan, A., A. Michard, Kh. El Kadiri, F. Negro, D. Frizon de Lamotte, J.I. Soto, and O. Saddiqi (2008), The Rif Belt, in Continental Evolution: The Geology of Morocco, edited by Michard, A., O. Saddiqi, A. Chalouan, and D. Frizon de Lamotte, 203-302, Springer, Berlin
- Chertova, M., W Spakman, T. Geenen, A. Van den Berg and D. Van Hinsbergen (2014a), Underpinning tectonic reconstructions of the western Mediterranean region with dynamic slab evolution from 3-D numerical modeling, J. Geophys. Res. Solid Earth, 119, 5876-5902, doi:10.1002/2014JB011150
- Chertova, M., W. Spakman, A.P. van den Berg and D.J.J. van Hinsbergen (2014b), Absolute plate motion and regional subduction evolution, Geochem., Geophys., Geosys., 15, 3780-3792, doi:10.1002/2014GC005494
- Comas, M. C., J. P. Platt, J. I. Soto, and A. B. Watts (1999), The origin and tectonic history of

## References

- the Albora n Basin: Insights from Leg 161 results, Proc. Ocean Drill. Program Sci. Results, 161, 555 – 579.
- Crampin, S. (1981), A review of wave motion in anisotropic and cracked elastic media. Wave Motion, 3, 342-391.
- Dewey, J.F. (1988), Extensional collapse of orogens. Tectonics 7,1123–1139.
- Díaz, J. and J. Gallart (2009), Crustal structure beneath the Iberian Peninsula and surrounding waters: A new compilation of deep seismic soundig results, Physics oh the Earth and Planetary Interiors 173, 181-190.
- Díaz, J., A. Villaseñor, J. Gallart, J. Morales, A. Pazos, D. Córdoba, J. Pulgar, J. L. García-Lobón and M. Harnafi (2009), The IBERARRAY broadband seismic network: a new tool to investigate the deep structure beneath Iberia, Orfeus News!, 8,2.
- Díaz, J., J. Gallart, A. Villaseñor, F. Mancilla, A. Pazos, D. Córdoba, J.A. Pulgar , P. Ibarra, M. Harnafi and the TopoIberia Seismic Working Group (2010), Mantle dynamics beneath the Gibraltar Arc (western Mediterranean) from shear-wave splitting measurements on a dense seismic array. Geophys. Res. Lett.,37,18,L18304,doi: 10.1029/2010GL044201.
- Díaz, J., A. Gil, and J. Gallart (2013), Uppermost mantle seismic velocity and anisotropy in the Euro-Mediterranean region from Pn and Sn tomography, Geophys. J. Int., 192, 310-325, doi:10.1093/gji/ggs016
- Díaz J., and J. Gallart (2014), Seismic anisotropy from the Variscan core of Iberia to the Western African Craton: New constrains on upper mantle flow at regional scales. Earth Planet. Sci. Lett., 394, 48-47, doi:10.1016/j.epsl.2014.03.005
- DeCelles, P.G., and K. A. Giles (1996), Foreland basin systems, Basin Res., 8, 105-123
- DeCelles, P.G. (2012), Foreland basin systems revisited: variations in response to tectonic settings in: Tectonics of Sedimentary Basins: Recent Advances, edited by Busby, C., and A, Azor Pérez, Wiley-Blackwell,
- Durand Delga. M., L. Hottinger, J. Marcais, M. Mattauer, Y. Millard and G. Suter (1960-1962), Données actuelles sur structures du Rif. Soc. Géol. Fr. (livre mémoire P. Fallot). t.1. 399-442.
- Dziewonski, A.M., and D.L. Anderson (1981), Preliminary Reference Earth Model (PREM), Phys. Earth Planet. Inter., 25, 297-356
- Eberhart-Phillips, D. (1990), Three-dimensional P and S velocity structure in the Coalinga region, California, J. Geophys. Res. 95, 15343–15363.
- Ehsan, S.A., R. Carbonell, P. Ayarza, D. Martí, A. Pérez-Estaún, D.J. Martínez-Poyatos, J.F. Simancas, A. Azor and L. Mansilla (2014), Crustal deformation styles along the reprocessed deep seismic reflection transect of the Central Iberian Zone (Iberian Peninsula), Tectonophysics, 621, 159-174, doi:10.1016/j.tecto.2014.02.014
- El Kadiri Kh., A. Linares and F. Oloriz (1992), La Dorsale calcarie rifaine (Maroc

## References

- septentrional): evolution stratigraphique et géodynamique durant le Jurassique-Crétacé, Notes Mém. Serv. Géol. Maroc, 336, 217-265
- El Mirihi, A. (2005), Structure et cinématique de la mise en place des nappes des flyschs maurétaniens (Rif externe nord oriental): Elaboration d'un modèle, Ph.D. thesis, Univ. De Tetuan, Tetuán, Morocco.
- El Moudnib, L., A. Villaseñor, M. Harnafi, M.M.Himmi and J. Gallart (submitted), Crust structure of northern Morocco and southern Iberian Peninsula from local earthquake tomography, Tectonophysics
- Enderle, U., J. Mechie, S. Sobolev and K. Fuchs (1996), Seismic anisotropy within the uppermost mantle of southern Germany. Geophys J. Int. 125, 3, 747-77. doi: 10.1111/j.1365-246X.1996.tb06021.x
- Evangelidis, C.P., W.T. Liang, N.S. Melis and K.I. Konstantinou (2011), Shear wave anisotropy beneath the Aegean inferred from SKS splitting observations, J. Geophys. Res., 116, B04314, doi:10.1029/2010JB007884.
- Faccenna, C., C. Piromallo, A. Crespo-Blanc, L. Jolivet, F. Rossetti (2004), Lateral slab deformation and the origin of the Western Mediterranean arcs, Tectonics 23, doi:10.1029/2002TC001488.
- Fadil, A., P. Vernant, S. McClusky, R. Reilinger, F. Gomez, D. B. Sari, T. Mourabit, K. L. Feigl, and M. Barazangi (2006), Active tectonics of the western Mediterranean: GPS evidence for roll back of a delaminated sub-continental lithospheric slab beneath the Rif mountains, Geology, 34, 529–532, doi:10.1130/G22291.1.
- Fernàndez, M., X. Berástegui, C. Puig, D. Garcia-Castellanos, M.J. Jurado, M. Torne, and C. Banks (1998) , Geophysical and geological constraints on the evolution of the Guadalquivir foreland basin, Spain, in Cenozoic Foreland Basins of Western Europe, edited by Mascle, A., C. Puigdefabregas, H.P. Luterbacher, M. Fernàndez, 29-48 Geological Society, London
- Frizon de Lamotte, D. (1985), La structure du Rif oriental (Maroc), rôle de la tectonique longitudinale et importance des fluides, Thèse Doct. Etat, Univ. P. et. M. Curie, Paris
- Frizon de Lamotte, et al., (2004) TRASNSMED-transect I: Betics, Alboran Sea, Rif, Moroccan Meseta, High Atlas, JbelSaghro, Tindouf Basin, in The TRANSMED Atlas-the Mediterranean Region from Crust to Mantle edited by Cavazza, W., et al. 91-96 Springer, Berlin
- Fullea, J., M. Fernàndez, J.C. Afonso, J. Vergés, and H. Zeyen (2010), The structure and evolution of the lithosphere-asthenosphere boundary beneath the Atlantic-Mediterranean Transition Region, Lithos, 120 (1-2), 74-95, doi:10.1016/j.lithos.2010.03.003
- Fullea, J., J. Rodríguez-González, M. Charco, Z. Martinec, A. Negredo, and A. Villaseñor (2014), Perturbing effects of sub-lithospheric mass anomalies in GOCE gravity gradient and other gravity data modelling: Application to the Atlantic-Mediterranean transition zone. Int.

## References

- J. Appl. Earth Observ. Geoinf. doi:10.1016/j.jag.2014.02.003
- Gallart, J., R. Carbonell, J. Díaz, A. Gil, M. Ruiz , M. Harnafi, L. Elmoudnib, D. ElOuai, A. Levander , I. Palomeras, D. Cordoba and FJ. Alonso-Chaves (2012), Crustal structure beneath the Rif Cordillera, North Morocco, from active seismic profiling, Paper presented at EGU General Assembly, European Geosciences Union, Vienna, Austria
- Gallart, J. and J. Diaz (2013), Outstanding Moho depth variations in the Iberian Peninsula, NW Africa and surrounding margins, revealed from controlled-source seismic surveys. Paper presented at EGU General Assembly, European Geosciences Union, Vienna, Austria
- Gallastegui, J., Pulgar, J.A., Gallart, J., 2002. Initiation of an active margin at North Iberian continent-ocean transition. *Tectonics* 21, doi:10.1029/2001TC901046
- Galvé, A., J. Gallart, J. Díaz, M. Fernández, I. Grevemeyer, CR. Ranero and the WestMed Team (2007), Probing the deep structure of the Eastern Alboran Basin (Western Mediterranean) by wide-angle seismics, Paper presented at EGU General Assembly, European Geosciences Union, Vienna, Austria
- García-Castellanos, D. (2002), Interplay between lithospheric flexure and river transport foralend basins. *Basin Res.* 14 (2), 89-104, doi:10.1046/j.1365-2117.2002.00174.x
- García-Castellanos, D., and A. Villaseñor (2011), Messinian salinity crisis regulated by competing tectonics and erosion at the Gibraltar Arc. *Nature* 480, 359-363, doi:10.1038/nature10651
- García-Lobón, C. Rey-Moral, C. Ayala, L.M. Martín-Parra, J. Matas and M.I. Reguera (2014), Regional structure of the southern segment of Central Iberian Zone (Spanish Variscan Belt) interpreted from potential field images and 2.5 D modelling of Alcudia gravity transect, *Tectonophysics*, 614, 185-202, doi:10.1016/j.tecto.2013.12.005
- Gil, A., J. Gallart, J. Díaz, R. Carbonell, M. Torne, A. Levander and M. Harnafi (2014, in press.), Crustal structure beneath the Rif Cordillera, North Morocco, from the RIFSIS wide-angle reflection seismic experiment, *Geochem. Geophys. Geosys.* 15
- Giacomuzzi, G., M. Civalleri, P. De Gori and C. Chiarabba (2012), A 3D Vs model of the upper mantle beneath Italy: Insight on the geodynamics of central Mediterranean, *Earth Planet. Sci. Lett.*, 335-336, 105-120. Doi: 10.1016/j.epsl.2012.05.004
- Gomez, F., W. Beauhamp, and M. Barazangi (2000), Role of the Atlas Mountains (northwest Africa) within the African-Eurassian plate-boundary zone. *Geology*, 28(9), 775-778, doi:10.1130/0091-7613
- Gómez-Ortiz, D., B. N. P. Agarwal, R. Tejero and J. Ruiz (2011), Crustal structure from gravity signatures in the Iberian Peninsula. *GSA Bulletin* vol. 123, no. 7/8, 1247-1257, doi:10.1130/B30224.1
- Gràcia, E., CR. Ranero, I. Grevemeyer, The WestMed, TopoMed and Geomargen-1 cruise parties (2012), Seismic Images and Wide-Angle Velocity constrains of the structure and

## References

- geodynamic origin of the Gibraltar Arc system: A geological interpretation of the Gulf of Cadiz imbricated wedge, the western and eastern Alboran basins, and the South-Balearic basin, Paper presented at AGU General Assembly, American Geosciences Union, San Francisco, USA
- Gràcia, E., R. Bartolome, H. Perea, L. Gómez de la Peña, C. Ranero, C. Lo Iacono, S. Martínez-Loriente, X. Moreno and J. Dañobeitia (2014), Seismogenic potential of active faults in the Alboran Sea revealed by multiscale seismic imaging, Paper presented at 16<sup>th</sup> SEISMIX symposium, Castelldefels, Spain.
- Grad, M., T. Tiira, and ESC Working Group (2009), The Moho depth map of the European Plate. *Geophysical Journal International*, 176: 279–292. doi: 10.1111/j.1365-246X.2008.03919.x
- Gurría E., and J. Mezcua (2000), Seismic tomography of the crust and lithospheric mantle in the Betic Cordillera and Alboran Sea. *Tectonophysics*, 329, 99–119
- Gutscher, M.A., J. Malod, J.P. Rehault, I. Contrucci, F. Klingelhoefer, L. Mendes-Victor, and W. Spakman (2002), Evidence for active subduction beneath Gibraltar, *Geology*, 30, 1071-1074
- Hafid, M., G. Tari, D. Bouhadioui, I. El Moussaid, H. Echarfaoui, A. Ait Salem, M. Nahim, and M. Dakki (2008), Atlantic Basins, in Continental Evolution: The Geology of Morocco edited by Michard, A., O. Siddiqi, A. Chalouan, and D. Frizon de Lamotte, 303-330, Springer, Berlin
- Hatzfeld, D., and D. Bensari (1977), Grands profile sismiques dans la région de l'arc de Gibraltar, *Bull. Sec. Géol. France*, 7, XIX-4, 749-756
- Hearn, T.M. (1996), Anisotropic Pn tomography in the western United States, *J. Geophys. Res.* 101 (B2), 8403-8414.
- Hearn, T.M. (1999), Uppermost mantle velocities and anisotropy beneath Europe, *J. Geophys. Res.* 104 (B7), 15123-15139
- Hearn, T.M. and J.F. Ni (1994), Pn velocities beneath continental collision zones: the Turkish-Iranian Plateau, *Geophys. j. Int.* 117, 273-283.
- Hildenbrand, T. G., R. P. Kucks, M. F. Hamouda, and A. Bellot (1988), Bouguer gravity map and related filtered anomaly maps of Morocco, U.S. Geol. Surv. Open File Rep., 88-517.
- Hoernle, K., Y.S. Zhang and D. Graham (1995), Seismic and geochemical evidence for large-scale mantle upwelling beneath the eastern Atlantic and western and central Europe, *Nature*, 374, 34-39
- International Seismological Centre, On-line Bulletin, <http://www.isc.ac.uk>, Internatl. Seis. Cent., Thatcham, United Kingdom (2010)
- IUGG (2012), IUGG Yearbook 2012, Union Géodésique et Géophysique Internationale, Published by Secretary General Alik Ismail-Zadeh, Germany
- Jolivet, L., C. Faccenna and C. Piromallo (2009), From mantle to crust: Stretching the

## References

- Mediterranean. Earth Planet. Sci. Lett., 285, 198–209, doi:10.1016/j.epsl.2009.06.017
- Julià, J., C.J. Ammon and R.B. Hermann (2003), Evaluation of deep sediment velocity structure in the New Madrid Seismic Zone, Bull. Seismol. Soc. Am., 94, 334-340
- Karato, S.I. and H. Jung (1998), Water, partial melting and the origin of the seismic low velocity and high velocity zone in the upper mantle, Earth planet. Sci. Lett., 157, 193-207.
- Kornprobst, J (1973), Petrological studies of “acustic basement” and associated breccia at site 121 – western Alboran Basin: a comparision with the Betico-Rifean basement, in Init.Repts. DSDP, 13 (Pt. 12) by Ryan, WBF, KJ Hsü et al. 759-761, U.S. Govert. Printing Office, Washinton DC
- Koulali, A., D. Ouazar, A. Tahayt, R.W., King, P. Vernant, R.E. Reilinger, S. McClusky, T. Mourabit, J.M. Davila, and N. Amraoui (2011), New GPS constraints on active deformation along the Africa-Iberia plate boundary, Earth Planet. Sci. Lett., 308, 211-217, doi:10.1016/j.epsl.2011.05.048
- Koulakov, I, M.K. Kaban, M. Tesauro and S. Cloetingh (2009), P- and S-velocity anomalies in the upper mantle beneath Europe from tomographic inversion of ISC data, Geophys. J. Int. 179, 345–366 doi: 10.1111/j.1365-246X.2009.04279.x
- Langton, C. A. (1979), Structure under Mount Rainier, Washington, inferred from teleseismic body waves, J. Geophys. Res., 84, 4749-4762.
- Legendre, CP; T. Meier, S. Lebedev, W. Friederich and L. Viereck-Götte (2012), A shear wave velocity model of the European upper mantle from automated inversion of seismic shear and surface waveforms, Geophys. J. Int., 191, 282-304, doi:10.1111/j.1365-246X.2012.05613.x
- Levander, A., M. Bezada, F. Niu, E. Humphreys, I. Palomeras, S. Thurner, J. Masy, M. Scmitz, J. Gallart, R. Carbonell and M.S. Miller (2014), Subduction-driven recycling of continental margin lithosphere, NATURE, 515, 253-256, doi:10.1038/nature13878
- Lippitsch, R., E. Kissling and J. Ansorge (2003), Upper mantle structure beneath the Alpine orogen from high resolution teleseismic tomography, J. Geophys. Res. 108 (B8), 2376. doi:10.1029/2002JB002016.
- Lombardi, A.M., M. Cocco and W. Marzocchi (2010), On the increase of background seismicity rate during the 1997-1998 Umbria-Marche (central Italy) sequence: apparent variation of fluid -driven triggering?, Bull. Seismol. Soc. Am., 100, 1138-1152, doi:10.1785/0120090077
- Lonergan, L., and N. White (1997), Origin of the Betic-Rif mountain belt, Tectonics, 16, 504-522, doi:10.1029/96TC03937
- Mancilla, F.L., D. Stich, J. Morales, J. Julià, J. Diaz, A. Pazos, D. Córdoba, J.A. Pulgar, P. Ibarra, M. Harnafi, and F. Gonzalez-Lodeiro (2012), Crustal thickness variations in Northern Morocco, J. Geophys. Res., 177, B02312, doi:10.1029/2011JB008608
- Marone, F., S. van der Lee and G. Giardini (2004), Shallow anisotropy in the Mediterranean

## References

- mantle from Surface waves, Geophys. Res. Lett., 31 (L06624), 1-4, doi:10.1029/2003GL018948
- Martínez-Díaz, JJ., E. Masana, JL. Hernández-Enrile, P. Santasach (2001), Evidence for coseismic events of recurrent prehistoric deformation along the Alhama de Murcia fault, southern Spain, *Acta Geologica Hispanica*, 36 (3-4), 12
- Martínez-Poyatos, D., et al. (2012), Imaging the crustal structure of the Central Iberian Zone (Variscan Belt): the ALCUDIA Deep seismic reflection transect. *Tectonics*, 31, p. TC3017, doi:10.1029/2011TC002995
- Mauffret, A., D. Frizon de Lamotte, S. Lallemand, C. Gorini and A. Maillard (2004), E-W opening of the Algerian Basin (Western Mediterranean). *Terra Nova*, 16, 257-264.
- Medialdea, T., E. Suriñach, R. Vegas, E. Banda, and J. Ansorge (1986), Crustal structure under the western end of the Betic cordillera (Spain), *Annales Geophysicae*, 4 (B4), 457-464.
- Miller, M.S., A. Allam, T.W. Becker, J.F. Dileo, and J. Wookey (2013), Constraints on the tectonic evolution of the westernmost Mediterranean and northwestern Africa from shear wave splitting analysis. *Earth Planet. Sci. Lett.* doi:10.1016/j.epsl.2013.05.036
- Mohsen, A., R. Hofstetter, G. Bock, R. Kind, M. Weber, K. Wylegalla an G. Rümpker (2005), A receiver function study across the Dead Sea Transform, *Geophys. J. Int.*, 160(3), 948-960, doi:10.1111/j.1365-246X.2005.02534x
- Muñoz, J.A. (1992), Evolution of a continental collision belt: ECORS- Pyrenees crustal balanced cross section. In: McClay, K. (Ed.), *Thrust Tectonics*. Chapman and Hall, New York, 235–246.
- Mutlu, A.K. and H. Karabulut (2011) Anisotropic Pn tomography of Turkey and adjacent regions, *Geophys. J. Int.* doi: 10.1111/j.1365-246X.2011.05235.x
- Nair, S.K., S.S. Gao, K.H. Liu and P.G. Silver (2006), Southern African crustal evolution and composition: constraints from receiver function studies, *J. Geophys. Res.*, 111(B2), 1-17, doi:10.1029/2005JB003802
- Paige, C., and M. Saunders (1982), LSQR: An Algorithm for Sparse Linear Equations and Sparse Least Squares, *ACM Transactions on Mathematical Software*, 8(1), 43-71
- Palano, M., P. Gonzalez and J. Fernandez (2013), Strain and stress fields along the Gibraltar Orogenic Arc: constraints on active geodynamics *Gondwana Res.*, 23, 1071–1088 doi:10.1016/j.gr.2012.05.021
- Palomeras, I., S. Thurner, A. Levander, K. Liu, A. Villaseñor, R. Carbonell and M. Harnafi (2014), Finite-frequency Rayleigh wave tomography of the western Mediterranean: Mapping its lithospheric structure, *Geochem., Geophys., Geosyst.*, 15 (1), 140-160, doi:10.1002/2013GC004861
- Pei, S., Y. Sun and MN. Toksöz (2011a), Tomographic Pn and Sn velocity beneath the continental collision zone from Alps to Himalaya, *J. Geophys. Res.*, vol 116 (B10311), 10

## References

- Pei, S., Y. Sun, MN. Toksöz, YJ. Chen, X. Gao, Z. Wang, J. Zhao and H. Liu (2011b), Imaging Poisson's Ratio of the Uppermost Mantle beneath China, *Bull. Seis. Soc. Am.*, 101, 3, 1452-1461, doi: 10.1785/0120090024
- Pérouse, E., P. Vernant, J. Chery, R. Reilinger, and S. McClusku (2010), Active surface deformation and sub-lithospheric processes in the western Mediterranean constrained by numerical models, *Geology* 38(9), 823-826, doi:10.1130/G30963.1
- Piromallo, C., and A. Morelli (2003), P wave tomography of the mantle under the Alpine - Mediterranean area. *J. Geophys. Res.*, 108(B2), 2065, doi:10.1029/2002JB001757, 2003
- Platt, J.P. and R.L.M. Vissers (1989), Extensional collapse of thickened continental lithosphere: An hypothesis for the Alboran Sea and Gibraltar arc, *Geology*, 17, 540-543.
- Platt, JP., ThW. Becker, RL. Evans, ED. Humphreys, C-T Lee and A. Levander (2008), PICASSO: Testing Models for Upper Mantle Processes beneath the Alboran Basin and the Gibraltar Arc (Western Mediterranean) Paper presented at AGU General Assembly, American Geosciences Union, San Francisco, USA
- Platt, JP., W.M. Behr, K. Johanesen and J.R. Williams (2013), The Betic-Rif Arc and Its Orogenic Hinterland: A Review. *Annu. Rev. Earth Planet. Sci.*, 41, 313–357, doi:10.1146/annurev-earth-050212-123951
- Pous, J., D. Martínez-Poyatos, W. Heise, F. Monteiro Santos, J. Galindo-Zaldívar, P. Ibarra, A. Pedrera, A. Ruiz-Constán, F. Anahnah, R. Gonçalves and A. Mateus (2011), Constraints on the crustal structure of the internal Variscan Belt in SW Europe: A magnetotelluric transect along the eastern part of Central Iberian Zone, Iberian Massif, *J. Geophys. Res.*, 116, B02103, doi:10.1029/2010JB007538.
- Précigout, J., F. Gueydan, C.J. Garrido, N. Cogné and G. Booth-Rea (2013), Deformation and exhumation of the Ronda peridotite (Spain), *Tectonics*, 32(4), 1011-1025, doi:10.1002/tect.20062
- Puglisi, D. (2009), Early Cretaceous flysch from Betic-Maghrebian and Europe Alpine Chains (Gibraltar Strait to the Balkans): comparision and palaeotectonic implications, *Geologica Balcanica*, 38 (1-3), 15-22
- Romagny, A., Ph. Münch, J.-J. Cornée, M. Corsini, A. Azdimousa, M.C. Meline-Dobrinescu, H. Drinia, M. Bonno, N. Arnaud, P. Monié, F. Quillévéré and A. Ben Moussa (2014), Late Miocene to present-day exhumation and uplift of the Internal Zone of the Rif Chain: Insights from low temperature thermochronometry and basin analysis, *Journal of Geodynamics*, 77, 39-55, doi:10.1016/j.jog.2014.01.006
- Rosenbaum, G.and Lister, G.S., (2004), Neogene and Quaternary rollback evolution of the Tyrrhenian Sea, the Apennines, and the Sicilian Maghrebides.*Tectonics* 23, TC1013, doi:10.1029/2003TC001518.
- Rosenbaum, G., GS. Lister and C. Duboz (2002), Reconstruction of the tectonic evolution of the

## References

- western Mediterranean since the Oligocene. In: Rosenbaum, G. and Lister, G. S. 2002. Reconstruction of the evolution of the Alpine-Himalayan Orogen. *Journal of the Virtual Explorer*, 8, 107 - 130.
- Royden, L.H. (1993), Evolution of retreating subduction boundaries formed during continental collision, *Tectonics*, 12, 629-638, doi:10.1029/92TC02641
- Ruiz-Constán, A., A.Pedrera, J.Galindo-Zaldívar, J.Pous, J.Arzate, F.J.Roldán-García, C.Marin-Lechado, and F.Anahnah (2012), Constraints on the frontal crustal structure of a continental collision from an integrated geophysical research: The central-western Betic Cordillera (SW Spain), *Geochem.,Geophys., Geosyst.*, 13, Q08012, doi:10.1029/2012GC004153.
- Sanz de Galdeano, C. and JA. Vera (1991), Una propuesta de clasificación de las cuencas neógenas béticas, *Acta Geologica Hispanica*, 26 (3-4), 205-227
- Salimbeni, S., S. Pondrelli, L. Margheriti, J. Park and V. Levin (2008), SKS splitting measurements beneath Northern Apennines region: A case of oblique trench-retreat, *Tectonophysics* 462 68–82. doi:10.1016/j.tecto.2007.11.075
- Sato, H., IS. Sacks and T. Murase (1989), The use of laboratory velocity data for estimating temperature and partial melt fraction in the low-velocity zone: comparison with heat flow and electrical conductivity studies, *J. Geophys. Res.*, 94(B5), 5689-5704, doi: 10.1029/JB094iB05p05689
- Schimmel, M., and J. Gallart (2007), Frequency-dependent phase coherence for noise suppression in seismic array data, *J. Geophys. Res.*, 112, B04303, doi:1029/2006JB0046860
- Schmid, Ch., Van Der Lee, S., and D. Giardini (2004), Delay times and shear wave splitting in the Mediterranean region. *Geophys J Int.* 159, 1,275-290. doi.wiley.com/10.1111/j.1365-246X.2004.02381.x.
- Schmid, C., S. van der Lee, J. C. VanDecar, E. R. Engdahl, and D. Giardini (2008), Three-dimensional S velocity of the mantle in the Africa-Eurasia plate boundary region from phase arrival times and regional waveforms, *J. Geophys. Res.*, 113, B03306, doi:10.1029/2005JB004193.
- Seber, D., M. Barazangi, B. A. Ibenbrahim, and A. Demnati (1996), Geophysical evidence for lithospheric delamination beneath the Alboran Sea and Rif-Betic Mountains, *Nature*, 379, 785-790, doi:10.1038/379785a0
- Serrano, I., TM. Hearn, J. Morales and F. Torcal (2005), Seismic anisotropy and velocity structure beneath the southern half of the Iberian Peninsula, *Physics of Earth and Planetary Interiors*. 150, 317-330
- Shear, PM., (2009), Introduction to Seismology (2n edition), Cambridge University Press, Cambridge.
- Song, L-P., M. Koch, K. Koch and J. Schlittenhardt (2004), 2-D anisotropic Pn-velocity tomography underneath Germany using regional traveltimes, *Geophys. J. Int.*, 157, 645–663

## References

- doi: 10.1111/j.1365-246X.2004.02171.x
- Soto, J.I., F. Fernández-Ibáñez, M. Fernández, and A. García-Casco (2008), Thermal structure of the crust in the Gibraltar Arc: Influence on active tectonics in the western Mediterranean, *Geochem., Geophys., Geosystems*, 9(10), 1525-2027, doi:10.1029/2008GC002061
- Stein, S., and M. Wysession (2003), An introduction to seismology, earthquakes, and earth structure, Blackwell Publishing Ltd., London
- Talwani, M. and JR. Heirtzler (1964), Computation of magnetic anomalies caused by two dimensional bodies of arbitrary shape. In: Parks, G. A. (Ed.), Computers in the mineral industries, Part 1. Stanford University Publications, Geological Sciences, 9: 464-480.
- Talwani, M., JL. Worzel and M. Landisman (1959), Rapid gravity computations for two dimensional bodies with application to the Mendocino submarine fracture zone, *Journal of Geophysical Research*, 64: 49-59.
- Tarbuck, EJ., FK, Lutgens and DG. Tasa (2013) Earth: An Introduction to Physical Geology (11<sup>th</sup> edition), Prentice Hall Inc., Upper Saddle River, New Jersey, 2013
- Teixell, A. (1998), Crustal structure and orogenic material budget in west central Pyrenees, *Tectonics* 17, 395–406.
- Tesauro, M., MK. Kaban, and PL. Cloetingh (2008). EuCRUST-07: A new reference model for the European crust, *Geophys. Res. Lett.*, 35, L05313, doi:10.1029/2007GL032244.
- Tesón, E. (2009), Estructura y cronología de la deformación en el borde Sur del Alto Atlas de Marruecos a partir del registro tectono-sedimentario de la cuenca de antepaís de Ouarzazate, Ph.D. Thesis, UniversitatAutònoma de Barcelona, Spain
- Thurner, S., I. Palomeras, A. Levander, R. Carbonell and L. Cin-ty (2014), Evidence for Ongoing Lithospheric Removal in the Western Mediterranean: Ps Receiver Function Results from the PICASSO Project, *Geochem., Geophys., Geosystems*, doi:10.1002/201GC005124
- Torne, M., M. Fernández, M. C. Comas, and J. I. Soto (2000), Lithospheric structure beneath the Alboran Basin: Results from 3D gravity modeling and tectonic relevance, *J. Geophys. Res.*, 105(B2), 3209–3228, doi:10.1029/1999JB900281.
- Udías, A and E. Buforn (1992), Sismicidad y sismotectónica de las Béticas, *Física de la Tierra*, 4, 109-123
- Van Hinsbergen, D., R. Vissers and W. Spakman (2014), Origin and consequences of western Mediterranean subduction, rollback, and slab segmentation, *Tectonics*, 33, 393-419, doi:10.1002/tect.20125
- Vergés, J., H. Millán, E. Roca, JA. Muñoz, M., Marzo, J. Cirés, T. Den Bezemer, R. Zoetemeijer and S. Cloetingh (1995), Eastern Pyrenees and related foreland basins: Pre-, syn- and post-collisional crustalscale cross-sections, *Mar. Pet. Geol.* 12, 893–915.

## References

- Vergés, J. and F. Sàbat (1999), Constraints on the western Mediterranean kinematics evolution along a 1,000-km transect from Iberia to Africa. Geological Society Special Publication, in The Mediterranean basins: Tertiary extension within the Alpine orogen by Durand, B., L. Jolivet, F. Horvath and M. Séranne, 156, 63-80
- Vergés, J., and M. Fernàndez (2012), Tethys-Atlantic interaction along the Iberia-Africa plate boundary: The Betic-Rif orogenic system, *Tectonophysics*, 579, 144-172, doi:10.1016/j.tecto.2012.08.032
- Vernant, P., A. Fadil, T. Mourabit, D. Ouazar, A. Koulali, J.M. Davila, J. Garate, S. McClusky, and R. Reilinger (2010), Geodetic constraints on active tectonics of the Western Mediterranean: Implications for the kinematics and dynamics of the Nubia-Eurasia plate boundary zone, *J. Geodynamics*, 49, 123-129, doi:10.1016/j.jog.2009.10.007
- Watts, A. B., J. P. Platt, and P. Buhl (1993), Tectonic evolution of the Alboran Sea basin, *Basin Res.*, 5, 153 – 177.
- Wessel, P., and W. H. F. Smith, 1998. New, improved version of the generic mapping tool released, *Eos Trans. Am. Geophys. Union* 79, 579
- Wigger, P., G. Asch, P. Giese, W. D. Heinsohn, S. O. E. Alami, and F. Ramdami (1992), Crustal structure along a traverse across the Middle and High Atlas mountains derived from seismic refraction studies, *Geol. Rundsch.*, 81(1), 237–248, doi:10.1007/BF01764552.
- Wildi, W. (1983), La chaînetello-rifaine (Algérie, Maroc, Tunisie): Structure, stratigraphie et évolution du Trias au Miocène, *Rev. Dyn. Geogr. Phys.*, 24, 201-297
- Won, IJ., and M. Bevis (1987), Computing the gravitational and magnetic anomalies due to a polygon: Algorithms and Fortran subroutines, *Geophysics*, 52: 232-238.
- Working Group For Deep Seismic Sounding In Alboran 1974 (1978), Crustal seismic profiles in the Alboran sea-preliminary results. *Pageoph*, 116, 166–180.
- Wortel, W., and W. Spakman (2004), A tomographic view on western Mediterranean geodynamics, in The TRANSMED Atlas — The Mediterranean region from crust to mantle. edited by Ziegler, P., 31-52, Springer, Berlin
- Wüstefeld, A., GHR. Bokelmann, G. Barruol and J-P. Montagner (2009), Identifying global seismic anisotropy patterns by correlating shear-wave splitting and surface waves data, *Phys. Earth Planet. Int.*, 176 (3-4), 198-212, doi:10.1016/j.pepi.2009.05.006 (database available online at <http://www.gm.univ-montp2.fr/splitting/DB/>)
- Zandt, G., and CJ. Ammon (1995), Continental crust composition constrained by measurements of crustal Poisson's ratio, *Nature* 374, 152-154
- Zeck, H.P. (1996), Betic-Rif orogeny: Subduction of Mesozoic Tethys lithosphere under eastward drifting Iberia, slab detachment shortly before 22 Ma and subsequent uplift and extensional tectonics, *Tectonophysics*, 254, 1-16, doi:10.1016/0040-1951(95)00206-5
- Zelt, C.A., and R.B. Smith (1992), Seismic traveltimes inversion for 2-D crustal velocity

## References

- structure, *Geophys. J. Int.*, 108, 16-34, doi:10.1111/j.1365-246x.1992.tb00836.x
- Zeyen, H., P. Ayarza, M. Fernàndez, and A. Rimi (2005), Lithospheric structure under the western African-European plate boundary: A transect across the Atlas Mountains and the Gulf of Cadiz, *Tectonics*, 24, TC2001, doi:10.1029/2004TC001639
- Zhu, H., E. Bozdag, D. Peter and J. Tromp (2012), Structure of the European upper mantle revealed by adjoint tomography, *Nature Geoscience*, 5, 493-498. doi:10.1038/NGEO1501
- Zhu, L., and H. Kanamori (2000), Moho depth variation in southern California from teleseismic receiver functions, *J. Geophys. Res.*, 105(B2), 2969-2980, doi:10.1029/1999JB900322

## Websites:

### Others

NASSA

[visibleearth.nasa.gov/](http://visibleearth.nasa.gov/)

(last view 27<sup>th</sup> November 2014)

### Methodology

Generic Mapping Tools from Wessel and Smith

<http://gmt.soest.hawaii.edu/>

(last view on 27<sup>th</sup> November 2014)

RAYINVR & FAST software packages

<http://terra.rice.edu/department/faculty/zelt/>

(last view on 27<sup>th</sup> November 2014)

Ammon software package

<http://eqseis.geosc.psu.edu/~cammon/HTML/RftnDocs/rftn01.html>

(last view on 27<sup>th</sup> November 2014)

### Seismological data

International Seismological Center

<http://www.isc.ac.uk/>

(last view on 27<sup>th</sup> November 2014)

PICASSO network

<http://ds.iris.edu/gmap/XB?timewindow=2009-2013>

(last view on 27<sup>th</sup> November 2014)

Topo-Iberia network

<http://iberarray.ictja.csic.es/index.php>

(last view on 27<sup>th</sup> November 2014)

Shear-wave splitting data base

<http://www.gm.univ-montp2.fr/splitting/DB/>

(last view on 27<sup>th</sup> November 2014)

### Gravity data

International Gravimetric Bureau (BGI)

<http://bgi.omp.obs-mip.fr/data-products/Grids-and-models/wgm2012>

(last view on 27<sup>th</sup> November 2014)

